Posttranslational modification of the spliceosome paralogue SNRPN links metabolic signaling to splicing regulation

Dissertation
Zur Erlangung des Grades
Doktor der Naturwissenschaften

Am Fachbereich Biologie
Der Johannes Gutenberg-Universität Mainz

Feyza Polat
geboren am 07.07.1994 in Ereğli

Mainz, 2025

Dekan: Prof. Dr.

1. Berichterstatterin: Dr.

2. Berichterstatterin: Prof. Dr.

Tag der mündlichen Prüfung: 27.06.2025

Summary

Gene duplication events give rise to paralogues that can evolve specialized functions over time. SNRPB and SNRPN are two such splicing paralogues, sharing over 90% sequence identity yet exhibiting distinct expression patterns, regulatory features, and disease associations. While SNRPB is ubiquitously expressed and essential in most tissues, SNRPN is expressed primarily in the brain and heart and is subject to genomic imprinting. The aim of this work was to investigate how these paralogues differ at the protein level, particularly focusing on their unstructured regions and their responses to cellular context.

To dissect intrinsic differences between the two proteins, we used an inducible expression system in HEK cells to express 2xHA-mNEON-tagged SNRPB and SNRPN individually in the absence of endogenous SNRPB. Transcriptomic analysis revealed that SNRPN and SNRPB stabilize largely non-overlapping sets of transcripts. SNRPN preferentially stabilized genes that are involved in metabolic pathways and mitochondrial function, and SNRPN-expressing cells exhibited higher proliferation rates. In contrast, SNRPB regulated transcripts involved in cell signaling and adhesion. Despite their roles in the spliceosome, these paralogues did not significantly affect alternative splicing; instead, they appeared to modulate global splicing efficiency, particularly of long and complex transcripts.

A striking difference emerged in the posttranslational regulation of SNRPN. Upon translation inhibition with cycloheximide (CHX), SNRPN – but not SNRPB – underwent a loss of detection by the SmB/B'/N (12F5) antibody, a change that correlated with decreased Arginine methylation in its proline-rich C-terminal region. Mass spectrometry revealed several SNRPN-specific methylated Arginine residues, and mutational analysis showed that replacing key Arginine residues with Lysine residues abolished this CHX-sensitive phenotype. Notably, Arginine 228 (R228) was consistently present in all mutation combinations that disrupted the phenotype but was never observed as methylated, suggesting it may instead be citrullinated.

Together, these findings uncover a previously unrecognized regulatory axis in which SNRPN integrates translational and metabolic cues to modulate its posttranslational state and stabilize complex transcripts. This translationally sensitive regulation may explain why SNRPN is enriched in energy-demanding tissues such as the brain. This work establishes a framework for understanding how paralogues with nearly identical sequences can diverge through subtle, context-dependent posttranslational modifications to acquire distinct cellular roles.

Zusammenfassung

Durch Genduplikationen entstehen paraloge Proteine, die im Laufe der Zeit spezialisierte Funktionen entwickeln können. SNRPB und SNRPN sind zwei solcher Spleiß-Paraloge, die zwar eine Sequenzidentität von über 90 % teilen, jedoch unterschiedliche Expressionsmuster, regulatorische Merkmale und Krankheitsassoziationen aufweisen. Während SNRPB ubiquitär exprimiert wird und in den meisten Geweben essenziell ist, wird SNRPN überwiegend im Gehirn und im Herzen exprimiert und unterliegt der genomischen Prägung. Ziel dieser Arbeit war es, Unterschiede der Paraloge auf Proteinebene zu untersuchen, insbesondere in Bezug auf ihre unstrukturierten Regionen und ihren Reaktionen auf den zellulären Kontext.

Um die intrinsischen Unterschiede zwischen den beiden Proteinen zu entschlüsseln, haben wir ein induzierbares Expressionssystem in HEK-Zellen verwendet, um 2xHA-mNEON-markiertes SNRPB und SNRPN einzeln in Abwesenheit von endogenem SNRPB zu exprimieren. Transkriptom-Analysen zeigten, dass SNRPN und SNRPB überwiegend nicht-überschneidende Transkriptgruppen stabilisieren. SNRPN stabilisierte bevorzugt Gene, die an Stoffwechselwegen und mitochondrialen Funktionen beteiligt sind, und SNRPN-exprimierende Zellen wiesen höhere Proliferationsraten auf. SNRPB hingegen regulierte Transkripte, die an der Zellsignalisierung und Adhäsion beteiligt sind. Trotz ihrer Rolle im Spleißosom beeinflussten die Paraloge das alternative Spleißen nicht signifikant; stattdessen schienen sie die globale Spleiß-Effizienz zu modulieren, insbesondere bei langen und komplexen Transkripten.

Ein auffälliger Unterschied zeigte sich in der posttranslationalen Regulierung von SNRPN. Nach Translationshemmung mit Cycloheximid (CHX) wurde SNRPN - nicht jedoch SNRPB - durch den SmB/B'/N (12F5)-Antikörper nicht mehr detektiert. Diese Veränderung korrelierte mit verminderter Arginin-Methylierung in der prolinreichen C-terminalen Region von SNRPN. Massenspektrometrie zeigte mehrere SNRPN-spezifische methylierte Argininreste auf, und eine Mutationsanalyse ergab, dass der Austausch von wichtigen Argininresten durch Lysinreste diesen CHX-empfindlichen Phänotyp aufhob. Arginine 228 (R228) war in allen Mutationskombinationen vorhanden, die den Phänotyp veränderten, wurde jedoch nie als methyliert detektiert, was auf eine mögliche Citrullinierung hinweisen könnte.

Gemeinsam decken diese Ergebnisse eine bisher unerkannte regulatorische Achse auf, in welcher SNRPN translatorische und metabolische Hinweise integriert, um seinen posttranslationalen Zustand zu modulieren und komplexe Transkripte zu stabilisieren. Diese translationssensitive Regulierung könnte erklären, warum SNRPN besonders in Geweben mit hohem Energieverbrauch, wie dem Gehirn, angereichert ist. Diese Arbeit bietet einen Rahmen, um zu verstehen, wie Paraloge mit nahezu identischer Sequenz durch subtile, kontextabhängige posttranslationale Modifikationen divergieren können, um unterschiedliche zelluläre Rollen übernehmen.

Acknowledgements

Contents

List of Figures

List of Tables

Abbreviations

ADMA	asymmetric dimethylarginine
ALS	amyotrophic lateral sclerosis
AML	acute myeloid leukemia
Arg	Arginine
ASO	antisense oligonucleotide
CCMS	Cerebro-Costo-Mandibular syndrome
cDNA	complementary DNA
CHX	cycloheximide
EDM	euclidean distance map
FRAP	fluorescence recovery after photobleaching
GAR	glycine- and arginine-rich
GOI	gene of interest
hiPSCs	human induced pluripotent stem cells
IPs	immunoprecipitations
MDS	myelodysplastic syndromes
MMA	monomethylarginine
NMD	nonsense-mediated decay
non-DE	non-differentially expressed
ORF	open reading frame
padj	adjusted *p*-values
PADs	peptidylarginine deiminases
PGM	proline-, glycine- and methionine-rich
PlaB	pladienolide B
P-rich	proline-rich
PRMT	protein arginine methyltransferase
PTC	premature termination codon
PTM	posttranslational modification
PWS	Prader-Willi syndrome
RBP	RNA-binding protein
RG	arginine-glycine
RNA Pol II	RNA polymerase II
RNA Pol III	RNA polymerase III
RP	retinitis pigmentosa
SAM	S-adenosylmethionine
SDMA	symmetric dimethylarginine

SF1	splicing factor 1
SLE	systemic lupus erythematosus
SMA	spinal muscular atrophy
SMN	survival of motor neuron
snoRNA	small nucleolar RNA
snRNA	small nuclear RNA
snRNP	small nuclear ribonucleoprotein
TSS	transcription splice sites
U2AF	U2 snRNP auxiliary factor
WGD	whole-genome duplication

1. Introduction

1.1. Gene Duplication Events and Their Evolutionary Significance

1.1.1. Historical perspective of gene duplications

Gene duplication is a fundamental evolutionary process, providing new genes with novel functions (Rice and McLysaght 2017; Bergthorsson, Andersson, and Roth 2007). The early theories of Susumu Ohno in his book “Evolution by Gene Duplication” laid the foundation of the mutation during nonfunctionality model, also known as neo-functionalization model. This model suggests that duplicated genes are not subject to the same selective pressures as the original one, and this makes newborn genes free to accumulate mutations and to gain new functions (Bergthorsson, Andersson, and Roth 2007; Koonin 2005).

Neutral duplicated genes are subject to loss by genetic drift and inactivating mutations such as deletions, frameshift or nonsense mutations. Although the neo-functionalization model explains how new functions can emerge, it does not address how neutral duplicated genes are not lost before acquiring new functions (Bergthorsson, Andersson, and Roth 2007). To address this issue, alternative models have been proposed such as the sub-functionalization model, proposed by Aleksand S. Serebrowsky. This model provides an explanation to how duplicated genes could be retained (Kuzmin, Taylor, and Boone 2022). Details of sub-functionalization will be given in another chapter.

1.1.2. Gene dosage alterations

Gene duplication events often lead to changes in gene dosage, which refers to the relative gene copy number within the genome (Basilicata and Keller Valsecchi 2021). Different organisms have different gene numbers such as budding yeast with approximately 6275 genes, mouse with around 30,000 genes, and human with 20,000-25,000 genes (Drobek 2022). However, what is particularly significant is not just the total number of genes, but how changes in gene dosage can affect cellular processes (Drobek 2022; Basilicata and Keller Valsecchi 2021). Increased gene dosage due to duplication can alter the levels of RNA and protein products, impacting biological functions in both beneficial and detrimental ways such as in sex determination and cancer development, respectively (Basilicata and Keller Valsecchi 2021).

Gene dosage alterations can occur at different levels, one of which is single-gene level dosage alterations. (Basilicata and Keller Valsecchi 2021). This category includes gene copy number variations, duplications or deletions of DNA fragments (Auwerx et al. 2024). There are many

examples of specific gene duplications causing developmental abnormalities, diseases, or adaptive advantages. In drosophila, having 3 copies of *Tpl* locus causes lethality (Basilicata and Keller Valsecchi 2021). In human, whereas duplication of *APP* locus on chromosome 21 is associated with autosomal dominant early-onset Alzheimer disease (Rovelet-Lecrux et al. 2006), duplication of *SNCA* locus on chromosome 4 is associated with Parkinson disease (Kara et al. 2014). Single-gene level dosage alterations can also contribute to adaptation in various organisms. In humans, it was found that individuals having a high-starch diet have more salivary amylase protein level as well as higher salivary amylase gene copy number (Perry et al. 2007). Moreover, in rice, duplication of GL7 locus increases grain length (Liu et al. 2020).

Another level of gene dosage alteration occurs at the chromosome-wide level. This category includes whole-genome duplications, aneuploidies, and sex chromosomes. Whole-genome duplication (WGD), the duplication of the entire chromosome set, is both an ancient and current process observed in yeast, plants, and animals (Lambuta et al. 2023; Crow and Wagner 2006). WGD was often considered as a “dead end”, with its long-term persistence being a rare event. However, although it is still considered as a rare event, some retained WGD examples have changed the view from being “dead end” to being “advantageous” (Moriyama and Koshiba-Takeuchi 2018). One of the best-studied examples of WGD is the baker’s yeast *Saccharomyces cerevisiae*, where WGD was shown to result from hybridization between two different ancestral species followed by genome doubling, rather than simple doubling the DNA of a single ancestor about 100 million years ago (Moriyama and Koshiba-Takeuchi 2018; Merico et al. 2007). After going through WGD, yeast has acquired the ability to grow in the absence of oxygen (Merico et al. 2007). Another example of retained WGD is from the salmonids: the Atlantic salmon, which underwent WGD nearly 100 million years ago. This event enhanced its ability to adapt to varying environments by contributing to its ability to produce different phenotypes (Warren et al. 2014).

In contrast to WGD, aneuploidy involves the gain or loss of individual chromosomes or chromosome arms rather than the entire chromosome set. These imbalances can disrupt cellular functions and lead to cell cycle delays, metabolic alterations, genomic instability, or proteotoxicity (Oromendia and Amon 2014). Aneuploidy is associated with various disorders, including squamous carcinoma, Down syndrome, and Klinefelter syndrome caused by the gain of small arm of chromosome 3, an extra copy of chromosome 21, and an additional X chromosome in males, respectively (Taylor et al. 2018; Biancotti et al. 2010). However, aneuploidy can also be beneficial in certain cases, such as in octaploid (8n) sugarcane, where increased chromosome numbers enhance crop yield (Renny-Byfield and Wendel 2014).

Dosage imbalance arises in the heterogametic sex, which carries two distinct sex chromosomes. For example, in fruit flies, mice and humans, females have XX chromosomes while males have XY chromosomes, whereas in chickens, females have ZW chromosomes while males have ZZ (Checchi and Engebrecht 2011). To mitigate gene dosage imbalances, organisms have evolved different mechanisms. Male fruit flies upregulate their X chromosome twofold, whereas female mice inactivate one of their X chromosomes. Additionally, some X-linked genes, known as escapees, remain transcriptionally active despite X-inactivation, contributing to allelic diversity. These findings reveal that sex chromosome dosage compensation plays a crucial role in maintaining physiological balance, and is also implicated in human diseases (Basilicata and Keller Valsecchi 2021).

1.1.3. Gene paralogues formation

Gene duplication events generate gene paralogues that are two copies of a gene in the same species (Koonin 2005). These two gene copies are initially functionally redundant, in other words, they share the same function. In case of an elimination of one of the paralogues, the other one is sufficient to compensate for the lost paralogue. After the duplication, paralogues can go through different fates (Figure 1. 1.), and if the outcome is advantageous for the organism, duplicated genes can be maintained, and if not, it can be eliminated through selection. Whereas some duplicated genes can maintain the initial redundancy (Figure 1. 1. a), most either acquire new functions (Figure 1. 1. b), partition ancestral functions (Figure 1. 1. c), or are lost (Figure 1. 1. d) (Drobek 2022).

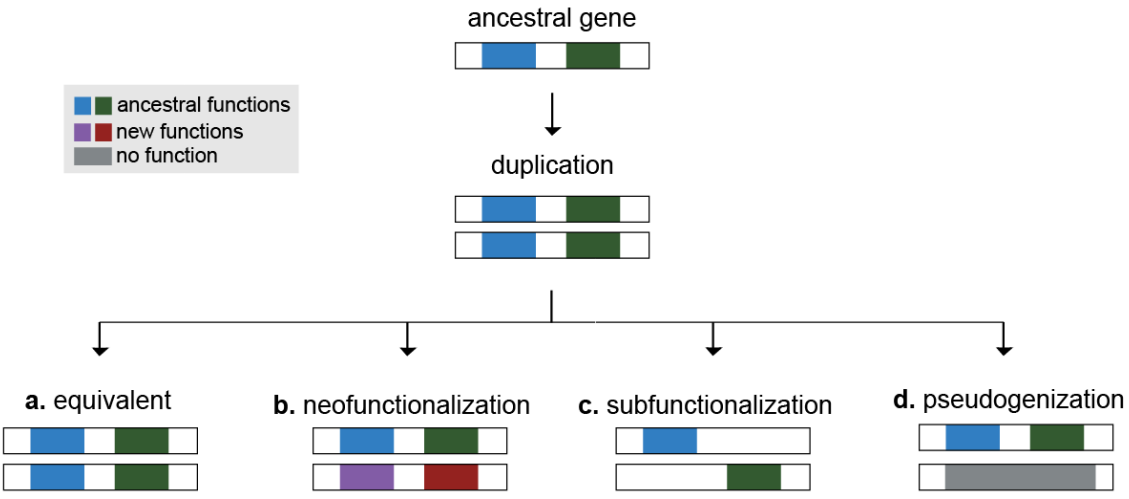

Figure 1. 1. Possible fates of gene paralogues after duplication. (Adapted from Drobek 2022; Kuzmin, Taylor, and Boone 2022)

Functional redundancy between paralogues can be either full or partial. Fully redundant paralogues can completely compensate for the loss of one another, whereas partially redundant paralogues provide only partial compensation (Drobek 2022). For example, gene paralogues XRCC4 and XLF, core factors of nonhomologous end joining, exhibit full functional redundancy. They can function independently, but their combined deficiency impairs DNA repair (Kumar, Alt, and Frock 2016). In contrast, gene paralogues CNOT7 and CNOT8, both catalytic subunits of the CCR4-NOT complex involved in mRNA deadenylation, display partial functional redundancy, as their combined knockdown reduces cell proliferation (Aslam et al. 2009).

Functional divergence among paralogues can occur through neo-functionalization or sub-functionalization, both of which contribute to their retention. In neo-functionalization, one paralogue gains a novel function that was absent in the ancestral gene, while the other paralogue retains the original function. This gain of new function arises due to the mutation accumulation, which can occur in either the coding or regulatory sequence of one gene. An example of neo-functionalization is seen in the histone chaperone genes Asf1a and Asf1b. While both originated from a common ancestor, they have acquired distinct roles. Asf1a is essential for embryonic development, regulating histone H3.3 deposition and Oct4 expression, while Asf1b primarily regulates cell proliferation in early embryos (Drobek 2022).

In sub-functionalization, ancestral functions are partitioned between paralogues genes, with each paralogue retaining only a subset of the ancestral functions. Similar to neo-functionalization, mutations can occur in either the coding or regulatory sequences. However, unlike neo-functionalization, mutations affect both paralogues at different sites. An example of sub-functionalization is seen in the SUMO gene family in rockcress, which diversified into eight paralogues post-duplication. SUMO1 and SUMO2 have been retained through sub-functionalization, with each paralogue specializing in distinct but complementary roles in plant immunity, rosette size and flowering time (Hammoudi et al. 2016).

Finally, in pseudogenization, one of the paralogues is not retained and instead becomes a nonfunctional null allele post-duplication, likely due to a lack of selective advantage. As a result, it loses its function. This fate is more common than the retention of both paralogues (Drobek 2022). An example of pseudogenization is found in toothed whales, where the olfactory receptor gene has gone through pseudogenization, leading to the loss of the olfactory sense (McGowen, Clark, and Gatesy 2008).

While traditional models emphasize the role of paralogues in providing mutational robustness, a systematic study in yeast paralogues exhibited gene duplication can sometimes increase the mutational fragility rather than robustness. By analyzing protein-protein interactions of 56 protein pairs in wild-type yeast cells and in cells lacking a paralogue, the study found that while

some paralogues proteins (22 out of 56) compensated for the loss of the other, an equivalent number (34 out of 56) exhibited the opposite effect, where the absence of one paralogue disrupted interactions rather than maintaining them. The latter group of paralogues pairs often interacted physically, regulated the abundance of each other, and more retained than non-interacting paralogues (Diss et al. 2017). This suggests that gene duplication not only contributes to functional redundancy, but also introduces the mutational fragility into protein-protein interaction network, influencing whether duplicated genes are retained or lost over time.

The principles of gene duplication and paralogue evolution discussed above are exemplified by the specific case of Snrpb and Snrpn. These genes illustrate how duplication events can lead to functional redundancy, regulatory divergence, and evolutionary retention over time. While Snrpb shares redundancy with its isoform Snrpb', Snrpn has evolved unique regulatory features, including genomic imprinting. Together, these genes provide insight into the broader evolutionary dynamics of duplicated genes.

1.1.4. Evolution of Snrpb and Snrpn gene paralogues

Snrpb, a core component of the spliceosome, was first identified in rodents. Later, studies in human HeLa cells revealed that SNRPB appears as a double band on immunoblots, leading to the discovery that humans express an additional isoform, SNRPB', which is absent in rodents (Matter et al. 1982; Todd A. Gray et al. 1999). This isoform diversity in humans arises from alternative splicing of exon 7 in the Snrpb/b' gene, where an alternative 3' splice site generates two protein products with distinct C-terminal sequences (Saltzman, Pan, and Blencowe 2011; Lynch et al. 2014; Turner et al. 2023). Despite these sequence differences, Snrpb and Snrpb' exhibit functional redundancy, as demonstrated by a rescue experiment in which Snrpb knockdown was successfully rescued by transfection with either Snrpb or Snrpb' cDNA (Saltzman, Pan, and Blencowe 2011).

From an evolutionary perspective, Snrpb' is thought to be the ancestral form of the gene. More than 90 million years ago, a gene duplication event involving Snrpb' gave rise to the Snrpn paralogue. Since rodents lack Snrpb', early studies assumed Snrpb was the ancestral gene. However, sequence comparisons by Gray et al. revealed that the putative SNRPB' protein products in hedgehog, opossum, wallaby, and chicken share the same length and high amino acid sequence similarity with human SNRPB' and SNRPN (Table 1. 1), suggesting that Snrpb' predates the gene duplication event that produced Snrpn (Todd A. Gray et al. 1999).

Table 1. 1. Sequence similarity of putative SmB' protein in different species compared to human SNRPB' and SNRPN.

Organism	Similarity to human SNRPB'	Similarity to human SNRPN	Reference
Hedgehog	>99%	93%	Todd A. Gray et al. 1999
Opossum	97%	94%	
Wallaby	96%	93%	
Chicken	96%	92%	

1.1.5. Distinct gene regulations of SNRPB and SNRPN gene paralogues

Despite their shared ancestry from SNRPB', SNRPB and SNRPN exhibit distinct regulatory mechanisms, including differences in alternative splicing and genomic imprinting (Rapkins et al. 2006).

In SNRPB, gene expression is tightly regulated by alternative splicing. In addition to the exon 7 splicing event that generates *SNRPB* and *SNRPB*', another alternative splicing event occurs between exon 2 and exon 3, where an alternative exon is located. This alternative exon, which is highly conserved in mammalian genomes, contains a premature termination codon, leading to nonsense-mediated decay and serving as an autoregulatory mechanism to prevent excessive *SNRPB* expression (Saltzman, Pan, and Blencowe 2011; Lynch et al. 2014).

In contrast, SNRPN follows a different regulatory strategy. The *SNURF-SNRPN* locus has a bicistronic gene organization, meaning that a single promoter drives the expression of both *SNURF* and *SNRPN*. The upstream open reading frame (ORF) encodes *SNURF*, while the downstream ORF encodes *SNRPN* (Tsai et al. 2002; T. A. Gray, Saitoh, and Nicholls 1999). Unlike *SNRPB*, which is expressed from both alleles, *SNRPN* is subject to genomic imprinting. Specifically, the maternal SNRPN allele is highly methylated and silenced, while the paternal allele remains unmethylated and active (Todd A. Gray et al. 1999; Bressler et al. 2001; Tsai et al. 2002).

1.2. RNA Splicing

1.2.1. Introduction to RNA splicing

RNA splicing is a post-transcriptional process, in which noncoding introns of pre-mRNAs are removed, and coding exons are ligated to generate mature mRNAs (van den Hoogenhof, Pinto, and Creemers 2016). This process occurs in eukaryotic organisms, including fungi (e.g. yeast), plants (e.g. rockcress, rice), and animals (e.g. human, mouse, chicken) (Muzafar et al. 2021; Tognacca et al. 2023; Sammeth, Foissac, and Guigó 2008; Hong Zhang et al. 2024). Prokaryotes (e.g. bacteria and archaea) were traditionally thought to lack introns and splicing. However, recent studies have shown that introns exist in prokaryotes, though they are much less common. It is suggested that these introns were inserted through transposon-like mechanisms (Rogers and Bendich 2023).

There are two types of splicing: constitutive splicing and alternative splicing. In the former, one mRNA transcript is generated from a single gene by removing all introns, and ligating all exons sequentially (Figure 1. 2). Unlike constitutive splicing, alternative splicing increases diversity of complex organisms by generating multiple mRNA transcripts from a single gene via different mechanisms. In exon skipping, a prevalent mechanism of alternative splicing, specific exons are removed from the final mRNA. By including only one of two exons, but not both, mutually exclusive exons are incorporated into the mRNA. Alternative splice site selection at 5' and 3' results in longer and shorter exon formation. Other mechanisms include partial or complete intron retention, and the choice of alternative transcription splice sites (TSS) or alternative poly-A sites (Kaminska 2024; Yan Wang et al. 2015).

Although it was thought that only 5% of human genes were subjected to alternative splicing in the 1980s, with the technological improvements, this number has increased to >95% (Yan Wang et al. 2015). Despite the prevalence of intron-containing genes in eukaryotic genomes, a small fraction of protein-coding genes, known as intronless genes, lack introns entirely and do not undergo splicing. Since they lack introns, intronless genes can be transcribed more efficiently and at potentially higher rates compared to genes containing multiple exons (Osemwenkhae and Aguebor-Ogie 2021; Yong Chen et al. 2023).

While RNA splicing is essential for generating mature mRNAs, the process relies on a highly coordinated molecular machinery to ensure precision and accuracy. This machinery is the spliceosome, a large and dynamic RNA-protein complex that identifies splice sites and catalyzes the removal of introns. The complex assembly and function of the spliceosome form the basis for understanding how splicing achieves its specificity.

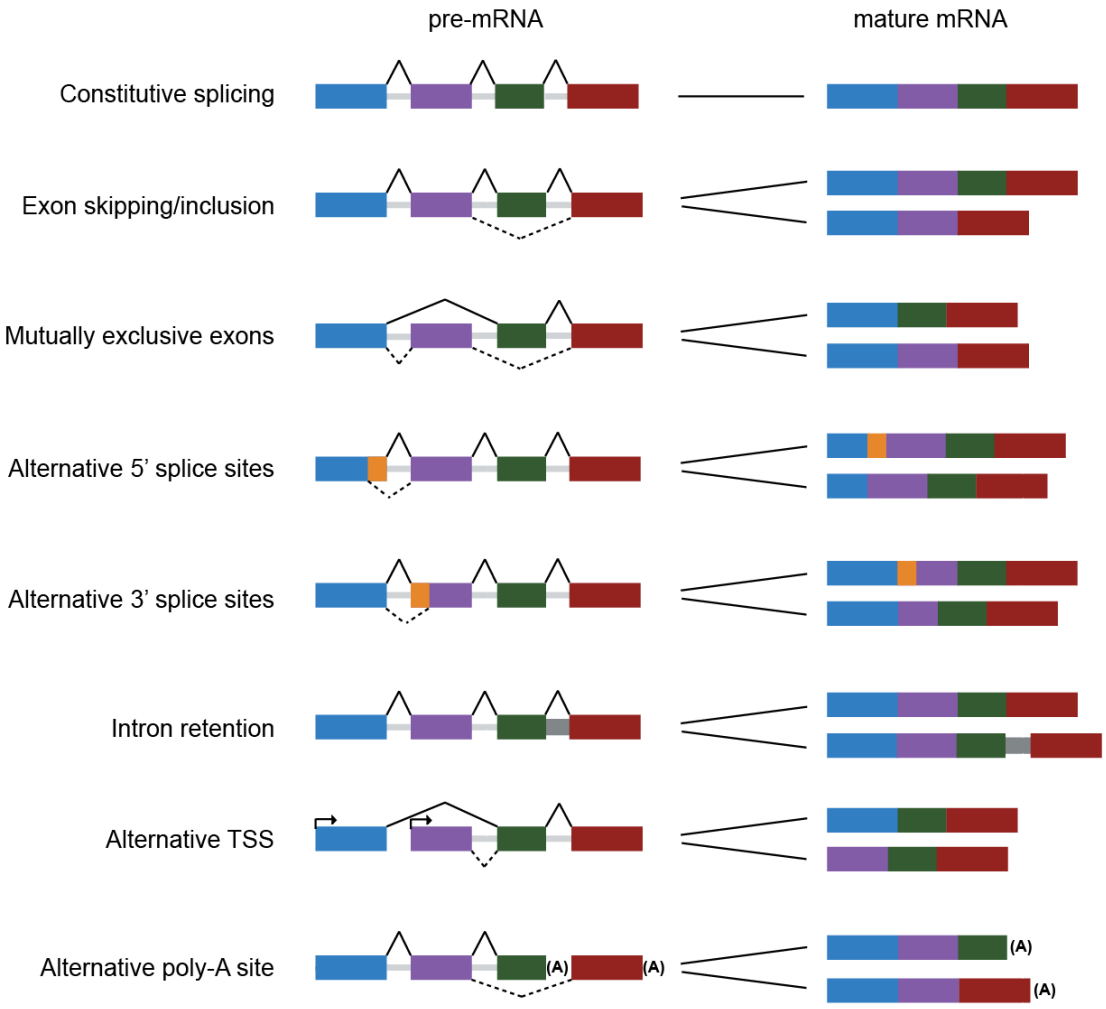

Figure 1. 2. Mechanisms of alternative splicing. Exons are implicated with colored bars, whereas introns are with gray lines. TSS: transcription splice sites, (A): polyadenylation sites (Adapted from Kaminska 2024)

1.2.2. The spliceosome and its assembly

RNA splicing is executed by the spliceosome, a highly dynamic large RNA-protein complex. This complex contains small nuclear ribonucleoproteins (snRNPs). Each snRNPs include small nuclear RNAs (snRNAs, U1, U2, U4/U6, or U5), along with a heptameric Sm ring (SNRPB/B/N', SNRPD1, SNRPD2, SNRPD3, SNRPE, SNRPF, and SNRPG), and more than 150 splicing factor proteins. Each snRNPs are named after their respective snRNAs. In other words, when a complex contains U1 snRNA, it is called U1 snRNP, and so on. The spliceosome identifies specific regulatory sites, including 5' and 3' splice sites, branch point, and polypyrimidine tract (Kambach et al. 1999; Mourão et al. 2016; van den Hoogenhof, Pinto, and Creemers 2016; Kaminska 2024; Yan Wang et al. 2015).

The assembly of spliceosome is a multi-step process where different intermediate complexes (complex E, A, B, and C) are formed. First, U1 snRNP recognizes the 5' splice site of an exon. Splicing Factor 1 (SF1) and U2 snRNP auxiliary factor (U2AF) recognize the 3' splice site on the adjacent exon. U2AF consists of two subunits: 65-kDa subunit U2AF65, and 35-kDa subunit U2AF35. According to the current models, U2AF65 binds to the polypyrimidine tract, whereas U2AF35 detects the AG dinucleotide at the 3' splice site. At this step, complex is called E-complex. Upon displacement of SF1 by U2 snRNP, A-complex, i.e. prespliceosome, is formed. Next, the recruitment of U4/U6 and U5 tri-snRNPs joins U1 and U2 together, forming the B-complex, precatalytic spliceosome. The removal of U1 and U4 from precatalytic spliceosome allows U6 to basepair with 5' splice site and branch point. In complex C, cleavage at 5' splice site generates 3'-OH group and an intron lariat structure. Then, U5 snRNP positions 5' and 3' splice sites together, enabling the 3'-OH group of the upstream exon to attack the 3' splice site. This brings exon-exon ligation, and intron excision in lasso-shaped intron lariat, and followed by the disassembly of spliceosome (Borao, Ayté, and Hümmer 2021; Kambach et al. 1999; van den Hoogenhof, Pinto, and Creemers 2016; Pineda and Bradley 2018).

Around 10 years after the spliceosome discovery, Tarn and Steitz identified another spliceosome targeting <1% of intron, called minor spliceosome (van den Hoogenhof, Pinto, and Creemers 2016). Minor spliceosome replaces U2 snRNP with U12 snRNP. While being functionally similar to the major spliceosome, minor spliceosome shows some differences. Key differences include different splice site and branch point sequences, cytoplasmic splicing, and slower splicing rate. Additionally, unlike major splicing, minor splicing rarely generates alternative isoforms (van den Hoogenhof, Pinto, and Creemers 2016).

The minor spliceosome is found in various eukaryotic species, including humans, slime mold, and some nematodes (Bai et al. 2021; Larue, Eliáš, and Roy 2020; Dávila López, Rosenblad, and Samuelsson 2008). The evolutionary conservation and limited occurrence of minor spliceosome suggest that it serves a unique function rather than acting as a backup (van den Hoogenhof, Pinto, and Creemers 2016). Despite the low abundance of the minor spliceosome, the genes containing them are involved in many essential cellular processes, including DNA replication, DNA repair, cell cycle regulation, transcription, translation, and splicing. The loss of function mutations in minor spliceosome-associated factors caused developmental defects in zebrafish and congenital disorders in humans. These findings highlight the importance of minor spliceosome (Powell-Rodgers et al. 2024).

The precise assembly and function of the spliceosome depend not only on its complicated molecular interactions but also on the spatial organization of its components within the cell. Spliceosome components are dynamically distributed across different subcellular compartments, ensuring their proper maturation, assembly, and recycling.

1.2.3. Subcellular localization of spliceosome

Spliceosome components exhibit distinct subcellular localization. After being synthesized in the nucleus, snRNAs transcribed by RNA polymerase II (all snRNAs except for U6) are exported to the cytoplasm, whereas U6 transcribed by RNA polymerase III stays in the nucleus (Figure 1. 3) (Lorković, Hilscher, and Barta 2004; Yildirim et al. 2021; Hutten et al. 2014). In the cytoplasm, the Survival Motor Neuron (SMN) complex facilitates the incorporation of snRNAs with Sm proteins, forming Sm core snRNPs (Hutten et al. 2014). After acquiring a trimethylguanosine cap at their 5', snRNPs are transported back to the nucleus (Lorković, Hilscher, and Barta 2004; Yildirim et al. 2021; Ohtani 2018).

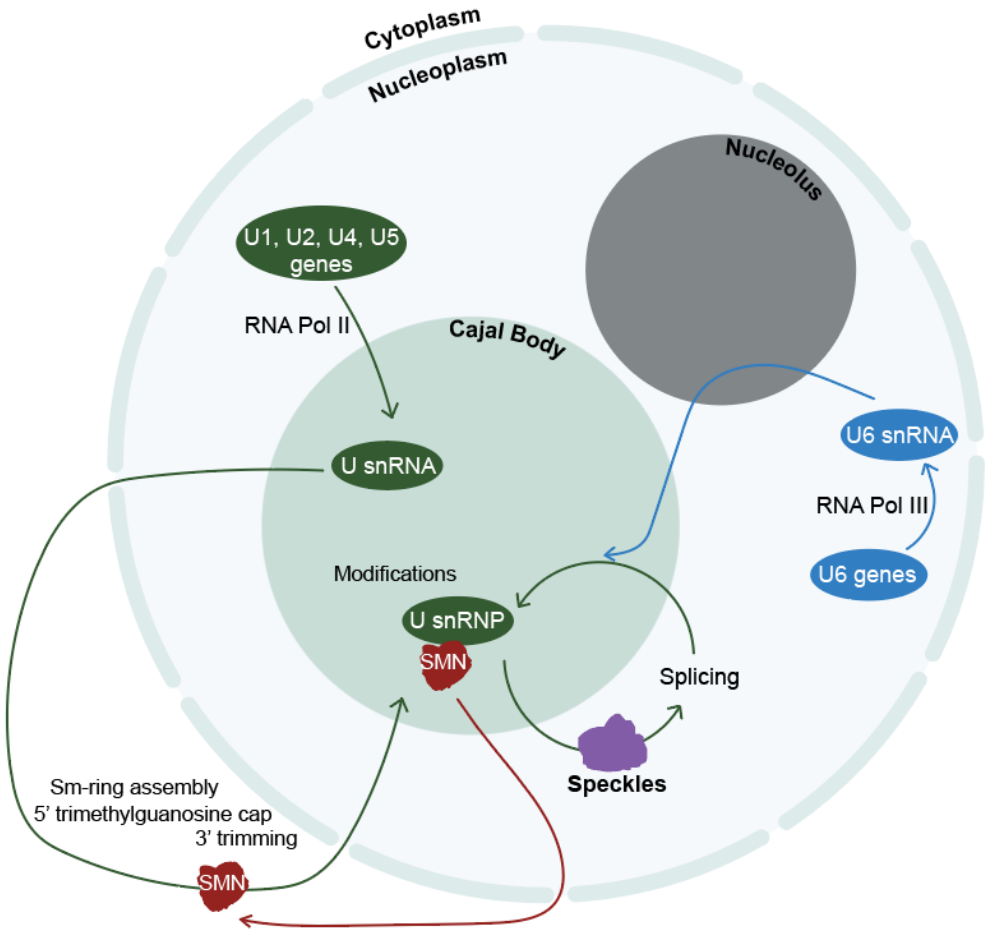

Figure 1. 3. Subcellular localization of spliceosome components. RNA Pol II: RNA polymerase II, RNA Pol III: RNA polymerase III. (Adapted from Machyna, Heyn, and Neugebauer 2013)

Within the nucleus, spliceosomal components localize into specific nuclear compartments, primarily in Cajal bodies and nuclear speckles. Cajal bodies serve as sites for additional snRNP assembly and post-transcriptional modifications, while nuclear speckles function as storage

and assembly sites for splicing factors (Lorković, Hilscher, and Barta 2004; Yildirim et al. 2021; Hutten et al. 2014). Although nucleolus is the well-characterized nuclear compartment, splicing factors do not localize there, except for the transient pass of U6 snRNPs during their maturation (Lorković, Hilscher, and Barta 2004).

After the nuclear import, SMN complex dissociates from Sm core snRNPs, and returns to the cytoplasm, while Sm core snRNPs localize to membraneless spherical Cajal bodies for further processing (Ohtani 2018). Once fully matured, snRNPs exit Cajal bodies and relocate to nuclear speckles, where they participate in active splicing. Following splicing, snRNPs can be recycled for subsequent splicing events, while nuclear speckles retain splicing factors for the next round of splicing (Hutten et al. 2014; Yildirim et al. 2021).

The precise location of spliceosome components within specific subcellular compartments ensures their efficient participation in splicing events. However, the regulation of splicing is not only determined by spatial organization, as many splicing factors exhibit tissue-specific expression patterns that contribute to the unique splicing outcomes observed in different cell types.

1.2.4. Tissue-specific expression of splicing factors

Splicing factors are broadly classified into basal and regulatory factors based on their role in splicing. Basal factors, including core spliceosomal proteins and snRNAs, directly catalyze splicing and are ubiquitously expressed across all cell types. In contrast, regulatory factors modulate splicing by interacting with enhancer or silencer sequences (Dvinge et al. 2019). Enhancers contain binding sites for activators that promote transcription, functioning independently of their position or orientation relative to the gene. Conversely, silencers recruit repressors that inhibit transcription, either by modifying chromatin structure or by blocking activator binding. Like enhancers, silencers operate in a modular and orientation-independent manner, ensuring precise gene regulation across different cellular contexts (Segert, Gisselbrecht, and Bulyk 2021).

While traditionally considered distinct, some studies indicate that some basal splicing factors also exhibit regulatory roles and show tissue-specific expression patterns. Similarly, many regulatory splicing factors exhibit tissue-specific expression, supporting the formation and preservation of the unique splicing process in different cell types (Dvinge et al. 2019).

Comparative studies analyzing splicing factor variations across brain, heart, kidney, liver, and testis in human, mouse, and chimpanzee tissues have shown that several snRNP components, including Lsm2, Lsm4, and Snrpa, are upregulated in the testis, while the core spliceosomal protein SNRPN is highly expressed in the brain. Additionally, SF3A2, a subunit of the splicing

factor 3a complex, and the SR protein kinases SRPK1 and SRPK2 display increased expression in the testis, suggesting a specialized role (Grosso et al. 2008).

While tissue-specific expression of splicing factors contributes to the unique splicing outcomes in different cell types, their activity is also controlled by additional regulatory mechanisms. These include interactions between splicing factors, autoregulatory feedback loops, and the modulation of alternative splicing through microexons. Together, these processes ensure precise regulation of the splicing machinery and its adaptability across diverse cellular contexts.

1.2.5. Regulation of splicing factors

Beyond differential expression, splicing regulation is also influenced by the modulation of ubiquitously expressed splicing factors. Many of these factors maintain the balance of the splicing machinery through cross-regulation or auto-regulatory mechanisms. Some splicing factors interact with others to modulate alternative splicing patterns, while others regulate their own expression to ensure stable protein levels (Pedrotti et al. 2012).

Cross regulation between splicing factors is exemplified by the Fox gene family, particularly Fox-3, which is expressed exclusively in the brain. Fox-3 interacts with PSF, a ubiquitously expressed splicing factor, to activate neural cell-specific alternative splicing of N30 exon. Although Fox-1 and Fox-2 are also expressed in the brain, PSF binds to Fox-3 more efficiently for reasons that remain unclear (Kim et al. 2011; Pedrotti et al. 2012). These interactions illustrate how tissue-specific splicing factors collaborate with general regulators to generate splicing diversity across different cell types.

In addition to cross-regulatory interactions, some splicing factors regulate their own expression though auto-regulatory mechanisms. One example is SNRPB, which undergoes alternative splicing to include a microexon containing a premature termination codon (PTC). The inclusion of this microexon is dependent on *SNRPB* levels. Low *SNRPB* expression reduces microexon inclusion, while higher levels promote its incorporation. This autoregulatory mechanism helps maintain the appropriate balance of *SNRPB* within the cell (Lynch et al. 2014).

Microexons, which are exons ranging from 3 to 30 nucleotides, play a crucial role in splicing regulation, particularly in neurons (Parada et al. 2021; Curry-Hyde et al. 2018). Unlike conventional exons, microexons exhibit high conservation, with over 13,000 conserved microexons in the human genome (J.-S. Lee, Lamarche-Vane, and Richard 2022). The majority are multiples of three nucleotides, preserving the open reading frame and generating alternative protein isoforms that influence protein binding properties and posttranslational

modifications. In contrast, microexons that are not in frame introduces PTCs, leading to degradation by the nonsense-mediated mRNA decay (NMD) pathway, preventing the production of potentially harmful truncated proteins (Ustianenko, Weyn-Vanhentenryck, and Zhang 2017; Curry-Hyde et al. 2018; Inglis et al. 2023).

These examples highlight how splicing regulation integrates cross-regulation, autoregulation, and microexon control to ensure precise gene expression across different tissues. Through these mechanisms, cells achieve the diversity and adaptability necessary for proper function. Among the core components of the spliceosome, SNRPB and SNRPN play critical roles in snRNP assembly and splicing fidelity, serving as key examples of how splicing factors contribute to both general and tissue-specific splicing processes.

1.2.6. SNRPB subunit of the spliceosome complex

SNRPB is one of the core components of the spliceosome complex, forming a heptameric Sm ring with six other Sm proteins. This ring-structure binds to snRNAs and protects them from degradation and facilitates RNA processing (Kambach et al. 1999; Saltzman, Pan, and Blencowe 2011; Hyjek-Składanowska et al. 2020; van Beers and Schreurs 2022).

SNRPB is a 231 amino acid protein with a molecular weight of 24 kDa (Todd A. Gray et al. 1999). It consists of a structured globular Sm domain at the N-terminus and an intrinsically disordered C-terminal region (Figure 1. 4). Intrinsically disordered region contains two distinct motifs. The arginine-glycine (RG) motif, spanning residues 90-167, includes arginine residues that can be symmetrically dimethylated. Downstream of the RG motif, from residues 167-231 in SNRPB, accommodates the proline-rich motif (Mourão et al. 2016).

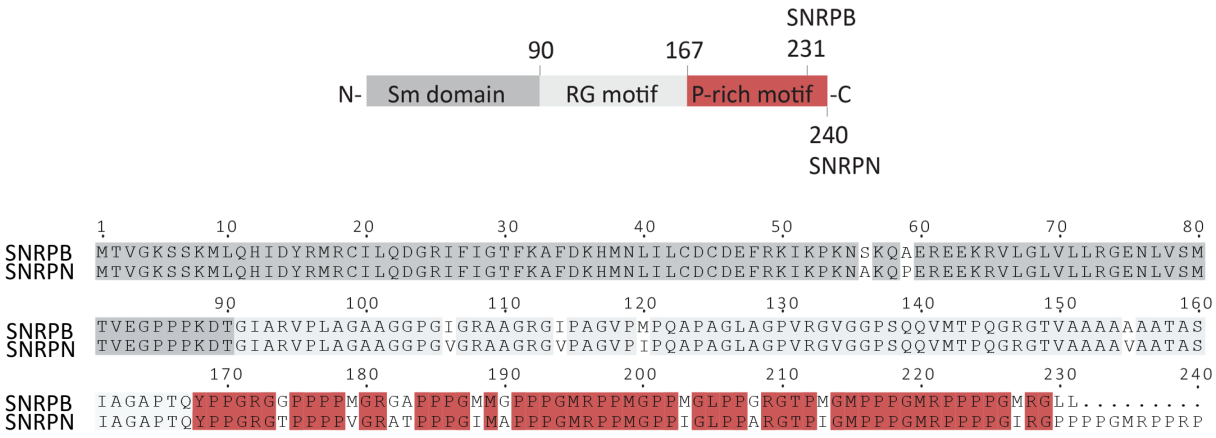

Figure 1. 4. Domain architecture and sequence alignment of SNRPB and SNRPN. The upper panel illustrates the domain organization of SNRPB and SNRPN, whereas the lower panel shows the sequence alignment. RG motif: arginine-glycine motif, P-rich motif: proline-rich motif (Adapted from Todd A. Gray et al. 1999; Mourão et al. 2016)

SNRPB interacts with multiple co-factors through its RG and proline-rich motives. SNRPB forms interactions with Survival Motor Neuron (SMN) and Protein arginine N-methyltransferase 5 (PRMT5) via its RG domain (Yong et al. 2004; DeAngelo et al. 2024). The SMN complex, essential for snRNP biogenesis, recognizes the methylated RG motif and facilitates the transfer of Sm proteins onto snRNAs (Yong et al. 2004). PRMT5 catalyzes the symmetrical methylation of arginine residues within this motif regulating protein-protein interactions critical for snRNP assembly and localization. These interactions ensure proper spliceosome function and contribute to the stability of snRNP complexes within the nucleus (DeAngelo et al. 2024).

SNRPB is proposed to maintain protein-protein interactions through its proline-rich motif. This motif contains proline-rich sequences similar to those found in the CD2 receptor, which associates with SH3 domain. Since SH3 domains mediate protein-protein interactions via proline repeats, the proline-rich motif of SNRPB is also suggested to facilitate interactions crucial for the assembly of snRNP core proteins (Filali et al. 1999). In addition to SH3 domain-containing proteins, SNRPB also interacts with the splicing factor RBM5 through its proline-rich motif. RBM5 contains an OCRE domain that directly binds the proline-rich domain of SNRPB and modulates alternative splicing (Mourão et al. 2016).

1.2.7. SNRPN subunit of the spliceosome complex

Like SNRPB, SNRPN is one of the core components of the spliceosome complex. In brain and heart tissues, it assembles into the heptameric ring together with six other Sm proteins by replacing its paralogue, the SNRPB subunit of the Sm ring (Thompson et al. 2018).

SNRPN consists of 240 amino acids and has a molecular weight of 29 kDa, reflecting its similarity to the ancestral form SNRPB', which also contains 240 amino acids (Sharpe, Williams, and Latchman 1990; Todd A. Gray et al. 1999). It shares the same domain architecture as SNRPB, with an N-terminal Sm domain, a C-terminal intrinsically disordered arginine-glycine (RG) motif, and a proline-rich motif (Figure 1. 4) (Mourão et al. 2016).

Despite their high sequence similarity (>90%), SNRPB and SNRPN exhibit differences at their C-termini (Grimaldi et al. 1993). Sequence alignment highlights these differences, particularly in the P-rich motif, where SNRPN contains an additional nine amino acids (Figure 1. 4).

Beyond its association with the Sm ring, the specific functions of SNRPN remain poorly understood. However, recent studies indicate that SNRPN interacts with a distinct set of proteins. After filtering out nonspecific interactors, mass spectrometry analysis of fluorescently tagged SNRPB and SNRPN revealed several interaction partners unique to SNRPN, suggesting functional divergence. For example, nuclear receptor co-activator 6 interacting protein and 7SK snRNA methylphosphate capping enzyme, both involved in snRNA capping,

were exclusive to the SNRPN interactome. Moreover, RNA-binding protein 40, a component of the minor spliceosome, was detected only in the SNRPN interactome. The presence of these unique interaction partners suggests that SNRPN may have specialized roles beyond its function in snRNP assembly (Thompson et al. 2018).

Despite their structural similarities and shared roles in snRNP assembly, SNRPB and SNRPN exhibit distinct functional characteristics, as evidenced by their unique interaction partners and potential specialized roles. These differences extend beyond their molecular properties to their expression patterns, which vary significantly across tissues and developmental stages.

1.2.8. Distinct expression patterns of SNRPB and SNRPN

SNRPB and its splice isoform SNRPB' are part of the heptameric Sm ring, and ubiquitously expressed across various tissues. On the contrary, their gene paralogue SNRPN exhibits a tissue-specific expression pattern, replacing the SNRPB/B' subunit of Sm ring in tissues where it is highly expressed, particularly in the brain and heart, with a strong presence in central neurons (Ozçelik et al. 1992; Huntriss, Latchman, and Williams 1993; Todd A. Gray et al. 1999; Saltzman, Pan, and Blencowe 2011; Thompson et al. 2018; Turner et al. 2023). Microarray data from Saltzman et al. demonstrated that SNRPB/B' is highly expressed in cell lines and hematopoietic system (described in the figure as "blood, immune"), whereas SNRPN is most abundant in the central nervous system (Figure 1. 5) (Saltzman, Pan, and Blencowe 2011).

Beyond its tissue specificity, SNRPN expression is also regulated developmentally. It is not only restricted to the central nervous system, but also detected in undifferentiated embryonal carcinoma cell lines and undifferentiated embryonic stem cells, suggesting a potential role of SNRPN in early embryonic differentiation (Sharpe, Williams, and Latchman 1990; Huntriss, Latchman, and Williams 1993; Turner et al. 2023). An immunoblot analysis of rat brain lysates from different developmental stages showed a progressive increase in SNRPN level during brain development, concomitant with a decrease in SNRPB levels, eventually replacing SNRPB in adult brain (Figure 1. 6) (Grimaldi et al. 1993).

There is an important factor in interpreting SNRPN expression at the RNA level due to the bicistronic nature of the *SNURF-SNRPN* locus. A single promoter drives the expression of both *SNURF* (upstream ORF) and *SNRPN* (downstream ORF) (Tsai et al. 2002), meaning that detecting *SNURF-SNRPN* RNA does not always indicate SNRPN protein expression. The upstream ORF encoding *SNURF* may influence SNRPN translation, highlighting the need for caution when interpreting RNA-based expression data.

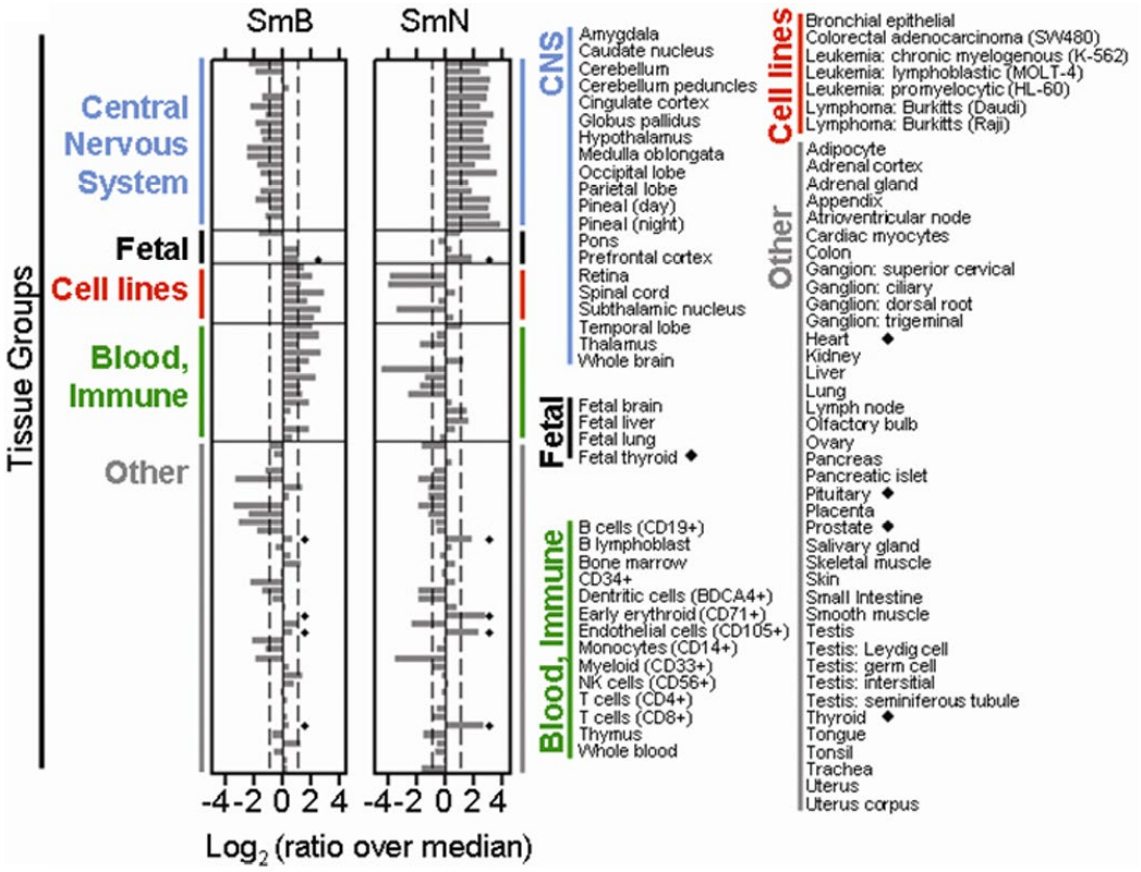

Figure 1. 5. Microarray expression data showing distinct expression patterns of SNRPB (SmB) and SNRPN (SmN) in different tissues and cell lines. Each bar represents 2-5 replicates. Dotted lines indicate expression that is two-fold above or below the median across the 84 samples. (Figure taken from Saltzman, Pan, and Blencowe 2011)

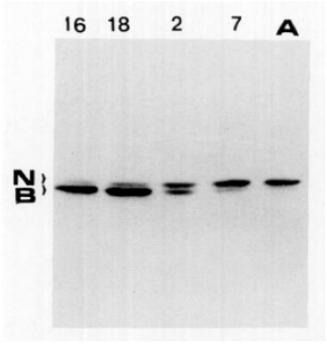

Figure 1. 6. Western blot of lysates obtained from rat brain at different developmental stages. KSm5 antibody recognizing both SNRPB and SNRPN was used. (16/18: embryonic days 16/18, 2/7: 2/7 days postnatal, A: adult) (Figure taken from Grimaldi et al. 1993)

1.3. Cellular Consequences of Aberrant Splicing

1.3.1. Introduction to aberrant splicing

Dysregulation of alternative splicing can lead to aberrant splicing events resulting in the production of abnormal mRNA transcripts and dysfunctional proteins (Kaminska 2024). Aberrant splicing is believed to stem from variations in the cellular composition, concentration, activity, localization, and the mutations of core splicing machinery. It is associated with diseases as both the cause and the consequence (Yan Wang et al. 2015; van den Hoogenhof, Pinto, and Creemers 2016; Will and Lührmann 2011).

Aberrant splicing covers all deviations from normal splicing, including those caused by genetic mutations, environmental factors, or regulatory disruptions. Mis-splicing, on the other hand, refers specifically to defective splicing events that occur due to errors in the splicing process, such as exons skipping, cryptic splice site activation and intron retention (Jung, Lee, and Choi 2021). Exon skipping is the removal of a specific exon from the final mRNA; in other words, the failure of an exon inclusion in the mature mRNA (Kaminska 2024). Cryptic splice site activation includes the usage of non-canonical (cryptic) splice sites, which are used at low levels and normally dormant unless activated by mutation and so on (Kapustin et al. 2011). Intron retention, another form of mis-splicing, occurs when an intron is not spliced out, but transcribed into pre-mRNA (Wong et al. 2016). Intron retention often leads to premature termination codons (PTCs) inclusion. As discussed in 1.2.5., transcripts containing PTCs are considered as harmful and mostly targeted by the nonsense-mediated decay (NMD), which is a conserved quality control mechanism preventing the accumulation of aberrant transcripts by degrading them (Wong et al. 2016).

The dysregulation of splicing mechanisms, whether through mutations, altered expression of splicing factors, or environmental influences, can have profound consequences on cellular function and integrity. In the context of disease, aberrant splicing is increasingly recognized as a central player in both cancerous and non-cancerous disorders, driving pathological processes and presenting opportunities for therapeutic targeting.

1.3.2. Aberrant splicing in cancer

Aberrant RNA splicing plays a crucial role in the initiation, progression and invasion of different cancers (Irimia et al. 2014). Aberrant RNA splicing in cancer might include dysregulation of alternative splicing, mutations in trans-acting splicing factors or mutations in cis-regulatory elements (Scotti and Swanson 2016; Bonner and Lee 2023).

SRSF1 is one of the most extensively studied splicing factors associated with various cancers such as lung, breast, and colon cancer. Its overexpression promotes cell growth and dysregulates the alternative splicing of transcripts involved in apoptosis, proliferation, and DNA damage response, particularly in breast cancer (Bonner and Lee 2023; Anczuków et al. 2012).

Several other splicing factors also show altered expression in cancer, including PRPF6 and PRPF8. The overexpression of PRPF6, which is a U5 snRNP protein, is associated with colorectal carcinoma, leading to the production of an oncogenic form of stress-activated ZAK through alternative splicing. Conversely, reduced expression of PRPF8 is associated with myelodysplastic syndromes and promotes cell proliferation (Scotti and Swanson 2016).

Beyond expression changes of splicing factors, somatic mutations in key spliceosome-associated components have been identified in various cancers. For example, U2AF1 mutations disrupt hematopoiesis and 3' splice site recognition, leading to transcript dysregulation (Scotti and Swanson 2016).

Aberrant splicing is also implicated in solid tumors such as glioblastoma. In a transcriptomic analysis to identify the glioblastoma-associated RNA binding proteins, SNRPB, a subunit of heptameric Sm ring of core spliceosome complex, has emerged as a key regulator of cell viability, cell proliferation, and apoptosis. Knockdown of SNRPB, in glioblastoma cell lines led to decreased cell viability, increased apoptosis, and reduced proliferation. The same study also showed that SNRPB depletion disrupted gene expression and alternative splicing regulation of key genes involved in DNA repair (e.g., BRAC1, RAD50, CHEK1) and glioblastoma development (e.g., MAPK, RAS, p53) (Correa et al. 2016).

Splice site recognition errors also contribute to cancer progression. In chronic lymohocytic leukemia and breast cancer, point mutations in SF3b155, one of the subunits of SF3b, result in cryptic 3' splice site selection and aberrant splicing (DeBoever et al. 2015; Cretu et al. 2016).

The widespread impact of aberrant splicing in cancer highlights its role in driving tumorigenesis and disease progression. However, the disruption of splicing mechanisms is not limited to cancer. It also contributes to the development of various non-cancerous disorders, where similar dysregulation leads to distinct disease phenotypes.

1.3.3. Aberrant splicing in non-cancerous disorders

Splicing factor mutations are associated with a variety of human diseases, often affecting multiple transcripts due to their fundamental roles in the splicing machinery. Unlike mutations in cis-elements that typically affect a single gene, defects in trans-acting splicing factors result in broader dysregulation of gene expression and complex disease etiologies (T. Chen et al.

2019). Although splicing is a fundamental process, spliceosomal diseases exhibit highly specific phenotypes (Turner et al. 2023).

Mutations in the survival of motor neuron 1 (SMN1) gene cause spinal muscular atrophy (SMA), an autosomal recessive neuromuscular disorder characterized by progressive motor neuron degeneration and skeletal muscle atrophy (Crawford et al. 2024; Mallapaty 2025). SMN1 gene encodes SMN1 protein, a key member of the SMN complex that mediates snRNP assembly. Despite its ubiquitous expression, SMN protein deficiency results in selective motor neuron vulnerability, the underlying cause of SMA pathology (Z. Zhang et al. 2008; van den Hoogenhof, Pinto, and Creemers 2016).

Humans have a paralogues gene, SMN2, which can partially compensate for SMN1 loss. However, a C-to-T transition at nucleotide position 840 in SMN2 disrupts an exonic splicing enhancer while creating an exonic splicing silencer. This leads to aberrant splicing, predominantly skipping exon 7, and results in truncated, non-functional SMN protein. Although SMN2 can express some functional SMN protein, its efficiency is much lower than SMN1. The number of SMN2 copies modulates the severity of SMA, with fewer copies associated with more severe phenotypes. However, this correlation is not absolute, as additional genetic variants, epigenetic and posttranslational modifications can influence the ability of SMN2 to produce functional SMN protein (Yeo, Tizzano, and Darras 2024).

The most severely affected cells in SMA are motor neurons in the brainstem and spinal cord. The motor neuron pool in SMA patients consists of a mix of immature, healthy, reversibly damaged, and irreversibly damaged motor neurons. Immature motor neurons are particularly vulnerable to postnatal degeneration, and disease severity inversely correlates with the proportion of surviving healthy motor neurons. In severe SMA cases, a significant reduction in healthy motor neuron numbers is already evident at birth, with neurodegeneration likely initiating in utero. This progressive loss results in a shifting neuronal composition over time, influencing disease progression. However, the precise role of SMN protein in prenatal and postnatal motor neuron development and degeneration remains unknown (Yeo, Tizzano, and Darras 2024).

Mutations in splicing factors can also contribute to craniofacial disorders, which often involve defects in neural crest-derived skeletal elements. The neural crest is a transient, multipotent cell population that plays a crucial role in vertebrate development, giving rise to a wide variety of cell types, including cartilage, bone, connective tissues, and neurons. The development of neural crest cells is tightly regulated by gene expression, and disruptions in this regulation can lead to developmental defects (Achilleos and Trainor 2012). Craniofacial disorders associated with mutations in splicing factors, such as Verheij syndrome (PUF60), mandibulofacial dysostosis (EFTUD2), Nager syndrome (SF3B4), Burn-McKeown syndrome (TXNL4A), and

Taybi-Linder syndrome (RNU4ATAC) are characterized by defects in neural crest cell derivatives, including micrognathia, facial dysmorphisms, and limb abnormalities (Griffin and Saint-Jeannet 2020; Khatri et al. 2023). The precise role of splicing in neural crest development is not fully understood, but it is thought that splicing mutations disrupt key developmental pathways, leading to abnormal cell differentiation and survival in the neural crest lineage. These defects are often observed in the craniofacial region because neural crest cells populate the pharyngeal arches, which gave rise to most structures of the face (Park et al. 2022).

The critical role of splicing dysregulation in non-cancerous disorders, such as SMA and craniofacial disorders, highlights the need for targeted interventions. Advances in understanding these defects have led to the development of splicing-targeted therapies, offering promising strategies to correct aberrant splicing events.

1.3.4. Splicing-targeted therapies

The growing understanding of splicing mechanisms had led to the development of splicing-targeted therapies, including antisense oligonucleotides (ASOs), small molecules, and combination approaches.

Antisense oligonucleotides (ASOs) are short complementary nucleotides correcting aberrant splicing events by binding to specific splice sites or regulatory elements (Douglas and Wood 2011; Szelest and Giannopoulos 2024). Nusinersen, an 18-oligonucletides ASO, binds to an intronic splicing silencer in SMN2, promoting the inclusion of exon 7, and increasing the production of functional SMN protein, thereby partially compensating for the loss of SMN1 (Porensky and Burghes 2013; Marasco et al. 2022; Zhan et al. 2024; Singh et al. 2022).

Small molecules, on the other hand, modulate splicing by targeting spliceosome components or interacting with regulatory proteins. Risdiplam is an FDA-approved oral small molecule splicing modifier that enhances SMN2 exon 7 inclusion, increasing SMN protein levels to treat SMA across a broad patient population, including adults, children and infants from birth (“Roche” n.d.). Recent study has expanded its potential use, demonstrating successful prenatal administration in a fetus diagnosed with SMA. Maternal Risdiplam treatment during late pregnancy resulted in transplacental drug transfer, increased SMN protein levels in the fetus, and lower nerve damage levels compared to other SMA cases (Finkel et al. 2025; Mallapaty 2025).

Finally, combination approaches strengthen the efficacy of ASOs and small molecules. For example, the combination of a low-dose treatment of the Anti-N1 ASO with risdiplam or branaplam small molecules enhances SMN2 exon 7 inclusion by minimizing the disruption of gene expression, unlike higher doses of each treatment (Ottesen and Singh 2024). These

strategies are promising for various splicing-related disorders such as SMA, AML, cancer (Szelest and Giannopoulos 2024).

While splicing-targeted therapies hold significant promise for addressing aberrant splicing in disorders like SMA, mutations in specific spliceosome-associated genes, such as SNRPB and SNRPN, are also linked to rare genetic conditions with distinct pathological mechanisms.

1.3.5. Genetic disorders associated with mutations in SNRPB and SNRPN

Mutations in SNRPB and SNRPN are linked to Cerebro-Costo-Mandibular syndrome (CCMS) and Prader-Willi syndrome (PWS), respectively.

CCMS is a congenital skeletal disorder characterized by micrognathia, glossoptosis, U- or V-shaped cleft palate, rip gaps, scoliosis, respiratory complications, and the lack of external ear canals (Bacrot et al. 2015; Lynch et al. 2014; Knill et al. 2024). This rare developmental disorder is classified as a spliceosomopathy, as it is associated with mutations in SNRPB. However, disease-associated mutations do not occur in the coding region but rather in an alternative exon containing a premature termination codon. These mutations lead to aberrant splicing, resulting in increased inclusion of the alternative exon and subsequent activation of non-sense mediated decay, thereby reducing overall *SNRPB* expression levels (Lynch et al. 2014; Knill et al. 2024).

Although splicing occurs in all tissues, the phenotypic consequences of spliceosomal defects often affect specific organs. In the case of CCMS, skeletal abnormalities arise due to impaired bone and cartilage formation. A recent study has shown that reduced *SNRPB* expression, through either knockdown or mutation, suppresses osteogenesis while promoting chondrogenesis. This is linked to altered splicing of Dlx5, a key regulator of bone development, and TCF7L2, which influences Wnt/β-catenin signaling. Activating this pathway rescues osteogenesis, while Wnt inhibitors enhance chondrogenesis. These findings suggest that SNRPB plays a crucial role in skeletal development, and its disruption contributes to CCMS pathology (Knill et al. 2024).

PWS is a neurodevelopmental disorder characterized by neonatal hypotonia, intellectual disability, growth retardation, short stature, small hands, facial dysmorphism, strong appetite, and obesity (Ozçelik et al. 1992; Glenn et al. 1996; Bressler et al. 2001; Rohm et al. 2025). It results from the absence of expression of paternally inherited genes within the 15q11-q13 region, primarily due to deletions or imprinting defects (Ozçelik et al. 1992; T. A. Gray, Saitoh, and Nicholls 1999; Bressler et al. 2001; Rohm et al. 2025).

SNRPN is a maternally imprinted gene, which is expressed exclusively from the paternal allele (Glenn et al. 1996; T. A. Gray, Saitoh, and Nicholls 1999). While early studies suggested that SNRPN gene loss contributes to PWS, mouse models have shown that its absence alone is not enough to show phenotypic abnormalities (Ozçelik et al. 1992; Bressler et al. 2001). Instead, patient mutation profiles suggest that the small nucleolar RNA (snoRNA) gene cluster SNORD116, which is located downstream of the *SNURF-SNRPN* locus, plays a crucial role in PWS pathology. Notably, patients with microdeletions affecting SNRPN exon 2 and 3, while retaining SNORD116 expression, have been reported to exhibit classic PWS symptoms, suggesting that additional factors may contribute to disease manifestation (Rohm et al. 2025).

Microdeletions in the imprinting center upstream of Snrpn result in aberrant methylation of the paternal allele, ultimately silencing PWS-associated genes and causing the disorder (Bressler et al. 2001). Because the maternal allele remains intact but epigenetically silenced, therapeutic strategies aimed at reactivating the maternal copy of critical genes, such as SNORD116, may offer a potential treatment avenue for PWS (Rohm et al. 2025).

The role of spliceosome-associated proteins in genetic disorders such as CCMS and PWS highlights their importance in maintaining cellular and developmental processes. These proteins are also linked to autoimmune diseases, where defects in immune tolerance result in the production of autoantibodies targeting components like Sm proteins.

1.3.6. Anti-Sm autoantibodies

Systemic lupus erythematosus (SLE) is a complex autoimmune disease characterized by the presence of a wide range of autoantibodies, particularly those targeting nuclear components. Among them, anti-Smith (anti-Sm) antibodies are highly specific for SLE and were first identified in 1966 (Cozzani et al. 2014; van Beers and Schreurs 2022). Despite their specificity, anti-Sm antibodies are detected in only 5-30% of SLE patients, depending on ethnicity and the detection method (van Beers and Schreurs 2022). These antibodies primarily recognize SmB (SNRPB, SNRPB', SNRPN) and SmD (SNRPD1, SNRPD2, SNRPD3) proteins, components of snRNP complex (Huntriss, Latchman, and Williams 1993; Filali et al. 1999; van Beers and Schreurs 2022).

The origin and the precise mechanisms leading to anti-Sm autoantibody production remain unclear. SLE is characterized by the breakdown of B-cell tolerance, resulting in the activation of autoreactive B cells that produce antibodies against self-antigens, including nuclear and cytoplasmic proteins (Cozzani et al. 2014; van Beers and Schreurs 2022). The Sm proteins, particularly SmD1 and SmD3, are considered the most specific antigens for SLE due to their limited cross-reactivity with other autoantigens (van Beers and Schreurs 2022). The targeting

of the immune system toward spliceosomal proteins like Sm remains poorly understood, but one hypothesis suggests that apoptosis and NETosis, neutrophil specific kind of death, contribute to the impairment of the clearance of apoptotic cells, the loss of tolerance, and subsequent autoantibody production (Mahajan, Herrmann, and Muñoz 2016).

Autoantibodies targeting Sm proteins can precipitate snRNP complexes containing U1, U2, U4/U6, and U5 RNAs (Filali et al. 1999). Although anti-Sm antibodies are not the most sensitive biomarkers for SLE, they are included in the classification criteria due to their diagnostic specificity (Cozzani et al. 2014). Immunofluorescence studies have shown that Sm antigens are predominantly nuclear, with some cytoplasmic localization, supporting their accessibility to autoantibodies in autoimmune conditions (Lerner and Steitz 1979). Further research is needed to clarify the mechanisms driving their production and their potential role in disease progression (Cozzani et al. 2014).

1.4. Posttranslational Modifications (PTMs): Arginine Methylation

1.4.1. General introduction into PTMs and their functional significance

Posttranslational modifications (PTMs) are covalent modifications that alter the properties of proteins by introducing functional groups such as acetyl, phosphoryl, glycosyl, and methyl groups or by proteolytic cleavage. These modifications regulate the function of a wide range of proteins, including secretory and membrane proteins, as well as histones (Ramazi and Zahiri 2021; Deribe, Pawson, and Dikic 2010; Fan et al. 2015).

PTMs influence a wide range of protein characteristics, including enzymatic activity, assembly, stability, solubility, protein–protein interactions, receptor activation, molecular trafficking, and subcellular localization. By altering protein conformation, charge, and interactions with DNA, RNA, and other proteins, PTMs ultimately regulate cellular phenotypes and biological functions. These modifications are essential to various biological processes, such as signal transduction, gene expression regulation, DNA repair, cell cycle progression, metabolism, immunity, cell differentiation, and autophagy (Ramazi and Zahiri 2021; Zhong et al. 2023; Yang et al. 2023; Fan et al. 2015).

Specific PTMs contribute to distinct cellular functions: phosphorylation plays a key role in signal transduction and cell cycle control; acetylation and methylation regulate transcription and metabolism; glycosylation is essential for protein folding and cell adhesion; and ubiquitination governs protein degradation and localization. PTMs occur across different cellular compartments, including the nucleus, cytoplasm, endoplasmic reticulum, and Golgi apparatus. This widespread distribution ensures precise regulation of cellular pathways (Ramazi and Zahiri 2021; Zhong et al. 2023; Fan et al. 2015).

The regulation of PTMs depends not only on the activity of enzymes that catalyze these modifications but also on the availability of metabolic precursors, which can vary based on cellular and environmental conditions.

1.4.2. Metabolic control and tissue-specific regulation of PTMs

In response to fluctuations in metabolic or in environmental conditions, tissues dynamically adjust their metabolic pathways to maintain homeostasis. For instance, during fasting, glycogen stores are depleted, prompting a shift in substrate utilization from carbohydrates to lipid oxidation to conserve glucose for essential organs such as the brain. Skeletal muscle, as a metabolically adaptable tissue, plays a major role in this transition by modulating energy and nutrient-sensing pathways that coordinate fuel selection and metabolic efficiency (Wijngaarden et al. 2014).

The brain, as a highly energy-demanding organ, relies on tightly regulated metabolic processes to sustain neuronal activity and synaptic function. Unlike other tissues, brain has a limited capacity for energy storage and depends primarily on a continuous supply of glucose as its main fuel source. During periods of high neuronal activity, local cerebral blood flow increases to ensure the delivery of oxygen and nutrients required for ATP production. In addition to glucose metabolism, neurons and glial cells engage in metabolic crosstalk, exchanging key metabolites such as lactate, glutamine, and lipids to maintain energy balance and biosynthetic processes. Astrocytes, for instance, play a crucial role in supplying neurons with lactate, which can be converted into pyruvate and oxidized in mitochondria for ATP generation (Chausse et al. 2024; Rae et al. 2024; Falkowska et al. 2015). Microglia, the brain's resident immune cells, undergo metabolic reprogramming in response to environmental cues, shifting between glycolysis and oxidative phosphorylation to support their functional state.

These metabolic shifts not only influence energy balance but also impact the availability of PTM precursors (Pataky et al. 2024; Fan et al. 2015), thereby regulating protein modifications in a tissue-specific manner. Among these modifications, arginine methylation is particularly sensitive to metabolic conditions, as it relies on S-adenosylmethionine (SAM) as a methyl donor. SAM is generated through the one-carbon metabolism pathway, which is closely linked to nutrient availability including folate and methionine levels (Mentch and Locasale 2016; Ouyang et al. 2020; Serefidou, Venkatasubramani, and Imhof 2019). Given the brain's high metabolic demands, fluctuations in precursor availability can influence arginine methylation patterns, ultimately affecting protein-protein interactions, RNA processing, transcriptional regulation, and signaling (Guo et al. 2014; Boisvert, Chénard, and Richard 2005; Zakrzewicz et al. 2012). In neurons and glial cells, dynamic methylation of arginine residues modulates key signaling pathways, ensuring proper cellular function and adaptation to metabolic changes (Qualmann and Kessels 2021). Due to its dependence on metabolic precursors, arginine methylation plays an important role in regulating cellular responses to metabolic fluctuations, influencing key processes such as transcriptional regulation and signaling.

PTMs are central to regulating protein function and cellular responses, including adaptations to metabolic changes. Their ability to fine-tune protein activity extends to highly specialized processes such as pre-mRNA splicing, where PTMs of splicing machinery components ensure the precision and adaptability of gene expression in eukaryotes.

1.4.3. PTMs of splicing machinery

Posttranslational modifications (PTMs) play a crucial role in modulating the dynamics of ribonucleoprotein complexes and spliceosome-associated proteins. They contribute to the precise regulation of pre-mRNA splicing and linking it to gene expression in eukaryotes. As a result, research on how PTMs influence splicing regulation has gained increasing attention. Among all PTMs, acetylation, ubiquitination, phosphorylation, sumoylation, and methylation are the most important ones in this process (Kretova et al. 2023).

Acetylation can influence protein stability, DNA binding, localization, and transcriptional activity (McKay and Johnson 2010). For example, acetylation of the splicing factor Sam68 by acetyltransferase p300 increases its activity by strengthening its RNA-binding activity (Siam et al. 2019; Babic, Jakymiw, and Fujita 2004). Additionally, acetylation of splicing factor SRSF5 by histone acetyltransferase Tip60 under high glucose intake stabilizes SRSF5 proteins, modulating its activity in splicing (Yuhan Chen et al. 2018).

Ubiquitination involves in protein stability, localization, activity of proteins, and spliceosome assembly (Kretova et al. 2023). For instance, ubiquitin ligase TRAF6 ubiquitinates splicing factor hnRNPA1, influencing the splicing of Arhgap1. This process plays a role in self-renewal and differentiation of hematopoietic stem cells. Another example is the ubiquitin ligase PRP19. It ubiquitinates the splicing factors PRP3 and PRP31, stabilizing the tri-snRNP complex (Chanarat and Mishra 2018).

Phosphorylation regulates the assembly, catalysis and disassembly of spliceosomes (McKay and Johnson 2010), as well as the subcellular localization (Long et al. 2019). Phosphorylated SR proteins, SRSF1, SRSF3, and SRSF7, are imported to the nucleus by interacting SR-specific transporting proteins (Long et al. 2019). Similarly, tyrosine phosphorylation of the splicing factor Sam68 promotes the accumulation of Sam68 nuclear bodies. Moreover, phosphorylation of Sam68 diminishes its splicing by disrupting its binding with hnRNP A1 to the BCL-X pre-mRNA (Kretova et al. 2023).

Sumoylation affects pre-mRNA splicing by modifying spliceosomal components and influencing spliceosome assembly like pre-mRNA 3’ end processing, RNA binding by hnRNP proteins, and RNA editing (Acuña et al. 2023; Kretova et al. 2023). For example, ubiquitylation of the U4/U6 protein Prp3 is necessary for stabilization of the U4/U6.U5 tri-snRNP (Pozzi et al. 2017). Another example is the RNA-binding protein TDP-43, whose splicing activity is regulated by sumoylation in its N-terminal RRM1 domain. Sumoylated TDP-43 acts as a scaffold for the multiprotein complexes formations, ensuring proper spatial organization of splicing factors within the spliceosome and supporting their activity in the nucleus (Maraschi et al. 2021).

Methylation regulates gene expression, transcription, mRNA turnover, splicing, and protein function and stability (Han et al. 2019; Bedford and Clarke 2009). PRMT5, an arginine methyltransferase, has a role in the assembly of snRNPs. It chaperons Sm proteins and methylates SNRPD1, SNRPD3, and SNRPB/B' posttranslationally, together with its cofactors pICln and MEP50, respectively. Methylated Sm proteins are then imported into SMN assembly factor for further processing and subsequent nuclear import (Maron et al. 2022). Additionally, PRMT5 methylates SRSF1, enhancing spliceosome assembly. Inhibition of PRMT5 negatively affects spliceosome assembly, resulting in exon skipping and intron retention with weak 5' splice donor sites (Q. Wu et al. 2021). Another arginine methyltransferase, PRMT9, is involved in the maturation of the U2 snRNP, where it associates with the splicing factors SAP145 and SAP49. PRMT9 methylates SAP145, linking it to the early steps of splicing by allowing SAP145 to bind the branch point sequence (Kretova et al. 2023).

Among the various PTMs that regulate splicing, arginine methylation stands out as a critical modification due to its widespread role in modulating spliceosome assembly and activity. This process is tightly controlled by a network of enzymes and proteins, including writers, erasers, and readers, that recognize and interpret methylated arginine residues.

1.4.4. Regulators of arginine methylation: writers, erasers, readers

Arginine methylation is controlled by several enzymes and proteins, regulating the addition, removal, and recognition of methyl groups on arginine residues on target proteins. Writers and erasers are the enzymes adding or removing methyl groups, respectively (Figure 1. 7). Finally, readers are the proteins recognizing and binding to methylated arginine residues, and interpreting the biological signals encoded by arginine methylations (Biswas and Rao 2018).

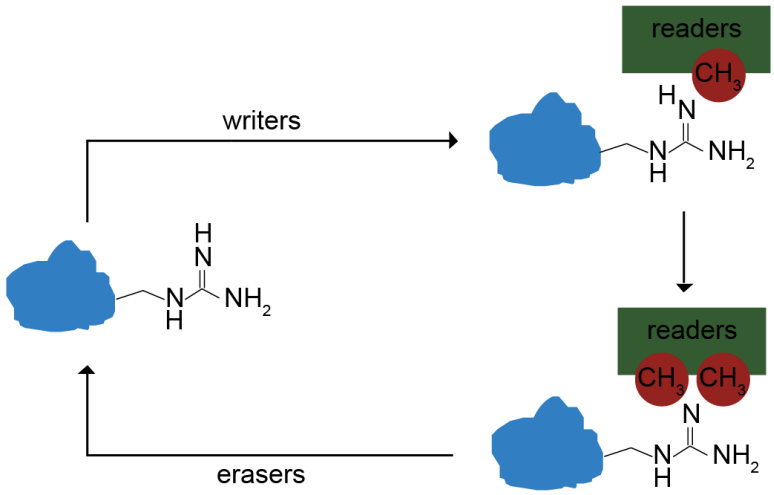

Figure 1. 7. Enzymatic regulators of protein arginine methylation: Writers, readers, and erasers. (Adapted from Xie et al. 2024)

1.4.5. Writers of arginine methylation: protein arginine methyltransferases (PRMTs)

Writers of arginine methylation, protein arginine methyltransferases (PRMTs), are the enzymes that catalyze the transfer of methyl groups from SAM to the guanidinium nitrogen atoms of the arginine residues (Xie et al. 2024; Bryant, Heiss, and Banasavadi-Siddegowda 2021; Al-Hamashi, Diaz, and Huang 2020). Mammals generate three main forms of methylated arginine including monomethylarginine (MMA), asymmetric dimethylarginine (ADMA), and symmetric dimethylarginine (SDMA).

To date, there are nine identified protein arginine methyltransferases (PRMTs), and they are classified into three based on their catalytic activities. Type I PRMTs, including PRMT1, PRMT2, PRMT3, PRMT4 (CARM1), PRMT6, and PRMT8, catalyze the formation of MMA and ADMA (Figure 1. 8). Type II PRMTs, consisting of PRMT5 and PRMT9, generate MMA and SDMA. The only type III PRMT, PRMT7, exclusively catalyzes the formation of MMA (Zhong et al. 2023; Al-Hamashi, Diaz, and Huang 2020; Bryant, Heiss, and Banasavadi-Siddegowda 2021; Qualmann and Kessels 2021; Guo et al. 2014; Musiani et al. 2019). In addition to these nine PRMTs, two potential PRMTs, PRMT10 and PRMT11, have been predicted to show type II activity (Qualmann and Kessels 2021). In summary, all PRMTs can mediate monomethylation of arginine residues, type I enzymes introduce a second methyl group asymmetrically to form ADMA, whereas type II enzymes generate SDMA through symmetric dimethylation.

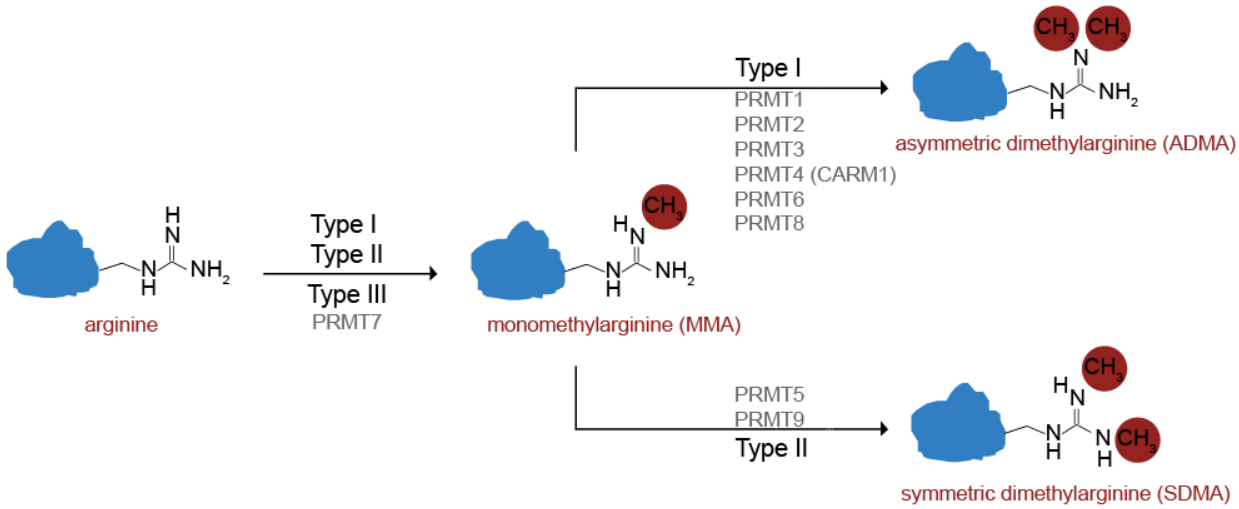

Figure 1. 8. Three types of protein arginine methyltransferases. (Adapted from Samuel et al. 2021)

The majority of PRMT substrates contain glycine- and arginine-rich (GAR) motif, while PRMT4 (CARM1) primarily methylates arginine residues within proline-, glycine- and methionine-rich (PGM) motif. PRMT5 is capable of methylating both GAR and PGM motifs. While most PRMTs exhibit ubiquitous expression, PRMT8 is specifically expressed in neurons. PRMTs mediate different methylation processes, influencing a variety of cellular functions like gene expression regulation, splicing, synaptic plasticity, and DNA repair (Table 1. 2) (Azhar et al. 2023; Shiquan Shen et al. 2024; Yalong Wang and Bedford 2023; Tewary, Zheng, and Ho 2019; Hartley and Lu 2020; Dong, Li, and Lai 2021).

PRMT4, PRMT5, and PRMT7-mediated methylation has been implicated in RNA processing, particularly in pre-mRNA binding and alternative splicing regulation. In particular, PRMT4 and PRMT7 are connected to splicing because they can directly methylate splicing factors. For example, PRMT4 methylates CA150, U1C and SAP49 splicing factors. PRMT4 also either mono- or dimethylates SNRPB/B' at multiple arginine residues, including R94, R108, R112, R132, R147, R172, R181, R236, and R239 sites. Moreover, PRMT7 symmetrically dimethylates SNRPB/B', SNRPD1, SNRPD2, and SNRPD3, a modification essential for snRNP biogenesis. PRMT7-dependent methylation sites in SNRPB/B' include R108, R112, R132, R147, R172, and R181 (W.-J. Li et al. 2021).

While PRMTs establish arginine methylation patterns, these modifications must also be reversible to allow dynamic regulation of cellular processes. This reversibility is achieved by erasers, such as demethylases, which remove methyl groups and reset the functional state of proteins.

Table 1. 2. Classification, recognized motifs, functions, and expression patterns of PRMTs. (GAR: glycine- and arginine-rich, PGM: proline-, glycine- and methionine-rich)

Type	PRMT	Motif	Expression	Functions	References
I	PRMT1	GAR	Ubiquitous	Gene expression regulation, cell cycle regulation, DNA repair, tumor development, formation of astrocytes, oligodendrocytes, and neurons	(Azhar et al. 2023; Shiquan Shen et al. 2024; Yalong Wang and Bedford 2023; Angelopoulou et al. 2023)
	PRMT2	GAR	Ubiquitous	Cell proliferation of renal cell carcinoma	(Yalong Wang and Bedford 2023; Z. Li et al. 2023)
	PRMT3	GAR	Ubiquitous	Maturation of 80S ribosome	(Tewary, Zheng, and Ho 2019; Yalong Wang and Bedford 2023)
	PRMT4 (CARM1)	PGM	Ubiquitous	Maintenance of stem cell pluripotency, splicing, muscle cell differentiation, T-cell development	(Azhar et al. 2023; Hartley and Lu 2020)
	PRMT6	GAR	Ubiquitous	Transcriptional regulation, cell cycle regulation, DNA excision repair, cell fate determination	(Tewary, Zheng, and Ho 2019; Yalong Wang and Bedford 2023)
	PRMT8	GAR	Cerebral cortex, hippocampus, cerebellum	Regulation of synaptic plasticity and cognitive functions, maturation of synapse and neuronal circuit	(Hartley and Lu 2020; Yalong Wang and Bedford 2023; Dong, Li, and Lai 2021)
II	PRMT5	GAR or PGM	Ubiquitous	Cell proliferation, DNA repair, cell differentiation, splicing, signal transduction, oligodendrocyte differentiation	(Azhar et al. 2023; Hartley and Lu 2020; Angelopoulou et al. 2023)
	PRMT9	Not well characterized	Ubiquitous	Maturation of U2 snRNP	(Tewary, Zheng, and Ho 2019)
III	PRMT7	RXR	Ubiquitous	DNA repair, biogenesis of nuclear ribonucleoprotein particle	(Tewary, Zheng, and Ho 2019; Yalong Wang and Bedford 2023; S.-Y. Lee et al. 2020)

1.4.6. Erasers of arginine methylation: demethylases

Erasers of arginine methylation, demethylases, remove the methyl groups from the guanidinium nitrogen atoms of the arginine residues. Two primary demethylases have been implicated in protein arginine demethylation: Peptidylarginine deiminase 4 (PAD4) and Jumonji domain-containing protein 6 (JMJD6) (Zhong et al. 2023).

PAD4 catalyzes the conversion of methyl-arginine into citrulline, a process that leads to the release of methylamine. This enzyme targets histone H3 and H4 from different sites, including those methylated by coactivators PRMT1 (H4R3) and PRMT4 (H3R17). PAD4 is not classified as a typical demethylase because it is unable to demethylate dimethylated arginine and can also modify unmodified arginine (Biswas and Rao 2018; Zhong et al. 2023).

JMJD6 catalyzes the demethylation of histone H3R2 and H4R3 through hydroxylation of the methyl group, converting them into formaldehyde. This reaction could be catalyzed by dioxygenases, using iron to deactivate a dioxygen molecule and form hydroxylated substrates (Trewick, McLaughlin, and Allshire 2005). JMJD6 has been shown to remove monomethylated, symmetric- and asymmetric-dimethylated arginine residues. However, its function remains controversial, as JMJD6 was shown to act as lysine hydroxylase in another study, catalyzing lysyl-5-hydroxylation of U2AF65 (65-kDa subunit of splicing factor U2AF). While more evidence supporting arginine demethylation is likely to emerge, distinguishing whether JMJD6 primarily functions as an arginine methylation or a lysine hydroxylation remains a challenge (Pham, Tao, and Yang 2023).

Once arginine methylation is established or removed, the biological significance of these modifications depends on their recognition by effector proteins known as readers. Tudor domain-containing proteins serve as key interpreters of methylated arginine marks, linking these modifications to downstream signaling pathways and cellular functions.

1.4.7. Readers of arginine methylation: Tudor domain proteins

Modification of arginine through methylation can lead to structural changes in proteins, and create docking sites for specific effector proteins. Tudor domain-containing proteins serve as the primary readers of arginine methylations. These domains, which are approximately 60 amino acids in length, utilize conserved aromatic residues to construct an “aromatic cage” that facilitates binding to methylated arginine (Erce et al. 2012; Pham, Tao, and Yang 2023; Yalong Wang and Bedford 2023). Thanks to their aromatic residues, Tudor domain-containing proteins act as scaffolds that connect methylarginine to downstream effector proteins with distinct catalytic activities. Through this mechanism, methylation signals are interpreted and transmitted, contributing to the regulation of essential cellular processes (Pham, Tao, and Yang

2023). For example, Tudor domain of SMN protein recognizes symmetric dimethylarginine (SDMA) marks on Sm proteins, which are introduced by PRMT5. This interaction promotes the functional small nuclear ribonucleoprotein complex assembly, essential for spliceosome function (Q. Wu et al. 2021).

In humans, there are approximately thirty-six Tudor domain-containing proteins, but more than eighty Tudor domains, as many proteins have more than one copy of this domain. These Tudor domain-containing proteins can be categorized into those that bind methylated arginine and those that methylated lysine. Methyllysine motifs are recognized by at least eight distinct domain types, including Tudor, Chromo, PWWP, MBT, PHD, Ank, WD40 and BAH. However, among these, only the Tudor domain family has been identified to recognize methylated arginine. Tudor domain reading methylarginine motifs do not read methyllysine motifs, and vice versa (Erce et al. 2012; Pham, Tao, and Yang 2023; Yalong Wang and Bedford 2023).

Structural studies indicate that methylarginine-binding Tudor domains create a relatively narrower cage compared to the ones interacting with methyllysine, although their binding preferences cannot be predicted based on their amino acid sequences (Erce et al. 2012; Pham, Tao, and Yang 2023; Yalong Wang and Bedford 2023).

In addition to SMN, the primary methylarginine-binding Tudor domains identified so far belong to SPF30 (Splicing Factor 30), and members of the TDRD family, including TDRD1, TDRD2, TDRD3, TDRD6, TDRD9, and TDRD11 (Blanc and Richard 2017; Yalong Wang and Bedford 2023). Given the role of Tudor domain proteins in recognizing PRMT-mediated methylation, recent proteomics studies have aimed to explore how these modifications regulate splicing factors at a global level.

While Tudor domain-containing proteins interpret methylarginine marks, recent proteomics studies have provided insights into how PRMTs establish these marks and regulate splicing factors on a global scale.

1.4.8. Proteomics studies on arginine methylation in splicing factors

Recent proteomics analysis have highlighted the critical role of arginine methylation in regulating splicing factors, with PRMTs acting as key regulators, specifically PRMT4 (CARM1), PRMT5, and PRMT7. The heptameric Sm ring members of the spliceosome complex are among the most prominent PRMT substrates. Comparative methylome analysis revealed that although PRMT4, PRMT5 , and PRMT7 modify proteins involved in similar pathways, such as spliceosome assembly and RNA transport, each PRMT primarily acts on distinct substrates. This suggests that, despite their functional overlap, these PRMTs have non-redundant regulatory roles (W.-J. Li et al. 2021).

Larsen et al. performed a proteome-wide approach to identify and quantify arginine methylation sites, revealing previously uncharacterized roles of arginine methylation in splicing factor regulation. Their study demonstrated that PRMT4 depletion increased the accumulation of SRSF2 in nuclear speckles, suggesting that PRMT4-mediated methylation normally prevents this localization. Moreover, they showed PRMT5 depletion inhibited SRSF2 from RNA binding (Larsen et al. 2016).

While proteomics studies have advanced the understanding of how arginine methylation regulates splicing factors, dysregulation of these modifications can disrupt cellular processes, contributing to the development of various diseases.

1.4.9. Diseases associated with arginine methylation

Defects in arginine methylation, mainly mediated by PRMTs, are implicated in various diseases, including neurodegenerative diseases, cancer, and pulmonary diseases. The dysregulation may contribute to disease progression by altering key cellular processes (Angelopoulou et al. 2023).

In neurodegenerative diseases, several PRMTs play a role in pathological mechanisms. PRMT4, PRMT5, and PRMT8 have been implicated in Alzheimer's disease, where they influence signaling pathways that drive beta-amyloid accumulation, tau phosphorylation, neuroinflammation, and cell death. Similarly, PRMT1 has been linked to amyotrophic lateral sclerosis, where its dysregulation leads to abnormal cytoplasmic accumulation of FUS. This accumulation contributes to cytoplasmic inclusion, stress granule aggregation, and cellular toxicity (Angelopoulou et al. 2023).

Beyond neurodegeneration, dysregulations of PRMTs are associated with cancer. For example, PRMT5 dysregulation is linked to various cancers through its role in p53 arginine methylation, which alters its biochemical properties and functional response to DNA damage. This modification influences the activation of target genes involved in p53-dependent growth arrest, such as p21, NOXA, APAF1, and PUMA (Zakrzewicz et al. 2012).

Finally, PRMT1 has been linked to asthma through its role in T lymphocyte activation, a key process in airway inflammation. Specifically, PRMT1 methylates the NIP45, enhancing NFAT activity. This modification promotes cytokine production in T lymphocytes, contributing to the inflammatory response characteristic of asthma (Zakrzewicz et al. 2012). Since PRMTs are involved in several diseases, targeting arginine methylation has gained importance as a promising therapeutic strategy.

The critical role of PRMTs in disease progression has led to interest in targeting these enzymes as a therapeutic strategy. Developing PRMT inhibitors offers a promising approach to modulate arginine methylation and restore normal cellular function.

1.4.10. Inhibitors of arginine methylation

The development of PRMT inhibitors has provided understanding of their structural and functional mechanisms, contributing to the therapeutic applications (Q. Wu et al. 2021).

Currently, several PRMT1 and PRMT5 inhibitors are in the ongoing clinical trials. GSK3368715, a selective type I inhibitor, is undergoing Phase I trials for solid tumors and hematologic tumor of diffuse larger B-cell lymphoma. It is aimed to determine its therapeutic activity and maximally tolerated oral dose. PRMT5 inhibitor JNJ46419178 is being tested in patients having refractory B cell non-Hodgkin lymphoma (NHL) or advanced solid tumors. Moreover, phase I trials for another PRMT5 inhibitor, PF-06939999, are currently in progress to evaluate its safety, pharmacokinetics, and pharmacodynamics in patients with advanced or metastatic solid tumors (Al-Hamashi, Diaz, and Huang 2020).

Research on PRMT inhibitors has led to the discovery of selective compounds for other PRMTs (Al-Hamashi, Diaz, and Huang 2020). SGC707, a selective inhibitor of PRMT3, was developed through structure-based optimization and has shown promise in preclinical studies. TP-064 and EZM2302, two highly selective PRMT4 inhibitors, have shown efficacy against multiple myeloma in preclinical settings (Biswas and Rao 2018). PRMT6 inhibitors have also progressed. EPZ020411 has emerged as a promising candidate for reducing H3R2me2a levels. Its clinical applications require further research (Z. Chen et al. 2022). There are still many ongoing studies about PRMT inhibitors, showing great promise for future therapies.

1.5. Aim

Gene duplication events often result in gene paralogues – two copies of a gene in the same species – that are either lost or become pseudogenes over time. However, SNRPB and SNRPN, which originated from a duplication event over 90 million years ago, have been retained with high sequence similarity. Despite their similarity, they show clear differences in expression and regulation: *SNRPB* is ubiquitously expressed and biallelic, while *SNRPN* is expressed exclusively in brain and heart and is subject to genomic imprinting. These differences suggest that SNRPB and SNRPN have acquired distinct regulatory and functional properties that are not yet fully understood.

Importantly, these two paralogues are not functionally redundant – they do not compensate for each other. Their dysfunction is also linked to different diseases: mutations in SNRPB are associated with Cerebro-Costo-Mandibular syndrome (CCMS), a skeletal disorder, while loss of SNRPN expression contributes to Prader-Willi syndrome (PWS), a neurodevelopmental disorder. Understanding how these closely related proteins diverge at the molecular level could help identify new therapeutic targets for these disorders.

While the structured Sm domain has been well studied due to its essential role in snRNP assembly, much less is known about the unstructured regions, including arginine-rich and proline-rich motifs, despite their potential roles in regulating protein behavior and interactions.

The main aim of this project was to investigate these less characterized regions and to identify protein-level differences between SNRPB and SNRPN that might explain their specialized roles. More specifically, during my PhD, we aimed to:

1. Identify intrinsic differences between SNRPB and SNRPN, with a particular focus on their unstructured regions
2. Investigate whether translation-related mechanisms influence their posttranslational modification patterns
3. Explore why SNRPN, but not SNRPB, may be more sensitive to changes in translation
4. Determine whether these molecular differences affect their interaction networks or functional roles in the spliceosome
5. Evaluate whether these differences are also present in a physiological context

By addressing these questions, this study aims to better understand how two highly similar proteins can evolve distinct regulatory mechanisms and disease associations, and how subtle molecular features can drive paralogue-specific specialization.

2. Materials

2.1. Devices

Table 2. 1. List of devices used in this project.

Devices	Manufacturer	Catalogue Number
Balance	Sartorius	ED822-0CE
BD LSRFortessa SORP	BD Biosciences	
Biological Safety Cabinets	Dometic	BSC-SG403 N
Biorupture Pico Sonication Device	Diagenode	P2-210225
Centrifuge	Eppendorf	5427 R
Centrifuge	Thermo Scientific	Heraeus Multifuge X3
ChemiDoc™ Touch Gel Imaging System	Bio-Rad	
Color Sprout Plus Mini Centrifuge	Biozym	552031
Concentrator Plus	Eppendorf	5305000703
DS-11 FX+ Spectrophotometer/Fluorometer	DeNovix	DS-11 FX+
DynaMag™-2 Magnet	Thermo	12321D
Forma™ Steri-Cult™ CO2 Incubator, 232L	Thermo Scientific	3308
Freezer (-20)	Liebherr	LIE-LGex3410
Freezer (-80)	Sanyo	MDF-U74V
Fridge (4ºC)	Liebherr	LIE-FKex3600-20
Fume Hood	Wesemann Laboreinrichtungen	Delta System 30
Immobilon®-P^{SQ} Membrane, PVDF, 0.2 µm, 8.5 cm x 10 m roll	Merck	ISEQ85R
LightCycler 480 System	Roche	5015243001
Microwave	Samsung	MS8F303TAS

Mini Trans-Blot® Cell	Bio-Rad	153 BR110673
Multipette® E3x	Eppendorf	4987000029
Objective	Leica Microsystems	10450167
Pellet Mixer	VWR	431-0100
Pico™ 21 Microcentrifuge	Thermo Fisher	75002475
PIPETBOY acu	Integra	612-0928
Pipette (10 µL)	Eppendorf	3125000010
Pipette (2.5 µL)	Eppendorf	123000012
Pipette (20 µL)	Eppendorf	3123000039
Pipette (200 µL)	Eppendorf	3123000055
Pipettes (1000 µL)	Eppendorf	3123000063
PowerPac™ Basic Power Supply	Bio-Rad	1645050
Rotator Test Tube Rotator	Kisker Biotech Gmbh	Test Tube Rotator
Stereo Microscope	Leica Microsystems	M80
Sapanisertib (INK-128)	MedChemExpress	HY-13329
ThermoMixer	Eppendorf® ThermoStat C	EP5383000035
Tissue Culture Coverslips 13 mm (Plastic)	Starstedt	83.1840.002
Transmitted Light Base	Leica Microsystems	TL5000
VisiScope 5 Elements Fluorescence Spinning Disc confocal microscope	Visitron Systems	
Vortex Genie 2	Scientific Industries	P505.1
XCell *SureLock*™ Electrophoresis Cell	Invitrogen	EI0001
Stellaris 8 Falcon confocal microscope	Leica Microsystems	n.a.
HC PL APO CS2 100x/1.4 NA oil-immersion objective	Leica Microsystems	11506372
HC PL APO CS2 63x/1.4 NA oil-immersion objective	Leica Microsystems	11506350

2.2. Consumables

Table 2. 2. List of consumables used in this project.

Consumables	Manufacturer	Catalogue Number
6-well plate	Sarstedt	83.392
12-well plate	Sarstedt	83.3921
24-well plate	Sarstedt	83.3922
48-well plate	Falcon	353078
96-well plate	Sarstedt	83.3924
Bacteria Tubes	Sarstedt	62.515.006
Bottle Top Filter 500 mL	Fisher Scientific	FB12566510
Cell Culture Dish 35-mm	Greiner	627160
Cell Culture Dish 60-mm	Falcon	353004
Cell Culture Dish 100-mm	Falcon	353003
Cell Culture Dish 150-mm	Falcon	353025
Combitips (0.1 mL)	Eppendorf	0030089405
Combitips (0.2 mL)	Eppendorf	0030089626
Combitips (0.5 mL)	Eppendorf	0030089421
Combitips (1 mL)	Eppendorf	0030089430
Combitips (5 mL)	Eppendorf	0030089456
Combitips (10 mL)	Eppendorf	0030089464
Cryovials (1.8 mL)	Sarstedt	72.397.992
Dressing tissue forceps	Merck	F4267
Falcon™ Round-Bottom Polystyrene Test Tubes	Fisher Scientific	10186360
Filter tips (2.5 µL)	Starlab	S1121-2710
Filter tips (200 µL)	Starlab	S1120-8710
Filter tips (1000 µL)	Starlab	S1122-1730

Filter tips low retention (2.5 µL)	Sarstedt	703.010.285
Filter tips low retention (200 µL)	Sarstedt	703.031.275
Filter tips low retention (1000 µL)	Sarstedt	703.050.375
LB plates	IMB Media Lab	L-20_P
LightCycler®480 Multiwell Plate 384, white	Roche	04 729 749 001
Luer-Lock Syringe	BD Plastipak	300865
PCR Tube, Flat Cap 0.2 mL	Starlab	I1402-8100
PCR Tubes, with Flat Caps, 0.2 mL 8-Strip	Starlab	I1402-3700
Pipette tips (for agarose-TBE-gels)	Sarstedt	703.03
SafeSeal Tube (1.5 mL)	Sarstedt	72.706
SafeSeal Tube (2 mL)	Sarstedt	72.695.500
Screw Cap Tube (15 mL)	Sarstedt	62.554.502
Screw Cap Tube (50 mL)	Sarstedt	62.547.254
Serological pipette (5 mL)	Corning	CLS4487
Serological pipette (10 mL)	Corning	CLS4488
Serological pipette (25 mL)	Corning	CLS4489
Serological pipette (50 mL)	Corning	CLS4490
Syringe filter 0.2 µm	Starlab	83.1826.001
Tips (10 µL)	Starlab	S1111-3210
Tips (200 µL)	Starlab	S1111-1716
Tips (1000 µL)	Starlab	S1111-8701

2.3. Antibiotics, inhibitors, chemicals

Table 2. 3. List of antibiotics, inhibitors, and chemicals used in this project.

Antibiotics, Inhibitors, Chemicals	Company	Catalogue Number
Accutase	Sigma Aldrich	A6964-100ML
Agarose	Sigma-Aldrich	cas 9012 366
Ampicillin	IMB Media Lab	A-10_A
Attachment Factor Protein 1X	Thermo Scientific	S006100
Bovine Serum Albumin (BSA) Fraction V (lyophilized powder)	Pan Biotech	P06-1391500
Bradford - Solution for Protein Determination	Panreac AppliChem ITW	A6932
cOmplete™, EDTA-free Protease Inhibitor Cocktail	Roche	11836170001
Cycloheximide	Sigma Aldrich	C7698-1G
DAPI (4',6-Diamidin-2-phenylindol, Dihydrochlorid)	Invitrogen	10184322
Dimethylsulfoxide (DMSO)	Sigma Aldrich	D8418-100ML
Direct-zol RNA MicroPrep Kit	Zymo	R2062
Direct-zol RNA Microprep Kits	Zymo Research	R2062
DL-Dithiothreitol (DTT)	Sigma Aldrich	D0632-25G
DMEM, high glucose, no glutamine	Gibco	11960044
DMEM/F12		11320-074
DNA ladder	Thermo Fisher	SM0331
dNTP mix	NEB	N0447S
Doxycycline Hyclate	Sigma Aldrich	D9891
DPBS, calcium, magnesium	Gibco	14040117
DS-437	Cayman	Cay29476-5
Dulbeccos's Phosphate Buffered Saline	Sigma	D8662
Essential 8 medium	Life Technologies	A1517001
Ethanol 100%	Thermo Fisher	10342652

FastStart Universal SYBR Green Master	Roche	4913914001
Fetal Bovine Serum	Gibco	A5256701
Geltrex	Life Technologies	A1413302
Gibson Assembly 2X MasterMix	IMB Protein Production	n.a.
GlutaMAX™ Supplement	Gibco	35050061
GlutaMAX™ Supplement 100x	Gibco	35050061
Glutaraldehyde Solution	Sigma Aldrich	G5882-50ML
Glycerol	Sigma Aldrich	G5516
Green Taq buffer (5X)	IMB Protein Production	n.a.
GSK591	Cayman	Cay18354-1
Helix NP(TM) NIR	Biozol	BLD-425301
HEPES	Sigma-Aldrich	H0887
hSMG1-inhibitor 11e	ProbeChem	PC-35788
Hygromycin	Sigma Aldrich	H3274-1G
InstantBlue Coomassie Protein Stain	Abcam	ab119211
Iodoacetamide	Sigma Aldrich	I6125
KnockOut Serum Replacement	Life Technologies	10828028
LB without Antibiotics	IMB Media Lab	L-10_M
L-Glutamine	Sigma Aldrich	49419
Methanol 100%	Sigma Aldrich	34860
MOPS (Fine White Crystals/Molecular Biology), Fisher BioReagents™	Fisher Scientific	BP308
N2 Supplement 100x	Gibco	17502048
NEB® 10-Beta Competent *E. coli* (High Efficiency)	NEB	C3019H
Non-essential Amino Acids (NEAA) 100x	Gibco	11140050
Nonfat Dry Milk	Cell Signaling	9999S
Nuclease-Free Water	Qiagen	129115
NuPAGE™ LDS Sample Buffer (4X)	Novex	NP0007
Opti-MEM™	Gibco	31985062
PBS (5X)	IMB Media Lab	P-20_L
Penicillin-Streptomycin (10.000 U/ml)	Gibco	15140122
PhosSTOP™	Roche	4906845001

Pierce™ 16% Formaldehyde (w/v), Methanol-free	Thermo Scientific	28906
Pladienolide B (Pla B)	Santa Cruz Biotechnology	sc-391691
Poly-D-Lysin	Gibco	A3890401
Poly-L-Lysine Hydrobromide	Sigma Aldrich	P1274
Porcine Pancreatic Elastase	Promega	V189A
Potassium Ferricyanide(III)	Sigma Aldrich	702587-50G
Potassium Hexacyanoferrate(II) Trihydrate	Sigma Aldrich	P3289-5G
PRMT4/CARM1 Inhibitor	Cayman	Cay11033-500
ProLong™ Diamond Antifade Mountant	Invitrogen	P36965
Puromycin	Sigma Aldrich	P8833
rCutSmart™ Buffer	NEB	B6004S
Recombinant Albumin, Molecular Biology Grade	New England Biolabs	B9200S
Rho kinase inhibitor InSolution Y-27632	Sigma-Aldrich	5092280001
RNaseZAP™	Sigma Aldrich	R2020-250ML
RNasin® Ribonuclease Inhibitor	Promega	N2515
ScreenFect®A	ScreenFect	S-3001
SuperSignal™ West Pico PLUS Chemiluminescent Substrate	Thermo Scientific	34577
SYBR Safe DNA Gel Stain	Thermo Fisher	S33102
Taq DNA Polymerase	IMB Protein Production	n.a.
TBE Buffer (10X)	IMB Media Lab	T-40_L
Thermo Scientific™ Pierce™ Anti-HA Magnetic Beads	Thermo Scientific	88836
Transfer Buffer 10X	IMB Media Lab	T-20_L
Triton-X	Sigma-Aldrich	X100-500ML
TRIZol™ Reagent	Invitrogen	15596026
TrypLE Express	Life Technologies	12604013
Trypsin	Sigma Aldrich	T6567
TWEEN® 20	Merck	P1379-1L
X-Gal	Sigma-Aldrich	9630

2.4. Kits

Table 2. 4. The list of kits used in this project.

Kits	Manufacturer	Catalogue Number
Direct-zol RNA MicroPrep Kit	Zymo Research	R2062
Quick Ligation Kit	NEB	M2200S
QuikChange Lightning Kit	Agilent Technologies	200518
Rapid DNA Dephos & Ligation Kit	Roche	4898117001
ZR Plasmid Miniprep-Classic	Zymo Research	D4054
Zymoclean Gel DNA Recovery Kit	Zymo Research	D4001

2.5. Homemade buffer recipes

Table 2. 5. List of homemade buffers used in this project.

Homemade Buffers	Recipe
MOPS 20X	50 mM MOPS, 50mM Tris Base, 0.1% SDS, 1 mM EDTA, pH 7.7
Cell lysis buffer for IP-MS	250 mM NaCl, 50 mM HEPES pH 7.6, 0.1% IGEPAL, 10 mM MgCl2, 10% glycerol
Cell lysis buffer for WB	100 mM NaCl, 50 mM HEPES pH 7.6, 0.1% IGEPAL, 10 mM MgCl2, 10% glycerol
Elution buffer	25 mM Tris-HCl pH 8.0, 1% [wt/vol] SDS
Henikoff buffer	0.1% SDS, 3 mM CaCl2, 20 mM Tris pH 8.0, 100 mM NaCl, 0.9% Triton-X
Wash buffer	0.1% SDS, 20 mM Tris pH 8.0, 1 mM EDTA, 400 mM NaCl, 0.9% Triton-X 100

2.6. Plasmids

Table 2. 6. List of plasmids used in this project.

pCK number	Common name
-	pcDNA™FRT⁄TO (commercial)
340	pHB-Cbx3P-mNEONGreen (HB-C-NG)
437	pFastBacDual-p10-mCherry_pCAG-MLE2xmyc_pSV40-BlastiR
546	pcDNA5-FRT-TO-Snrpb-2xHA-V5
549	pcDNA5-FRT-TO-Snrpb-2xHA-mNEON
561	pcDNA5-FRT-TO-Snrpb(1-60)-2xHA-mNEON (constructed by Claudia)
562	pcDNA5-FRT-TO-Snrpn-2xHA-V5-stop (constructed by Claudia)
563	pcDNA5-FRT-TO-Snrpn-2xHA-mNEON
565	pcDNA5-FRT-TO-2xHA-mNeon-Snrpn_14qD1
566	pOG44 (commercial, from Anton Khmelinski Lab)
575	pcDNA5-FRT-TO-Snrpb(1-90)-2xHA-mNEON
576	pcDNA5-FRT-TO-Snrpb(1-160)-2xHA-mNEON
577	pcDNA5-FRT-TO-Snrpb(1-190)-2xHA-mNEON
578	pcDNA5-FRT-TO-Snrpb(1-61)-SV40NLS-2xHA-mNEON
582	pcDNA5-FRT-TO-Snrpb(1-229)-Snrpn(230-240)-2xHA-mNEON
583	pcDNA5-FRT-TO-Snrpn(1-229)-Snrpb(230-231)-2xHA-mNEON
584	pcDNA5-FRT-TO-Snrpn(1-229)-2xHA-mNEON
585	pcDNA5-FRT-TO-Snrpb(1-90)-BamHI-Snrpb(168-231)-2xHA-mNEON
586	pcDNA5-FRT-TO-Snrpb(1-229)-2xHA-mNEON
595	pcDNA-FRT-TO-mCherry-T2A-2xHA-mNEON-Snrpb-STOP
596	pcDNA-FRT-TO-mCherry-T2A-2xHA-mNEON-Snrpn-STOP
665	pcDNA-FRT-TO-mCherry-T2A-2xHA-mNEON-Snrpb(191-231)-STOP
666	pcDNA-FRT-TO-mCherry-T2A-2xHA-mNEON-Snrpn(191-240)-STOP
700	pcDNA5-FRT-TO-Snrpn(Arg196Lys)-2xHA-mNEON

701	pcDNA5-FRT-TO-Snrpn(Pro198Gly)-2xHA-mNEON
702	pcDNA5-FRT-TO-Snrpn(Arg221Lys)-2xHA-mNEON
703	pcDNA5-FRT-TO-Snrpn(Arg196-221Lys)-2xHA-mNEON
707	pcDNA5-FRT-TO-Snrpb(Met227Ile)-2xHA-mNEON
712	pcDNA5-FRT-TO-Snrpn(Ile203Met)-2xHA-mNEON
715	pcDNA5-FRT-TO-Snrpn(Ile203-221Met)-2xHA-mNEON
720	pcDNA5-FRT-TO-Snrpb(Ile203-227Met)-2xHA-mNEON
721	pcDNA5-FRT-TO-Snrpb(Met203-213-227Ile)-2xHA-mNEON
722	pcDNA5-FRT-TO-Snrpn(Ile203-213-227Met)-2xHA-mNEON
723	pcDNA5-FRT-TO-Snrpb(Met188-203-213-227Ile)-2xHA-mNEON
724	pcDNA5-FRT-TO-Snrpn(Ile188-203-213-227Met)-2xHA-mNEON
725	pcDNA5-FRT-TO-Snrpn(Arg196-221-236Lys)-2xHA-mNEON
728	pcDNA5-FRT-TO-Snrpn(Arg236Lys)-2xHA-mNEON
729	pcDNA5-FRT-TO-Snrpn(Arg239Lys)-2xHA-mNEON
730	pcDNA5-FRT-TO-Snrpn(Arg236-239Lys)-2xHA-mNEON
731	pcDNA5-FRT-TO-Snrpn(Arg196-221-236-239Lys)-2xHA-mNEON
732	pcDNA5-FRT-TO-Snrpn(Arg196-221-228-236Lys)-2xHA-mNEON
735	pcDNA5-FRT-TO-Snrpn(Arg209Lys)-2xHA-mNEON
736	pcDNA5-FRT-TO-Snrpn(Arg196-209-221-236Lys)-2xHA-mNEON
737	pcDNA5-FRT-TO-Snrpn(Arg196-209-221-236-239Lys)-2xHA-mNEON
740	pcDNA5-FRT-TO-Snrpn(Arg196-209-221-228-236-239Lys)-2xHA-mNEON
741	pcDNA5-FRT-TO-Snrpn(Arg196-221-228-236-239Lys)-2xHA-mNEON
742	pcDNA5-FRT-TO-Snrpn(Arg209-236-239Lys)-2xHA-mNEON

2.7. Oligos

Table 2. 7. List of oligos used in this project.

Target (h: human, m: mouse)	Forward primer		Reverse primer	
	Internal name	Sequence (5'-3')	Internal name	Sequence (5'-3')
ACTIN (h)	q189	CAAGCAGGAGTATGACGAGTC	q190	TTTTGTCAAGAAAGGGTGTAACG
BRD2 (h)	q739	AGGTAATGTCACAGGATGGGAAGT	q740	CCCTGCTGCCTTTCTCTAACC
CDKN1B (h)	q733	GTAATGACCCTTTCCCAACCATAG	q734	CTAAGGTTAACACCCTCCAGCAG
C-MYC (h)	q759	AGGGAGATCCGGAGCGAATA	q760	AAGTTCCAGTGCAAAGTGCC
C-MYC (h)	q761	AGAGTTTCATCTGCGACCCG	q762	GAAGCCGCTCCACATACAGT
COX-2 (h)	q763	CCCACCCATGTCAAAACCGA	q764	ATCCTGTCCGGGTACAATCG
DNAJB1 (h)	q735	GGCCTGATGGGTCTTATCTATGG	q736	TTAGATGGAAGCTGGCTCAAGAG
GAPDH (h)	q745	AATGGGCAGCCGTTAGGAAA	q746	GCGCCCAATACGACCAAATC
HIF1a (h)	q755	CCCTGACAAGCCACCTGAG	q756	AGGAAAGGCAAGTCCAGAGG
HIF1a (h)	q757	AGCCAGATCTCGGCGAAGTA	q758	CCAGAAGTTTCCTCACACGC
HIF1a (h)	q715	CTGAACGTCTCAAAGGGCCA	q716	TCCTCTCCGAGCTACTCCTTT
HPRT (h)	q174	TGCTGAGGATTTGGAAAGGG	q175	ACAGAGGGCTACAATGTGATG
Hprt (m)	q074	GTATACCTAATCATTATGCCGAGGA	q075	GACATCTCGAGCAAGTCTTTCA
HygroR	q178	TCCATACAAGCCAACCACG	q037	GCATAACAGCGGTCATTGAC

NANOG (h)	q283	CAGAAATACCTCAGCCTCCAG	q284	TGCTATTCTTCGGCCAGTTG
Nanog (m)	q078	GAACTCTCCTCCATTCTGAACC	q079	TTGCTAGTCTTCAACCACTGG
Neon (m)	q046	CCGATGTACGTGTTCCGTAAG	q047	TGCCCATCACATCGGTAAAG
OCT4 (h)	q285	CAAGAACATGTGTAAGCTGCG	q286	TGGTTCGCTTTCTCTTTCGG
OTX2 (h)	q313	GAGGTGGCACTGAAAATCAAC	q314	GGCAGGTCTCACTTTGTTTTG
PAX6 (h)	q295	ACACCGTCATTTCAAACCATTG	q296	CGCCCCTAGTTAAAGTCTTCC
Pax6 (m)	q098	CCCTCACCAACACGTACAG	q099	TCATAACTCCGCCCATTCAC
PODXL (h)	q281	TTTCACCATGTCAGCCAGG	q282	GTCTGTTGAGTTCTTTGCGAG
RIOK3 (h)	q737	TCAATGGAGATAGCAAAGGTATTATAAC	q738	AGATTTACTTAGGAGCACATTATGAGTG
RNA18SN1 (h)	q741	GCAATTATTCCCCATGAACG	q742	GGCCTCACTAAACCATCCAA
RNA18SN5 (h)	q743	GAAACTGCGAATGGCTCATTAAA	q744	CACAGTTATCCAAGTGGGAGAGG
RPLP0 (h)	q170	TCAACGGGTACAAACGAGTC	q171	CCACAAAGGCAGATGGATCAG
Rplp0 (m)	q072	ACTGGTCTAGGACCCGAGAAG	q073	CTCCCACCTTGTCTCCAGTC
SNRPB (h)	q181	GTATCAGAGCCATCAGAACCG	q182	AGGTGCCAATGAAGATCCG
SNRPB-4 (h)	q768	CTGCAGGACTTGCTGGGC	q769	AGGTGGGTACTGGGTTGGAG
Snrpb (m)	q124	GCCTTTGACAAGCACATGAAC	q125	AGCAACACCAGACCAAGG
Snrpb-2 (m)	q126	AGGAACTCCAATGGGCATG	q127	GCCTCTGAGCTACTGACATAATG
Snrpb-3 (m)	q217	TGCAGCACATTGACTACAGGA	q218	AAAGGCTTTGAAGGTCCCGA

SNRPN (h)	q179	AGAACCTGCGTCATACCTTTATC	q180	TCTTGCTACTCTTGCCAACAG
Snrpn (m)	q118	AATTTGATCCTCTGTGATTGTGATG	q119	CAAGTTCTCCCCACGTAGC
Snrpn-2 (m)	q120	CGGGTTTTGGGTCTGGTC	q121	AGAGGCACACGAGCAATG
Snrpn-3 (m)	q122	CTAGCATTGCAGGAGCCC	q123	GGTCTCATACCAGGTGGAGG
SOX1 (h)	q297	GCCGTCTATGCTCCAGG	q298	AGGTCGGTCTCCATCATCA
TBP (h)	q172	GAGTTCTGGGATTGTACCGC	q173	GATTATATTCGGCGTTTCGGG
Tbp (m)	q068	CACCAATGACTCCTATGACCC	q069	AGCCAAGATTCACGGTAGATAC
Y chromosome (m)	n.a.	AGATGAAGATGCTGGTGGCACAGC	n.a.	GACTAGACATGTCTTAACATCTGTCC

2.8. Antibodies

Table 2. 8. List of primary and secondary antibodies for Western Blot used in this project.

Antibody	Clone	Manufacturer	Catalogue Number	Dilution	Reactivity
Carm1	n.a.	Biomol	A300-421A	1:10,000	Rabbit
GAPDH, HRP	GA1R	Invitrogen	MA5-15738-HRP	1:5,000	Bacteria, Chicken, Hamster, Human, I nsect, Mouse, Rat, Rabbit, Yeast
PCNA	PC-10	Santa Cruz Biotechnology	sc-56	1:5,000	Mouse
Phospho-Akt (Ser473)	D9E	Cell Signaling Technology	4060T	1:5,000	Rabbit
PRMT5	A-11	Santa Cruz Biotechnology	sc-376937	1:500	Mouse
Purified anti-HA.11 Epitope Tag	16B12	Biozol	BLD-901502	1:5,000	Mouse
RNA pol II	4H8	Active Motif	39097, 39047	1:6,000	Budding Yeast, C. elegans, Human, Mouse, Rat
Sm B/B'/N	12F5	Santa Cruz Biotechnology	sc-130670	1:2,000 in HEKS, 1:1000 in neurons	Mouse
TUBULIN	n.a.	abcam	44928	1:7,000	Mouse

Rabbit anti-Rat IgG (H+L) Secondary Antibody	n.a.	Invitrogen	A18917	1:10,000	Rabbit
Rabbit Anti-Mouse IgG H&L	n.a.	Abcam	ab46540	1:10,000	Mouse

Table 2. 9. List of primary and secondary antibodies for immunostainings used in this project.

Antibody	Clone	Manufacturer	Catalogue Number	Dilution	Reactivity
Coilin	F-7	Santa Cruz Biotechnology	sc-55594	1:300	Mouse
Purified anti-HA.11 Epitope Tag	16B12	Biozol	BLD-901502	1:1,000	Mouse
Sm B/B'/N	12F5	Santa Cruz Biotechnology	sc-130670	1:500	Mouse
Donkey anti-Mouse IgG (H+L) Highly Cross-Adsorbed Secondary Antibody, Alexa Fluor™ 555	n.a.	Invitrogen	A-31570	1:400	Mouse

3. Methods

3.1. Cloning different constructs

3.1.1. Cloning C-terminally tagged full length SNRPB and SNRPN into pcDNA™FRT/TO plasmid

Total RNA was isolated from mouse brains (embryonic for Snrpb, adult for Snrpn) and converted into complementary DNA (cDNA). Full length Snrpb (231 amino acids) and Snrpn (240 amino acids) were amplified from cDNA by using primer pairs containing two HA tags. Then, amplified sequences were cloned into pcDNA™FRT/TO plasmid using AscI and PacI restriction sites. After verification of those plasmids via Sanger Sequencing, mNEON tag was amplified from a pre-existing backbone and then cloned them. The resulting plasmids are given in Table 2. 6.

3.1.2. Cloning C-terminally tagged truncation mutations of SNRPB and SNRPN

Forward primer containing the BamHI site was designed to clone HA, mNeon and the backbone. Reverse primers, also containing the BamHI site, were designed to amplify the truncation mutants corresponding to amino acids 1-61, 1-90, 1-160, 1-190, and 1-229 of SNRPB, along with the backbone. After amplifying the regions of interests, the PCR products were digested with BamHI. Without dephosphorylation, the digested fragments were ligated using the Rapid DNA Dephos & Ligation Kit (Roche, 4898117001) and subsequently verified by Sanger Sequencing. Using the same strategy, truncation of SNRPN corresponding to its amino acids 1-229 was generated, with HA and mNEON tags. The resulting plasmids are given in Table 2. 6.

3.1.3. C-terminally tagged swapped mutations of SNRPB and SNRPN

A reverse primer containing BamHI site and the last 11 amino acids (aa230-240) of SNRPN was designed to clone swapped mutation of SNRPB. Similarly, another reverse primer with a BamHI site and the last 2 amino acids (aa230-231) of SNRPB was designed for the SNRPN mutation. The same forward primer used for cloning truncation mutations of SNRPB was used. After amplification, BamHI digestion, and ligation without dephosphorylation, the plasmids were verified via Sanger Sequencing. The resulting plasmids are given in Table 2. 6.

3.1.4. C-terminally tagged point mutations of SNRPB and SNRPN

Primers for introducing point mutations at selected amino acid residues were designed using Agilent QuikChange Primer Design tool (https://www.agilent.com/store/primerDesignProgram.jsp). C-terminally tagged full-length SNRPB and SNRPN plasmids were used as template. Point mutations were introduced using QuikChange Lightning Kit (Agilent Technologies, 200518), following the manufacturer's protocol, with reaction volumes halved. The resulting sequences were confirmed via Sanger sequencing and they are given in Table 2. 6.

3.1.5. N-terminally tagged full length SNRPB and SNRPN

N-terminally tagged full length SNRPB and SNRPN plasmids were cloned using Gibson Assembly. To achieve this, mCherry and HA-mNEON tags were amplified from pre-existing plasmids. A T2A sequence was added via primers. Full length SNRPB and SNRPN were then cloned from C-terminally tagged full-length SNRPB and SNRPN plasmids, respectively. The resulting plasmids are given in Table 2. 6.

3.1.6. N-terminally tagged truncation mutations of SNRPB and SNRPN

The sequences corresponding to SNRPB (aa191-231) and SNRPN (aa191-240) were amplified from N-terminally tagged full-length SNRPB and SNRPN plasmids, respectively, along with the backbone and the tags. Following BamHI digestion and ligation, sequences were verified via Sanger sequencing. The resulting plasmids are given in Table 2. 6.

3.2. Gibson assembly

Overlapping fragments for Gibson assembly were designed the Benchling tool. The backbones and inserts were amplified from their respective plasmids, ensuring overlap between fragments. After amplification, DNA concentrations were measured using a DS-11 FX+ Spectrophotometer/Fluorometer (DeNovix).

For the assembly, 100 ng backbone was combined with Gibson Assembly 2X Master Mix (IMB Protein Production Core Facility), water, and a 4-fold molar excess of the inserts in a 0.2 mL thin walled PCR tube, kept on ice. The reaction mixture was incubated at 50°C for 45 minutes.

3.3. Bacterial transformation

Cloned vectors were transformed into NEB® 10-beta Competent E. coli (High Efficiency) (NEB, C3019H) following the manufacturers' protocol.

3.4. Colony PCR and plasmid DNA isolation

Following bacterial transformation, individual colonies were picked using a pipet tip and placed into 8 uL of nuclease free water. A PCR master mix was prepared by combining 1.6 uL of Green Taq buffer (5X) (IMB Protein Production Core Facility), 0.1 uL of Taq DNA Polymerase (IMB Protein Production Core Facility), 0.16 uL of dNTP mix (NEB, N0447S), 0.4 uL of 10 μM forward primer, 0.4 uL of 10 μM reverse primer, and nuclease free water, making a total of 8 uL per colony. The same pipet tip used to pick the colony was then transferred into the PCR mixture. After removing the tip, the samples underwent PCR with the following thermal cycling conditions: initially denaturation at 95ºC for 3 min, followed by 24 cycles of denaturation at 94ºC for 20 sec, annealing at 55ºC for 20 sec, and elongation at 68ºC for 1 min/kb. A final extension at 68ºC for 5 min was followed by holding the samples at 10ºC.

The PCR products were analyzed by running them on an agarose gel, with the gel percentage selected based on the size of PCR product. Two selected plasmids were inoculated into LB medium (IMB Media Lab, L-10_M) supplemented with ampicillin (IMB Media Lab, A-10_A). The cultures were incubated at 37ºC with orbital shaking at 200 rpm for 16 hours. Plasmid DNA was isolated using the ZR Plasmid Miniprep-Classic (Zymo, D4054) kit according to the manufacturer's instructions. DNA concentrations were measured using a DS-11 FX+ Spectrophotometer/Fluorometer (DeNovix), and plasmid sequences were verified by Sanger sequencing.

3.5. Plasmid maintenance

Bacterial stocks were prepared by combining 800 uL of liquid bacterial culture with 800 uL of glycerol (Sigma Aldrich, G5516) in cryovials (Sarstedt, 72.397.992). The mixture was gently rotated to ensure even distribution before storage at -80ºC.

For bacterial recovery, a small portion of the frozen stock was scraped using a pipet tip and inoculated into LB medium (IMB Media Lab, L-10_M) supplemented with ampicillin (IMB Media Lab, A-10_A). The culture was incubated at 37ºC with orbital shaking at 200 rpm for 16 hours.

3.6. Maintenance of HEK293T and Snrpb/n cells

Flp-In™ T-REx™ 293 and generated Snrpb/n cell lines were cultured and maintained in 4.5 g/L glucose DMEM (Gibco, 11960044) supplemented with 9% fetal bovine serum (FBS) (Gibco, A5256701), 1% Penicillin/Streptomycin (Gibco, 15140122), and 1% GlutaMAX™ Supplement (Gibco, 35050061). The cells were grown in a humidifier incubator (Thermo Scientific) at 37 °C and 5% CO_2.

Media was changed every 2-3 days. To passage, cells were washed with PBS once and incubated in Accutase (Sigma-Aldrich, A6964-100ML) at 37 °C. Supplemented media was added on Accutase. Cells were collected with pipetting. Some of the cells were transferred to a new dish.

For freezing, cells were centrifuged at 1000 rpm for 3 minutes and resuspended in supplemented DMEM media described above and 10% DMSO. Cell suspension was aliquoted into cryovials and frozen at -80 °C overnight in Mr.Frosty, followed by transfer to -150 °C for long term storage.

For thawing, vials were warmed in a 37 °C water bath and diluted 1:1 in culture medium. Cells were centrifuged at 1000 rpm for 3 minutes, resuspended in fresh medium, and plated.

3.7. Cell line generation

The desired plasmids and the commercial Flp-recombinase expression vector pOG44 were co-transfected into Flp-In™ T-REx™ 293 cells using the transfection reagent ScreenFect®A (ScreenFect, S-3001), following the manufacturer's protocol for a 6-well format. Initially, Opti-MEM™ (Gibco, 31985062) was used for the transfection medium. After 6 hours, Opti-MEM™ was replaced with complete DMEM supplemented with 9% FBS, 1% Penicillin/Streptomycin, and 1% GlutaMAX™ Supplement.

The following day, the transfected cells were collected from the 6-well plate and seeded onto a 15-cm dish containing 300 ug/mL hygromycin (Sigma Aldrich, H3274) in complete DMEM. After two days of selection with 300 ug/mL hygromycin, the cells were maintained in 150 ug/mL hygromycin. Once colonies appeared, they were picked and seeded into 96-well plates with 150 ug/mL hygromycin. Cells were then expanded sequentially into 48-well, 24-well, 12-well, and 6-well plates maintaining 150 ug/mL hygromycin throughout. When cells reached confluency in 6-well plates, hygromycin was removed, and cells were maintained in complete DMEM.

Following colony expansion, the cells were further selected via X-Gal staining, and the protein expression was validated by Western Blot. To induce gene of interest expressions, doxycycline (Sigma Aldrich, D9891) was used.

3.8. X-Gal staining

Picked colonies were seeded into a 96-well plate along with HEK293T cells as a control. The next day, two different mixtures were prepared: "Mixture 1" contained 2% paraformaldehyde (Thermo Scientific, 28906) and 0.2% glutaraldehyde (Sigma Aldrich, G5882-50ML) in PBS (no

Ca, no Mg). “Mixture 2” contained 5 µM Potassium hexacyanoferrate(II) trihydrate (Sigma Aldrich, P3289-5G), 5 µM Potassium ferricyanide(III) (Sigma Aldrich, 702587-50G), 2 µM $MgCl_2$, and 1 ug/uL X-Gal in PBS (no Ca, no Mg).

Cells were washed with PBS (no Ca, no Mg). After removing the PBS, 50 uL of “Mixture 1” was added to each well and incubated for 10 min at room temperature. Following two washes with PBS (no Ca, no Mg), 50 uL of “Mixture 2” was added. The plate was covered with aluminum foil and incubated at 37ºC until a blue color developed in HEK293T cells. Colorless colonies were selected for further experiments, while blue colonies were discarded.

3.9. Maintenance of human induced pluripotent stem cells (hiPSCs)

Human induced pluripotent stem cells (hiPSCs, Kolf 2.1 iPSC WT NGN2-EMX1-BFP) received from our collaboration partner (Mühlemann Group, Bern) were cultured and maintained in Essential 8 medium (Life Technologies, A1517001) supplemented with 1% Penicillin/Streptomycin in a humidifier incubator at 37 °C and 5% CO_2. Cells were cultured on dishes coated with Geltrex (Life Technologies, A1413302) following the protocol of manufacture.

The media was changed daily. Cells were checked daily for differentiation. Differentiated cells were removed via scraping. To passage, cells were washed twice and then incubated for 2 minutes with PBS containing 0.5 mM EDTA at 37 °C. After removing PBS containing 0.5 mM EDTA, E8 media supplemented with 1% Penicillin/Streptomycin was added and cells were collected via scraping. Some of detached cells were transferred to a new dish.

For freezing, cells were centrifuged at 120G for 3 minutes and resuspended in cold culture medium supplemented with 20% KnockOut Serum Replacement (KOSR, Life Technologies, 10828028) and 10% DMSO. Cell suspension was aliquoted into cryovials and frozen at -80 °C overnight in Mr.Frosty, followed by transfer to -150 °C for long tern storage.

For thawing, vials were warmed in a 37 °C water bath and diluted 1:9 in culture medium. Cells were centrifuged at 120G for 3 minutes, resuspended in fresh medium, and plated. 10 µM Rho kinase inhibitor InSolution Y-27632 (ROCKi, Sigma-Aldrich, 5092280001) was added to promote cell attachment.

3.10. Differentiation of hiPSCs to neurons

hiPSCs (Kolf 2.1 iPSC WT NGN2-EMX1-BFP) stably expressing PiggyBac-integrated doxycycline-inducible NGN2 were differentiated into neurons following a modified protocol based on (Fernandopulle et al. 2018).

On day 0, for induction, hiPSCs at a 70-80% confluency were dissociated with TrypLE Express (Life Technologies, 12604013) and resuspended in induction medium consisting of DMEM/F12 (Gibco, 11320-074), N2 Supplement 100x (Gibco, 17502048), Non-essential Amino Acids (NEAA) 100x (Gibco, 11140050), GlutaMAX™ Supplement 100x (Gibco, 35050061), and 1 M of HEPES (Sigma-Aldrich, H0887). ROCK inhibitor (1:1000, 10 µM final) and doxycycline (2 µg/mL final, Sigma-Aldrich, D9891) were added to induce NGN2 expression.

500,000 cells/well were plated onto Geltrex-coated 6-well plate in induction medium. Cells were incubated at 37 °C and 5% CO_2. Media was changed daily with fresh induction medium containing doxycycline (no ROCKi from Day 1 onward).

On day 3, cells were dissociated using TrypLE Express, counted, and seeded at 900,000 cells/well in 1.5 mL maintenance medium on Geltrex-coated plates. Final plating medium was BrainPhys™ Neural Medium (STEMCELL™ TECHNOLOGIES, 05790) supplemented with B27 50x (with vitamin C), 10 ng/mL of BDNF (PeproTech, 450-02), 10 ng/mL of NT-3 (PeproTech, 450-03), and 1 µg/mL of Laminin (Sigma-Aldrich, L2020). BrDU (40 µM) was added during final plating to eliminate residual proliferating hiPSCs.

On the day after plating, the media was replaced with fresh maintenance medium without BrDU. Media changes were performed 1-2 times per week by replacing half of the medium. Neurons were used after 7 days of differentiation.

3.11. Maintenance of chicken embryonic cells

Chicken embryonic fibroblast cells (UMNSAH/DF-1), kindly provided by Prof. Dr. Julian König, were cultured and maintained under the same conditions as HEK293T cells.

3.12. Maintenance of F9 chicken embryonic cells

F9 cells were cultured and maintained in 4.5 g/L glucose DMEM (Gibco, 11960044) supplemented with 10% fetal bovine serum (FBS) (Gibco, A5256701), and 2 mM L-Glutamine (Sigma-Aldrich, 49419). The cells were grown in a humidifier incubator (Thermo Scientific) at 37 °C and 5% CO_2. Cells were cultured on dishes coated with Attachment Factor Protein 1X (Thermo Scientific, S006100). For this, 60-mm cell culture dish containing 1 mL of Attachment Factor Protein 1X was incubated in the humidifier incubator at 37 °C and 5% CO_2 minimum for 2-hours.

For freezing, cells were centrifuged at 200 G for 5 minutes and resuspended in 4.5 g/L glucose DMEM supplemented with 20% FBS and 10% DMSO. Cell suspension was aliquoted into

cryovials and frozen at -80 °C overnight in Mr.Frosty, followed by transfer to -150 °C for long term storage.

3.13. General treatment timeline and cell numbers

Day 0: Cells were seeded based on the experimental need. For example, $1.5x10^6$ cells/well in 6-well plate for Western Blot or $8x10^6$ cells/plate in 10-cm plate for Co-IP for HEKs.

Day 1: Cells were treated with Doxycycline at 0.1 µg/mL for WB or 0.025 µg/mL for immunofluoresce concentrations.

Day 2: Cells were treated with the required compound (e.g., cycloheximide).

Day 2, 3, 4 or 8 (depending on the compound): Cells were collected for RNA or protein isolation, or processed for other methodologies like immunofluoresce.

3.13.1. Cycloheximide (CHX) treatment

100 mg/mL stock solution of cycloheximide (CHX) (Sigma Aldrich, C7698-1G) was freshly prepared for each use by dissolving it in EtOH 100% (Thermo Fisher, 10342652). This stock solution was diluted in complete DMEM media (9% FBS, 1% Penicillin/Streptomycin, 1% GlutaMAX™ Supplement) to obtain a final working concentration of 100 µg/mL. Cells were then treated with this working solution for 4 hours.

3.13.2. PRMT4/CARM1 inhibitor treatment

10 mM of stock solution of PRMT4/CARM1 inhibitor (Cayman, Cay11033-500) was prepared in DMSO (Sigma Aldrich, D8418-100ML). This stock solution was diluted in complete DMEM to obtain a final working concentration of 5 µM. Cells were then treated with this working solution for 27 hours.

3.13.3. GSK591 treatment

5 mM of stock solution of GSK591 (Cayman, Cay18354-1) was prepared in DMSO. This stock solution was diluted in complete DMEM to obtain a final working concentration of 10 µM. Cells were then treated with this working solution for 6 days.

3.13.4. Puromycin treatment

5 mg/mL of stock solution of Puromycin (Sigma Aldrich, P8833) was prepared in water. This stock solution was diluted in complete DMEM media to obtain a final working concentration of 10 µM. Cells were then treated with this working solution for 3-8 hours.

3.13.5. Pladienolide B treatment

1 mM of stock solution of Pladienolide B (Pla B) (Santa Cruz Biotechnology, sc-391691) was prepared in DMSO. This stock solution was diluted in complete DMEM media to obtain a final working concentration of 100 nM. Cells were then treated with this working solution for 16 hours.

3.13.6. hSMG1-inhibitor 11e treatment

10 mM of stock solution of hSMG1-inhibitor 11e (ProbeChem, PC-35788) in DMSO was received from our collaboration partner (Mühlemann Group, Bern). This stock solution was diluted in complete DMEM media to obtain a final working concentration of 0.6 µM. Cells were then treated with this working solution for 24 hours.

3.14. RNA extraction and cDNA synthesis

After the required treatment, media was removed using suction pump. 300 µL of TRIZol™ Reagent (Invitrogen, 15596026) were added on cells. Cells were harvested by scraping in TRIZol and collected in a 1.5 mL tube. 300 µL of 100% Ethanol (Thermo Fisher, 10342652) was added onto cell- TRIZol mixture, and RNA was isolated using Direct-zol RNA MicroPrep Kit (Zymo, R2062), following the manufacturer's instructions. RNA concentrations were determined using a DS-11 FX+ Spectrophotometer/Fluorometer (DeNovix).

For cDNA synthesis, 5 µL of 250 ng RNA was used. To this, 0.435 µL of 0.1 mM oligo (dT) and 0.435 µL of 10 mM dNTP mix (NEB, N0447S) were added to the RNA. The mixture was heated at 65°C for 5 minutes and then immediately chilled on ice. Subsequently, 1.739 µL of 5X buffer (250 mM Tris-HCl, pH 8.0, 375 mM KCl, 15 mM $MgCl_2$), 0.87 µL of 0.1 M DTT (Sigma Aldrich, D0632-25G), 0.109 µL of RNasin® Ribonuclease Inhibitor (Promega, N2515) and 0.25 µL of M-MLV Reverse Transcriptase (IMB Protein Production Core Facility, 400 U/µL) were added to the mixture.

The final mixture was incubated at 25°C for 10 minutes, followed by 42°C for 50 minutes, and 70°C for 15 minutes. The resulting cDNA was then diluted with nuclease-free water (Qiagen, 129115) to a final volume of 250 µL.

3.15. Real-time quantitative polymerase chain reaction (RT-qPCR)

RT-PCR was performed using LightCycler 480 System (Roche). 3.5 uL of cDNA, 3.458 uL of FastStart Universal SYBR Green Master (Roche, 4913914001), 0.3 µM forward primer and 0.3 µM reverse primer were mixed in 384-well plate.

The samples were initially denatured at 95°C for 10 min (ramp rate 4.8°C/sec), followed by 45 cycles of denaturation at 95°C for 15 sec (ramp rate 4.8°C/sec), and annealing-elongation at 60°C for 1 min (ramp rate 2.5°C/sec), with single signal acquisition at each cycle. For the melting curve analysis, the samples were denatured at 95°C for 15 sec (ramp rate 4.8°C/sec), then held at 60°C for 1 min (ramp rate 2.5°C/sec), followed by a gradual melt at 95°C (ramp rate 0.11°C/sec) with continuous signal acquisition every 5°C. Finally, the samples were cooled at 40°C for 30 sec (ramp rate 2.5°C/sec). Cp values were determined using the Abs Quant/2nd Derivative Max analysis mode in LightCycler 480 software (version 1.5.1.62). The values were normalized against the geometric mean of Cp values from housekeeping genes.

3.16. RNA sequencing

RNA was extracted using Direct-zol RNA MicroPrep Kit (Zymo, R2062), and the concentrations were measured as detailed in the 3.11. Snap frozen RNA samples were submitted to the Genomics Core Facility for RNA sequencing.

A stranded mRNA library was prepared using Illumina mRNA Ligation Kit, and sequencing was performed on a NextSeq 2000 System and 2x100 read lengths. Data analysis was carried out by Dr. Frank Rühle from the Bioinformatics Core Facility.

3.17. Ribosome profiling data analysis

Ribosome profiling (GSM7430289, GSM7430290, GSM7430249, GSM7430250) and the corresponding RNA-seq (GSM7430297, GSM7430298, GSM7430255, GSM7430256) data generated by (Tomuro et al. 2024) was used for analysis with default settings unless specified otherwise. The datasets were downloaded using sratoolkit v2.11.0. Adapter trimming and quality control was done with fastp v0.23.2. Next, reads were mapped to human genome (emsembl v110, GRCh38.p14) with STAR v2.7.3a *–outSAMPtype BAM SortedByCoordinate*, bam files were indexed with samtools *index* v1.10 and coverage tracks were generated with deepTools v3.5.5 *bamCoverage*.

3.18. Protein isolation

After inhibitor treatments, cells were harvested using either Accutase (Sigma Aldrich, A6964-100ML) or a cell scraper (Starstedt, 83.3950). The cells were then centrifuged at 700g for 5

minutes at room temperature. The resulting pellet was washed with ice-cold Dulbecco's Phosphate Buffered Saline (DPBS, Sigma, D8662) and centrifuged again at 700g for 5 minutes at 4°C. The pellet was resuspended in Henikoff buffer (0.1% SDS, 3 mM $CaCl_2$, 20 mM Tris pH 8, 100 mM NaCl, 0.9% Triton X-100), supplemented with 1 µL/mL Sm nuclease, 1X cOmplete™ EDTA-free Protease Inhibitor Cocktail (Roche, 11836170001), and 1X PhosSTOP™ (Roche, 4906845001). The mixture was vortexed briefly and incubated on ice for 15 minutes. EDTA was then added to a final concentration of 20 mM. The samples were sonicated using a Bioruptor Pico (Diagenode) for 5 cycles of 30 seconds ON and 30 seconds OFF at 4°C. Following sonication, the samples were centrifuged at 12,000g for 10 minutes, and the supernatant was transferred to a fresh tube.

Protein concentrations were determined using a colorimetric Bradford assay (Panreac AppliChem ITW, A6932). A 20 mg/mL stock solution of recombinant albumin (New England BioLabs, B9200S) was diluted to 1 mg/mL using the protein isolation buffer. Serial dilutions were prepared by adding 0, 3, 6, 9, 12, and 15 µL of the 1 mg/mL albumin stock to cuvettes containing 1 mL of Bradford reagent. Additionally, 1 µL of each isolated protein sample was added to 1 mL of Bradford reagent in separate cuvettes. A standard curve was generated by measuring the absorbance of the albumin dilutions using a DS-11 FX+ Spectrophotometer/Fluorometer (DeNovix). The concentrations of the isolated protein samples were then determined based on the standard curve. Protein extracts were diluted to the required concentrations using nuclease-free water (Qiagen, 129115) and NuPAGE™ LDS Sample Buffer 4X (Novex, NP0007) supplemented with 50 mM DL-Dithiothreitol (DTT) (Sigma, D0632-25G). The final mixture was boiled at 70°C on a shaking heat block (Eppendorf® ThermoStat C), snap-frozen on dry ice, and stored at -20°C.

3.19. Immunoprecipitation for posttranslational modification analysis via Mass Spectrometry (IP-MS)

After 4 hours 100 ug/mL cycloheximide (CHX) (Sigma Aldrich, C7698-1G) treatment, cells were harvested using a cell scraper. The cells were then centrifuged at 700g for 5 minutes at room temperature. The resulting pellet was washed with ice-cold DPBS and centrifuged again at 700g for 5 minutes at 4°C. The pellet was resuspended in Henikoff buffer (0.1% SDS, 3 mM $CaCl_2$, 20 mM Tris pH 8.0, 100 mM NaCl, 0.9% Triton X-100), supplemented with 1 µL/mL Sm nuclease, 1X cOmplete™ EDTA-free Protease Inhibitor Cocktail (Roche, 11836170001), and 1X PhosSTOP™ (Roche, 4906845001). The mixture was vortexed briefly and incubated on ice for 15 minutes. The samples were sonicated using a Bioruptor Pico (Diagenode) for 2 cycles of 30 seconds ON and 30 seconds OFF at 4°C. Following sonication, the samples were centrifuged at 16,000g for 20 minutes, and the supernatant was transferred to a fresh tube.

After determining protein concentrations using a colorimetric Bradford assay, proteins were diluted in Henikoff buffer to a total concentration of 1 mg in a final volume of 500 uL. 5% of this protein sample was transferred to a clean tube as “input” sample.

After mixing on rotator for 10-15 min, 20 uL of Pierce™ Anti-HA Magnetic Beads (Thermo Fisher, 88836) for each 1 mg of protein extract was transferred to a clean tube. The tube was put on DynaMag™-2 Magnet (Thermo Fischer, 12321D) for 30 sec and the supernatant was removed. The beads were resuspended in 1 mL supplemented Henikoff buffer, then placed back on the magnetic rack. After removing the supernatant, beads were washed by resuspending in 1 mL of Henikoff buffer and placed on the magnetic rack again. After removing the supernatant, beads were resuspended in 25 uL Henikoff buffer per 1 mg of protein sample. The bead suspension (25 uL) was added to each 1 mg of protein sample. The protein-bead mixture was incubated on the wheel rotator in cold room for 1 h. After incubation, the protein-bead mixture was placed on the magnetic rack and washed three times with wash buffer (0.1% SDS, 20 mM Tris pH 8.0, 1 mM EDTA, 400 mM NaCl, 0.9% Triton-X 100) supplemented with 1X cOmplete™ EDTA-free Protease Inhibitor Cocktail, and 1X PhosSTOP™. After the final wash, the supernatant was removed as thoroughly as possible. Beads were resuspended in 50 uL of elution buffer (25 mM Tris-HCl pH 8.0, 1% [wt/vol] SDS) and boiled at 60°C for 15 min at 800 rpm on a shaking heat block (Eppendorf® ThermoStat C). The tubes were then centrifuged at full speed for 1 min at 4°C. The supernatant was carefully transferred to a new tube, ensuring no beads were carried over. The beads were resuspended in an additional 10 uL of elution buffer, boiled again, and centrifuged. The second supernatant was combined with the initial 50 uL elution, bringing the total volume to 60 uL. The beads were discarded, and the supernatant was snap-frozen and submitted to Proteomics Core Facility for Mass Spectrometry analysis. The analysis was carried out by Dr. Jiaxuan Chen from IMB Proteomics Core Facility.

3.20. Immunoprecipitation for interaction partner analysis via Mass Spectrometry (IP-MS)

The same protocol as in 3.14 was followed with minor modifications: Henikoff buffer and wash buffer were replaced with cell lysis buffer (250 mM NaCl, 50 mM HEPES pH 7.6, 0.1% IGEPAL, 10 mM MgCl2, 10% glycerol).

3.21. Co-immunoprecipitation (co-IP) for Western Blot for interaction partner analysis

The same protocol as in 3.14 was followed with minor modifications: Henikoff buffer and wash buffer were replaced with cell lysis buffer (100 mM NaCl, 50 mM HEPES pH 7.6, 0.1% IGEPAL,

10 mM $MgCl_2$, 10% glycerol). Beads were resuspended in 1X NuPAGE™ LDS Sample Buffer (Novex, NP0007) in water (without DTT) and boiled at 42°C for 10 min at 800 rpm.

1 M DL-Dithiothreitol (DTT) (Sigma, D0632-25G) was added to the 60 uL eluates, and NuPAGE™ LDS Sample Buffer 4X (Novex, NP0007) containing 0.4 M DTT was added to the input samples, adjusting the final DTT concentration to 100 mM in both cases. The input and eluates were then boiled at 70°C for 10 min at 800 rpm, snap-frozen and stored at -20°C until further use.

3.22. Western Blot

A 10% SDS-PAGE gel (for detecting exogenous SNRPB/N-2xHA-mNEON) or 12% SDS-PAGE gel (for detecting endogenous SNRPB/N) was prepared and stored at 4°C after polymerization until use. The gel was then placed into XCell *SureLock*™ Mini-Cell electrophoresis system (Invitrogen), and the protein samples were loaded to SDS-PAGE gel. The gel was run in 1X MOPS buffer (Fischer Scientific, BP308) at 180 Volt for 45 minutes to 1.5 hours, depending on the experimental needs. Meanwhile, a piece of Immobilon®-PSQ PVDF Membrane (0.2 µm, 8.5 cm x 10 m roll, Merck, ISEQ85R) was activated by submerging it to 100% methanol (Sigma Aldrich, 34860) for 1-2 minutes, then transferred to 1X transfer buffer (IMB Media Lab, T-20_L) containing 10% methanol, where it was kept until the SDS-PAGE run was complete.

After electrophoresis, proteins were transferred to the PVDF membrane using Mini Trans-Blot® Cell (Bio-Rad) apparatus at 300 mA for 1hour. Post-transfer, the gel was stained with InstantBlue Coomassie Protein Stain (Abcam, ab119211) until bands became visible, then washed with deionized water overnight.

The membrane was blocked with 5% nonfat dry milk (Cell Signaling Technology, 9999S) in PBST (1X PBS, 0.2% Tween® 20, Merck, P1379-1L) and incubated with the respective primary antibody, diluted in 5% milk-PBST, overnight at 4°C. Details of the primary antibody dilutions can be found in 2.8. Following three washes with PBST, the membrane was incubated with 1:10,000 dilution of secondary antibody at room temperature for 1 hour. After three additional PBST washes, the membranes were imaged using SuperSignal West Pico PLUS Chemiluminescent Substrate (Thermo Scientific, 34577), ChemiDoc™ Touch Gel Imaging System (Bio-Rad) and Image Lab Software Version 6.1.0.

3.23. Immunofluorescence stainings

Coverslips (Starstedt, 83.1840.002) were coated with Poly-L-Lysine (Sigma-Aldrich, P1274) according to the manufacturer' instructions. Cells were seeded onto cell culture dishes containing the coated coverslips. Following the required treatments, such as cycloheximide, samples were washed twice with DPBS (Gibco, 14040117) containing calcium and magnesium. The cells were then fixed with 4% paraformaldehyde (Thermo Scientific, 28906) in PBS without calcium and magnesium for 15 minutes at room temperature. After three washes with PBS, samples were stored at 4°C in PBS until staining.

For permeabilization, the samples were incubated in 0.25% Triton X in water for 3 minutes, followed by two PBS washes. Blocking was performed using 1% BSA (Pan Biotech, P06-1391500) in PBS for 30 minutes at room temperature. After two additional washes, samples were incubated overnight at 4°C with the respective primary antibody, diluted in 0.1% BSA in PBS.

Following three washes with PBS, samples incubated with the respective secondary antibody, diluted in 0.1% BSA in PBS, for 1 hour at room temperature. They were then washed twice with PBST (1X PBS, 0.2% Tween® 20, Merck, P1379-1L) and stained with DAPI (1:2000 dilution in PBS, Invitrogen, 10184322) for 10 minutes. After a brief wash with water, the coverslips were mounted using ProLong™ Diamond Antifade Mountant (Invitrogen, P36965).

3.24. Confocal fluorescence imaging

Fixed and immunostained cells were imaged using the Leica Stellaris 8 Falcon line scanning confocal microscope. The HC PL APO CS2 100x/1.4 NA oil-immersion objective from Leica was used to image an area of 116 x 116 µm with an image format of 1160 x 1160 pizels with bidirectional scanning. Confocal z-stacks were acquired with 40 z slices spanning a total thickness of 8 µm, resulting in a voxel size of 0.1 x 0.1 x 0.2 µm. DAPI, mNeonGreen and Alexa Fluor 555 were excited sequentially (line-switching) using 405 nm (diode), 488 nm (OPSL) and 550 nm (80 MHz pulsed White Light Laser) excitation lasers, respectively. Their fluorescence was detected using HyD hybrid detectors in photon-counting mode over wavelength ranges 415-485 nm, 500-538 nm and 560-725 nm, respectively, generating 3-channel digital images with a bit-depth of 8. 4-8 fields of view were chosen for imaging per sample, where the cells were growing in a monolayer.

3.25. FRAP (Fluorescence Recovery After Photobleaching)

FRAP measurements were performed on live cells in ibidi 8-well microwell slides using the Leica Stellaris 8 Falcon confocal microscope equipped with an Okolab incubation cage for maintaining the cells at 37 ^{o}C and 5% CO_2 during the measurements. For each FRAP measurement, a single focal plane 18.45 x 18.45 µm in size was imaged using the HC PL APO CS2 63x/1.4 NA oil-immersion objective from Leica with an imaging format of 256 x 256 pixels, resulting in a pixel size of 72 x 72 nm. Fluorescence of SNRPB-mNeonGreen or SNRPN-mNeonGreen was excited using the 80 MHz pulsed White Light Laser at 488 nm and the emission was detected in the wavelength range 500-550 nm using a HyD-S hybrid detector in photon counting mode. A 10-frame pre-bleach timelapse was recorded with a frame interval of 0.342s. Following this, a SNRPB-mNeonGreen or SNRPN-mNeonGreen focus was bleached using a high intensity of the same laser and a 50-frame post-bleach timelapse was recorded with a frame rate of 0.331s. The bleached SNRPB-mNeonGreen or SNRPN-mNeonGreen focus was them tracked over time and the mean intensity of mNeonGreen fluorescence inside the focus was used to obtain the FRAP recovery curve as described below.

Fiji v1.54p was used for all image visualization and analysis (Schindelin et al. 2012). All segmentations were performed on filtered 2D z-projections of the 3D images, where the filters and thresholding algorithms to be applied were determined empirically for each segmented object of interest and then applied consistently across samples.

3.26. Image processing and analysis

<u>Detection and counting of SNRPB/N and Coilin foci</u>

Maximum z-projections were used for the detection of Coilin and SNRPB/N-mNeonGreen foci. Max z-projections of the Coilin channel (gaussian filter, radius=2 pixels) and SNRPB/N-mNeonGreen channel (variance filter, radius=2 pixels followed by gaussian filter, radius=3 pixels) were thresholded using the Maximum Entropy algorithm to obtain binary masks of the foci in the respective channels (Kapur, Sahoo, and Wong 1985). The foci in each channel were counted, and these counts were normalized to the number of cells in the field of view. In control cells not expressing SNRPB/N-mNeonGreen (HEK), only Coilin foci were segmented and counted.

<u>Distance-based colocalization of SNRPB/N and Coilin foci</u>

The “Find maxima” function in Fiji was applied to the binary masks of Coilin and SNRPB/N-mNeonGreen foci with prominence 1 to detect the pixel closest to the center of each identified

focus in both channels, and a Euclidean Distance map (EDM) was calculated for the centers of the Coilin foci. The value on the EDM was then read out at the center of each SNRPB/N-mNeonGreen focus to obtain the distance to the center of the nearest Coilin focus. SNRPB/N-mNeonGreen foci categorized as their distance to a Coilin focus (0-200 nm, 200-1000 nm and >1000 nm).

Quantification of nuclear and cytoplasmic SNRPB/N-mNeonGreen

Sum z-projections of the 3D images were used for quantifying nuclear and cytoplasmic distribution of SNRPB/N signal in samples immunostained for SmB/B'/N. The sum x-projection of the DAPI channel (median filter, radius=2 pixels followed by gaussian filter, radius=5 pixels) was used to generate a nuclear mask using the Huang thresholding algorithm (L.-K. Huang and Wang 1995). The edges of the resulting thresholded nuclei were further eroded by two pixels to obtain an accurate binary mask of the nuclei. Similarly, the sum z-projection of the SNRPB/N-mNeonGreen channel (gaussian filter, radius=10 pixels) was used to obtain a binary mask of cells using the Triagle thresholding algorithm (Zack, Rogers, and Latt 1977) followed by the erosion of 5 pixels. For control cells not expressing SNRPB/N-mNeonGreen (HEK), autofluorescence of the cells could be picked up in this channel and used for segmenting the cells in the same way but using the iterative intermeans thresholding algorithm instead,

A binary mask of the cytoplasm was obtained by subtracting the nuclear mask from the cell mask, and the cell mask was inverted to obtain a mask for the background. The binary masks for nuclei, cytoplasm and background were then applied to the sum z-projections of SmB/B'/N and SNRPB/N-mNeonGreen channels to obtain mean intensity in each of these regions. The mean background intensity was then subtracted from both the mean intensities obtained for cytoplasmic and nuclear signal.

Analysis of FRAP data

Fluorescence recovery curves for the bleached SNRPB/N-mNeonGreen foci were obtained from the recorded timelapses using Fiji, where the TrackMate plugin (Tinevez et al. 2017) was used to track the bleached SNRPB/N-mNeonGreen focus over the timelapse using the Linear Assignment Problem tracker (Jaqaman et al. 2008). The mean intensity inside a circle of diameter 0.7 µm centered at the focus was estimated at each frame of the timelapse (I_{bleach} (t)).

To track mean intensity in the nucleus over time, a binary nuclear mask was generated from the first frame of the timelapse (gaussian filter, radius=2 pixels) using the Huang thresholding algorithm (L.-K. Huang and Wang 1995). The binary mask was then applied to each frame of

the timelapse to determine the mean intensity of SNRPB/N-mNeonGreen signal in the nucleus over time (I_{nuc} (t)).

Finally, a representative region in the background was chosen to determine the mean background intensity in each frame (I_{bg} (t)) and the mean intensities of the bleached spot and nucleus were corrected by subtracting the mean background intensity.

$$I_{bleach,\ bg\text{-}sub}(t) = I_{bleach}(t) - I_{bg}(t)$$

$$I_{nuc,\ bg\text{-}sub}(t) = I_{nuc}(t) - I_{bg}(t)$$

The intensity in the bleached spot was then double-normalized relative to the nuclear intensity and pre-bleached intensity as follows:

$$I_{bleach,\ norm}(t) = [I_{bleach,\ bg\text{-}sub}(t) - I_{bleach,\ bg\text{-}sub}(\text{pre-bleach})] \ / \ [\ I_{nuc,\ bg\text{-}sub}\ (t) - I_{nuc,\ bg\text{-}sub}\ (\text{pre-bleach})]$$

where I(pre-bleach) refers to the mean value from all pre-bleach timepoints.

3.27. Flow cytometry

Flp-In™ T-REx™ 293 and generated Snrpb/n cell lines were seeded to 6-well plate. Two wells of Flp-In™ T-REx™ 293 were left untreated for gating purpose. After the treatments, cells were harvested with accutase and centrifuged at 1000 rpm for 3 minutes at room temperature. The resulting pellet was washed with Dulbecco's Phosphate Buffered Saline and centrifuged again at 1000 rpm for 3 minutes at 4°C at room temperature. Then, the pellet was washed once with PBS without calcium and magnesium and centrifuged. The pellet was resuspended in 500 µL PBS without calcium and magnesium and transferred into round bottom polystyrene test tubes (Fisher Scientific, 10186360). Helix NP(TM) NIR (Biozol, BLD-425301) was then added to a final concentration of 5 nM.

Data were acquired on a BD LSRFortessa SORP (BD Biosciences) and analyzed using FlowJo (version10.10).

3.28. Enzymatic protein digestion for mass-spectrometry

All samples were processed using the SP3 approach (Hughes et al. 2019). Proteins were reduced in 5 mM DTT, alkylated in 15 mM Iodoacetamide (Sigma-Aldrich, I6125) in the dark and quenched in 5 mM DTT. Enzymatic protein digestion was perfomed using Trypsin (Sigma-Aldrich, T6567) or porcine pancreatic elastase (Promega, V189A) overnight at 37 °C. The resultant peptide solution was purified by solid phase extraction in C_{18} Stage Tips (Rappsilber, Ishihama, and Mann 2003).

3.29. Liquid chromatography tandem mass-spectrometry for PTMs

Peptides were analyzed using an Orbitrap Exploris 480 mass spectrometer (Thermo Fisher Scientific) coupled to an EASY-nLC 1200 UHPLC system (Thermo Fisher Scientific). Peptides were separated in an in-house packed 60-cm analytical column (inner diameter: 75 µm; ReproSil-Pur 120 C_{18}-AQ 1.9-µm silica particles, Dr. Maisch GmbH) by online reverse-phase chromatography through a 90-min gradient of 2.4-32% acetonitrile with 0.1% formic acid at a nanoflow rate of 250 nl/min. The eluted peptides were sprayed directly by electrospray ionization into the mass spectrometer. Mass spectrometry was conducted in data-dependent acquisition mode using a top15 method with one full scan (resolution: 60,000, scan range: 300-1650 m/z, target value: 3×10^6, maximum injection time: 28 ms) followed by 15 fragment scans via higher energy collision dissociation (HCD; normalized collision energy 30%; resolution: 15,000, target value: 1×10^5, maximum injection time: 40 ms, isolation window: 1.4 m/z). Only precursor ions of +2 to +6 charge state were selected for fragment scans. Additionally, precursor ions already isolated for fragmentation were dynamically excluded for 25 s.

3.30. Liquid chromatography tandem mass-spectrometry for interaction partners

Peptides were separated via an in-house packed 45-cm analytical column (inner diameter: 75 µm; ReproSil-Pur 120 C_{18}-AQ 1.9-µm silica particles, Dr. Maisch GmbH) on a Vanquish Neo UHPLC system (Thermo Fisher Scientific). Online reverse-phase chromatography was performed through a 70-min non-linear gradient of 1.6-32% acetonitrile with 0.1% formic acid at a nanoflow rate of 300 nl/min. The eluted peptides were sprayed directly by electrospray ionization into an Orbitrap Astral mass spectrometer (Thermo Fisher Scientific). Mass spectrometry was conducted in data-dependent acquisition mode using a top50 method with one full scan in the Orbitrap analyzer (scan range: 325 to 1,300 m/z; resolution: 120,000, target value: 3×10^6, maximum injection time: 25 ms) followed by 50 fragment scans in the Astral analyzer via higher energy collision dissociation (HCD; normalized collision energy: 26%, scan range: 150 to 2,000 m/z, target value: 1×10^4, maximum injection time: 10 ms, isolation window: 1.4 m/z). Precursor ions of unassigned, +1 or higher than +6 charge state were rejected. Additionally, precursor ions already isolated for fragmentation were dynamically excluded for 15 s.

3.31. Mass-spectrometry data analysis

Mass spectrometry raw data were processed by MaxQuant software (version 2.1.3.0) (Cox and Mann 2008) using its built-in Andromeda search engine (Cox et al. 2011). MS/MS spectra were searched against a target-decoy database containing the forward and reverse protein sequences of UniProt *H. sapien* reference proteome (release 2022_03; 101,732 entries),

mCherry, HA::mNEON::SNRPB, HA::mNEON::SNRPN and a default list of common contaminants. Carbamidomethylation of cysteine was considered a fixed modification. The variable modification search included methionine oxidation, protein N-terminal acetylation, mono- and di-methylation on KR residues, and hydroxyproline. A maximum of 2 missed cleavages were allowed. The “second peptides” option was switched on. Minimum peptide length was set to be 7 amino acids. False discovery rate (FDR) was set to 1% at both peptide and protein levels.

For samples digested using trypsin, the trypsin/P specificity was chosen. For samples digested using elastase, the search was performed in two steps. Semi-specific cleavage at AGILSTV residues (Rietschel et al. 2009) was assigned initially without considering the variable modifications of mono-, di-methylation and hydroxyproline. To limit the search space of multiple variable modifications in a semi-specific setting, the detected proteins from the first search served as a reduced sequence database for a second search in which mono-, di-methylation on KR residues and hydroxyproline were considered.

To quantify the detected PTMs, the intensities of peptide evidences associated with each detected PTM site were summed and then normalized according to the overall detected peptide intensities in each sample, assuming the overall peptide intensities were similar across the test conditions.

Protein quantification was performed using the MaxLFQ algorithm (Cox et al. 2014) skipping its default normalization option. Minimum LFQ ratio count was set to one. Both the unique and razor peptides were used for quantification. Differential expression analysis was performed in R statistical environment. Reverse hits, potential contaminants and “only identified by site” protein groups were first filtered out. Data normalization was performed on the log-transformed data using median-centering. Proteins were further filtered to retain only those detected in at least 3 out of the 4 replicates in either group of each comparison. Following imputation of the missing LFQ intensity values, a linear model was fitted using the limma package in R (Phipson et al. 2016) to assess the difference between the two groups for each protein, with adjustment for multiple testing using the Benjamini-Hochberg approach (Benjamini and Hochberg 1995). The log2 fold change and the significance of the difference were displayed on a volcano plot. Only proteins with a minimum log2 fold change of 1 and an FDR-adjusted p value (q value) lower than 0.05 were considered as being differentially regulated.

3.32. Mice handling and intracerebroventricular cycloheximide injections

Wild type mice in a C57BL/6J background were kept by our collaborator Dr. Ana Villalba Requena (Hippenmeyer Group, Klosterneuburg) according to the protocols approved by Institutional Animal Care and Use Committee, Institutional Ethics Committee and the Preclinical Core Facility at Institute of Science and Technology of Austria (ISTA). Experimental protocols were performed under the approval of the Austrian Federal Ministry of Science and Research in accordance with the Austrian and European Union animal laws (license number: BMWFW-66.018/0015-WF/V/3b/2017).

All mice used showed pathogen free status according to the Federation of European Laboratory Animal Science Associations (FELASA) recommendations. Animals were maintained and bred in the Animal Facilities of the Institute of Science and Technology of Austria (ISTA). Animals were kept on a 12:12 hours light:dark cycle, room temperature of 21 ± 1°C and relative humidity of 40% to 55%, in accordance to European Union regulations. Food (V1126, Ssniff Spezialiteaten GmbH, Soest, Germany) and tap water available ad libitum.

Pups of 7 days postnatal (P7) were deeply anesthetized with Vetflurane (induced at 3% and maintain at 1-2%). After fixing the pup to the stereotaxic, the head was cleaned with 70% EtOH, Xylocain Gel 2% was applied and the skull was exposed by a minimal cut along the anterior-posterior axis and other perpendicularly to it at the level of lambda. The injected location was established by the coordinates: -0.3 to -0.5mm from Bregma in the anterior-posterior axis, ±1.00 to 1.5mm in the medial-lateral axis and 2.0 to 2.5mm in the ventral-lateral axis. For the injections, pulled glass micropipettes were used together with a Nanoject III (Drummond Scientific Company). 500nL with a 200nL/s rate for 10 cycles was injected (a total of 5µL) per hemisphere. Cycloheximide (CHX, Sigma, REF C7698-1G) at 4µg/µL concentration in NaCl 0.9% was administered in the treatment condition, while controls received a solution of NaCl 0.9%. CHX working solution was prepared fresh the day of the injections. Both conditions included 0.02% Fast Green (Sigma, REF F7252-5G). After injecting both hemispheres, tissue adhesive (SURGIBOND, REF ZG2) was applied in the edges of the wound. The pup was maintained over a warm pad during the whole procedure and until it woke up. Pups were placed back with the mother for 5 hours. Then, the pups were sacrificed by cervical dislocation and immediately processed. The brain was extracted, the cortex dissected and divided sagittally in three pieces. Each part was frozen by immersion in liquid nitrogen.

In order to assure that equal number of experimental cohorts according to sex was taking into account, male and female sex was assigned based on Y-chromosome genotyping at P4.

3.33. Statistics and reproducibility

All plots and statistical analyses were generated in RStudio 2024.04.1+748 (2024.04.1+748) with R version 4.4.0 (2024-04-24). Boxplots were generated in ggplot2, with the following parameters: lower whisker = smallest observation greater than or equal to lower hinge - 1.5 * IQR; lower = lower hinge, 25 % quantile; notchlower = lower edge of notch = median – 1.58 * IQR / sqrt(n); middle = median, 50 % quantile; notchupper = upper edge of notch = median + 1.58 * IQR/sqrt(n); upper = upper hinge, 75 % quantile; ymax = upper whisker = largest observation less than or equal to upper hinge + 1.5 IQR. Bar plots represent the mean ± s.e.m with overlaid data points representing independent experiments or replicates. Results were considered significant at a FDR or *p*-value below 0.05. Unless otherwise specified, statistical tests were two sided. Immunofluorescence was independently repeated at least four times with similar results. The FRAP experiments were independently performed and quantified twice. Western blots and co-immunoprecipitation experiments were independently replicated at least twice with similar results. Semi-quantitative RT-PCRs were performed once. Genotyping PCRs for positive CRISPR clones were repeated twice, followed by validation with complementary experimental approaches (qPCR and Western blot). Additional information and test results of statistical analysis are provided in the methods or figure legends.

4. Results

Manuscript in preparation:

Paralogue-specific Modification of SNRPN Couples Metabolic Subfunctionalization

Feyza Polat[1],

[1] Institute of Molecular Biology (IMB), Mainz, Germany

[2] Institute of Science and Technology Austria, Klosterneuburg, Austria

[3] Universität Bern, Bern, Switzerland

[4] University Medical Center, Mainz, Germany

Author Contributions:

I planned and executed all wet lab experiments, interpreted and analyzed the data and wrote the manuscript together with my supervisor CIKV.

The contributions of the other authors were as follows:

XX: Maintenance of human induced stem cells (hiPSCs), the induction of hiPSCs to neurons with treatments and collection of pellets, and data collection on the composition of different media used for hiPSCs and neurons.

XXX: Performed intracerebroventricular injections of ethanol and cycloheximide in neonatal mice, and conducted cortical dissections.

XX: Ribosome profiling data processing.

XXXX: Data collection on the composition of media used for HEKs.

XXX: Imaging and data analysis of confocal microscopy (data presented in the manuscript figures; replication and quantification of my own previous findings), Fluorescence Recovery After Photobleaching (FRAP) experiments.

XX: Data processing for RNA-seq.

XX: Data analysis strategy and statistics for FRAP.

XX: Mass-spectrometry and data processing.

XX: Provided samples and initiated data sharing on iNeuron differentiation and NMDi treatment.

XXXX: Bioinformatic analysis / interpretation of interaction partners (mass spectrometry) and RNA-seq.

In addition, XXX, XX, and XX jointly supervised aspects of the project and the involved scientists, interpreted data and provided resources/fundings.

4.1. SNPRN stabilizes transcripts involved in metabolic functions

SNRPB and *SNRPN* exhibit mutually exclusive expressions across tissues. Due to vast differences in trans-acting factors (e.g., gene expression profiles, splicing factors), it is difficult to disentangle intrinsic versus extrinsic effects of these two splicing paralogues in an organismal context. To address this, we generated HEK cells using the Flp-In™ T-REx™ 293 system, enabling the inducible expression of either SNRPB or SNRPN from a single-copy transgene tagged with a C-terminal HA and mNeonGreen epitope (Figure 4. 1. a, b). To ensure that this work focused exclusively on SNRPB and SNRPN, we used mouse tissues for cloning, as they lack the SNRPB' isoform. Specifically, we cloned *Snrpb* from embryonic mouse brain cDNA, and *Snrpn* from adult mouse brain cDNA. We confirmed the successful generation of stable cell lines by hygromycin resistance selection and β-galactosidase activity loss, indicative of proper construct integration.

HEK cells endogenously express *SNRPB*, but not *SNRPN* (Figure 4. 1. b). Upon induction of the transgenes, we found that the SNRPB/N proteins could not be expressed above the endogenous levels, even at high doxycycline concentrations, indicating tight dosage control (Figure 4. 1. c). Since *SNRPB* is a common essential gene (DepMap 2024), we used CRISPR/Cas9 to delete the endogenous *SNRPB* gene only after transgene insertion, whereupon the cells relied exclusively on the transgenic copy of either *SNRPB* or *SNRPN* (hereinafter referred to as SNRPB or SNRPN-cells, respectively). Immunoblotting confirmed successful deletion of endogenous SNRPB and expression of the transgenes (Figure 4. 1. d). In immunostainings, *Snrpb* and *Snrpn* transgenes localized to the nucleus and, as expected (Thompson et al. 2018), formed foci that co-localized with Cajal bodies, as indicated by Coilin staining (Figure 4. 1. e).

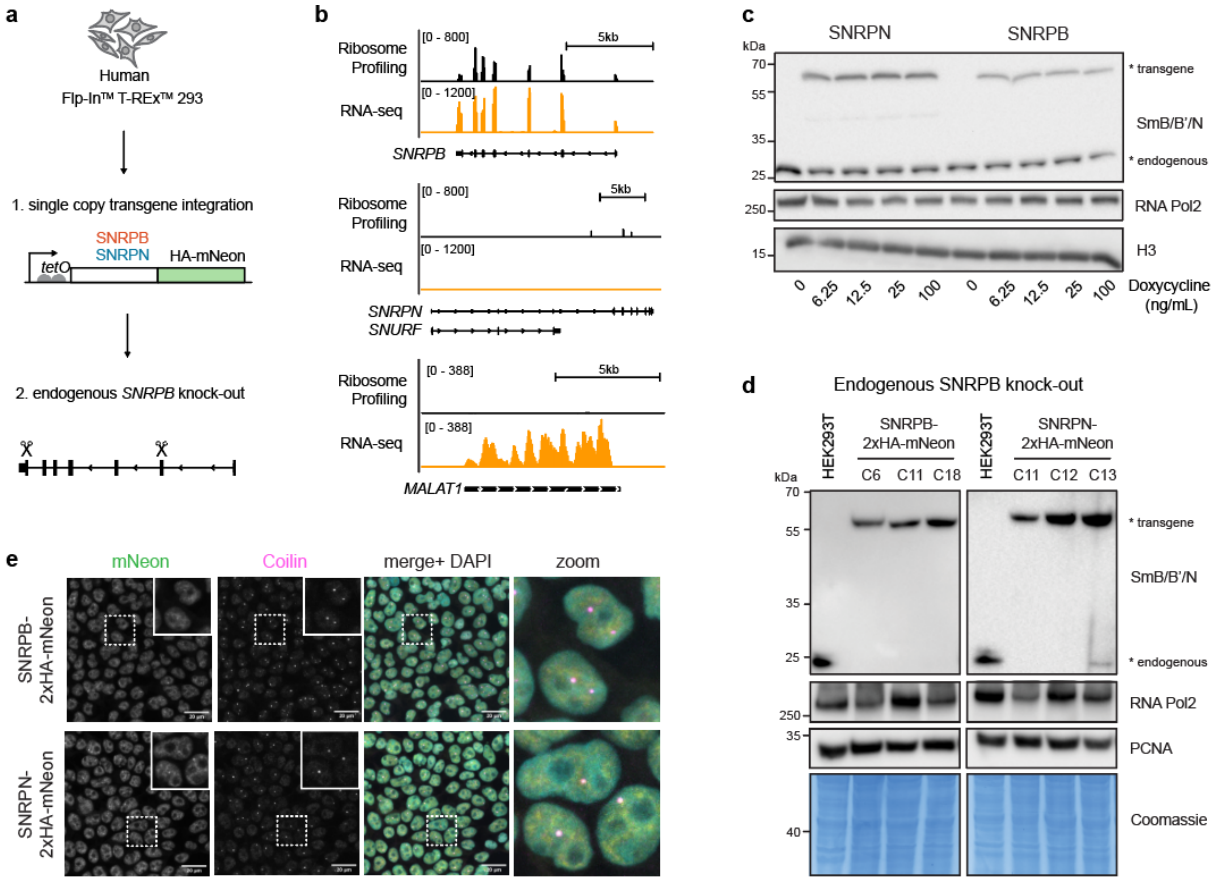

Figure 4. 1. Generation and validation of HEK293T cell lines stably expressing either mouse *Snrpb* or *Snrpn* transgenes under identical genetic background. (a) Schematic representation of the cell line development strategy: single-copy, doxycycline-inducible HA-mNeon-tagged *Snrpb* or *Snrpn* transgenes were integrated using the Flp-In™ T-REx™ 293 system, followed by CRISPR/Cas9-mediated knockout of the endogenous *SNRPB* gene. **(b)** Ribosome profiling and RNA-seq traces showing endogenous expression of *SNRPB*, but not *SNRPN*, in HEK293T cells. Tracks show ribosome occupancy (black) and transcript abundance (orange) across *SNRPB*, *SNRPN/SNURF*, and *MALAT1* loci. **(c)** Western blot showing doxycycline-inducible expression of HA-mNeon-tagged Snrpb or Snrpn transgenes in the presence of endogenous *SNRPB*. Transgene-derived and endogenous SNRPB proteins are distinguished by molecular weight. RNA Pol2 and histone H3 serve as loading controls. **(d)** Western blot confirming knockout of endogenous SNRPB in cell lines stably expressing Snrpb or Snrpn transgenes. Multiple independent clones were validated. RNA Pol2, PCNA, and Coomassie staining serve as loading controls. **(e)** Representative fluorescence microscopy pictures showing nuclear localization of the HA-mNeon-tagged SNRPB and SNRPN transgenes (mNeon-green), with co-localization to Cajal bodies (Coilin-magenta). DAPI (cyan) stains nuclei. The areas marked with a dashed square are magnified in the “zoom” panel. Data obtained from two independent replicates. Scale bars: 20 μM.

To investigate their functional differences, we performed stranded mRNA sequencing on two independent SNRPB-expressing clones and four independent SNRPN-expressing clones, alongside parental HEK cells. Clustering analysis revealed that SNRPB-expressing cells were largely similar to the parental HEK cells (Figure 4. 2. a). In contrast, SNRPN-expressing clones exhibited a markedly different transcriptomic profile and clustered separately (Figure 4. 2. a). Differential expression analysis using DESeq2 identified 2,103 genes with higher expression in SNRPN-expressing cells and 2,670 genes with higher expression in SNRPB-expressing cells (Figure 4. 2. b). Genes stabilized by either paralogue tended to have more transcript isoforms than expected (Figure 4. 2. c), but gene length and exon numbers were not different from other cellular transcripts (Figure 4. 2. d). We performed splicing analysis using rMATS (Shihao Shen et al. 2014), which identified several thousand splicing events, but a majority of them was not differentially regulated between SNRPB- and SNRPN-expressing cells (Figure 4. 2. e). Manual inspection of significant splicing changes revealed that most were artifacts arising from overall expression level differences of transcripts between the SNRPB and SNRPN cells. An independent analysis using VAST-Tools (Gohr et al. 2022) identified only a single significant alternative splicing event, which after manual inspection appeared false positive (data not shown). Lastly, we analyzed intron retention events using IRFinder (Lorenzi et al. 2021), which identified 14 differential intron retention events affecting 12 genes (Supplementary Table 8. 1). Manual inspection identified the majority as false positives, but *ITPKC* (Inositol-Trisphosphate 3-Kinase C) was a notable case with prominent intron retention in SNRPB, but not SNRPN expressing cells (Figure 4. 2. f).

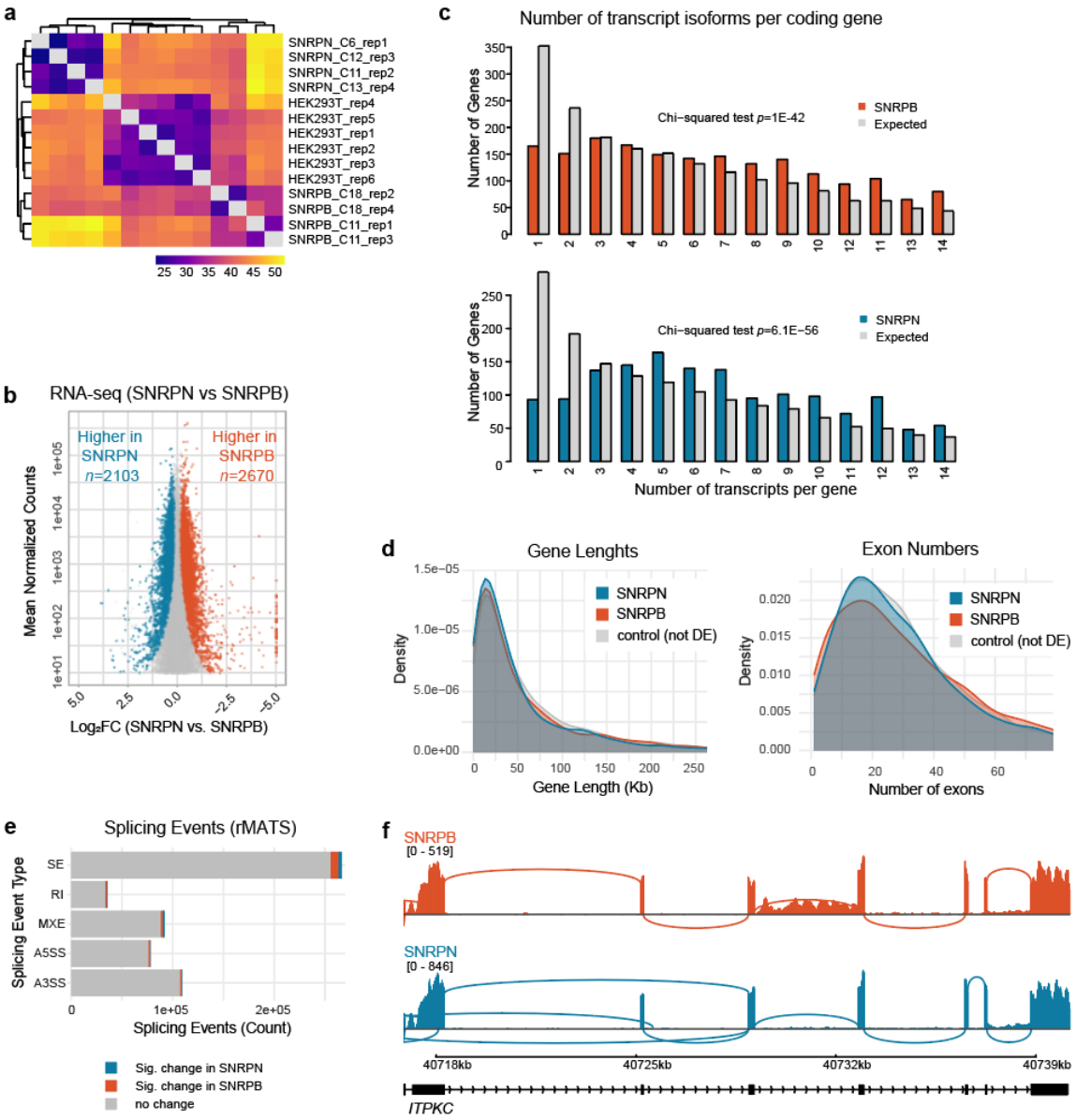

Figure 4. 2. *Snrpn* expression induces widespread transcriptomic changes compared to *Snrpb*, without major differences in alternative splicing. (a) Sample-to-sample distance matrix based on regularized log-transformed RNA-sequencing data from parental HEK cells, SNRPB-expressing clones, and SNRPN-expressing clones. **(b)** MA plot showing differentially expressed genes between SNRPB-expressing (orange) and SNRPN-expressing (blue) cells. **(c)** Distribution of transcript isoform numbers per coding gene for genes significantly upregulated in SNRPB and SNRPN cells. Observed versus expected distributions are compared based on the background transcriptome. Statistical significance was determined using a Chi-squared test. **(d)** Density plots comparing gene lengths (left) and exon counts (right) among genes stabilized in SNRPB and SNRPN cells, relative to a background set of non-differentially expressed (non-DE) genes. **(e)** Splicing event counts identified by rMATS across five splicing types: SE (skipped exon), RI (retained intron), MXE (mutually exclusive exon), A5SS (alternative 5' splice site), and A3SS (alternative 3' splice site). **(f)** Genome browser tracks showing the only significantly retained intron (RI) event detected between Snrpb- and Snrpn-expressing cells.

To further explore the characteristics of genes differentially stabilized by SNRPB/N, we conducted KEGG pathway analysis (Figure 4. 3. a, b). SNRPB-stabilized genes were enriched in pathways associated with cellular surface functions, including "ECM−receptor interaction," "Sphingolipid signaling pathway," "Endocytosis," and "Adherens junction." Interestingly, SNRPN-stabilized genes had very different gene functions and were involved in metabolic processes, with enriched KEGG-pathways like "Cysteine and methionine metabolism," "Pyruvate metabolism," and "Glycolysis/Gluconeogenesis". Examples for genes stabilized in SNRPN-cells are prominent metabolic enzymes such as PGM1 (phosphoglucomutase 1), PGK1 (phosphoglycerate kinase 1), PK (pyruvate kinase). In addition, 17 of the 42 large and 6 of the 35 small mito-ribosomal subunits encoded in the nucleus and multiple enzymes of the glycolysis pathway (Figure 4. 4) were more stable in SNRPN cells. More generally, genes stabilized by SNRPN had significantly higher expression levels, consistent with metabolic functions encoded by these genes (Figure 4. 3. c). These distinct transcriptomes were also reflecting on cellular parameters (Figure 4. 3. d), as SNRPN-expressing cells proliferated significantly faster than the SNRPB-expressing cells (p=0.0454). Taken together, these data suggest that SNRPB/N do not predominantly impact alternative splicing events, which is consistent with the fact that neuronal-specific alternative splicing proceeds normally in mice lacking *Snrpn* expression (Huntriss et al. 1994). Rather these paralogues appear to fine-tune the efficiency of the splicing process *per se*, which is expected to affect highly expressed transcripts involved in metabolic processes more strongly. Their rapid processing demands make them particularly susceptible to a potentially rate-limiting step in the splicing machinery.

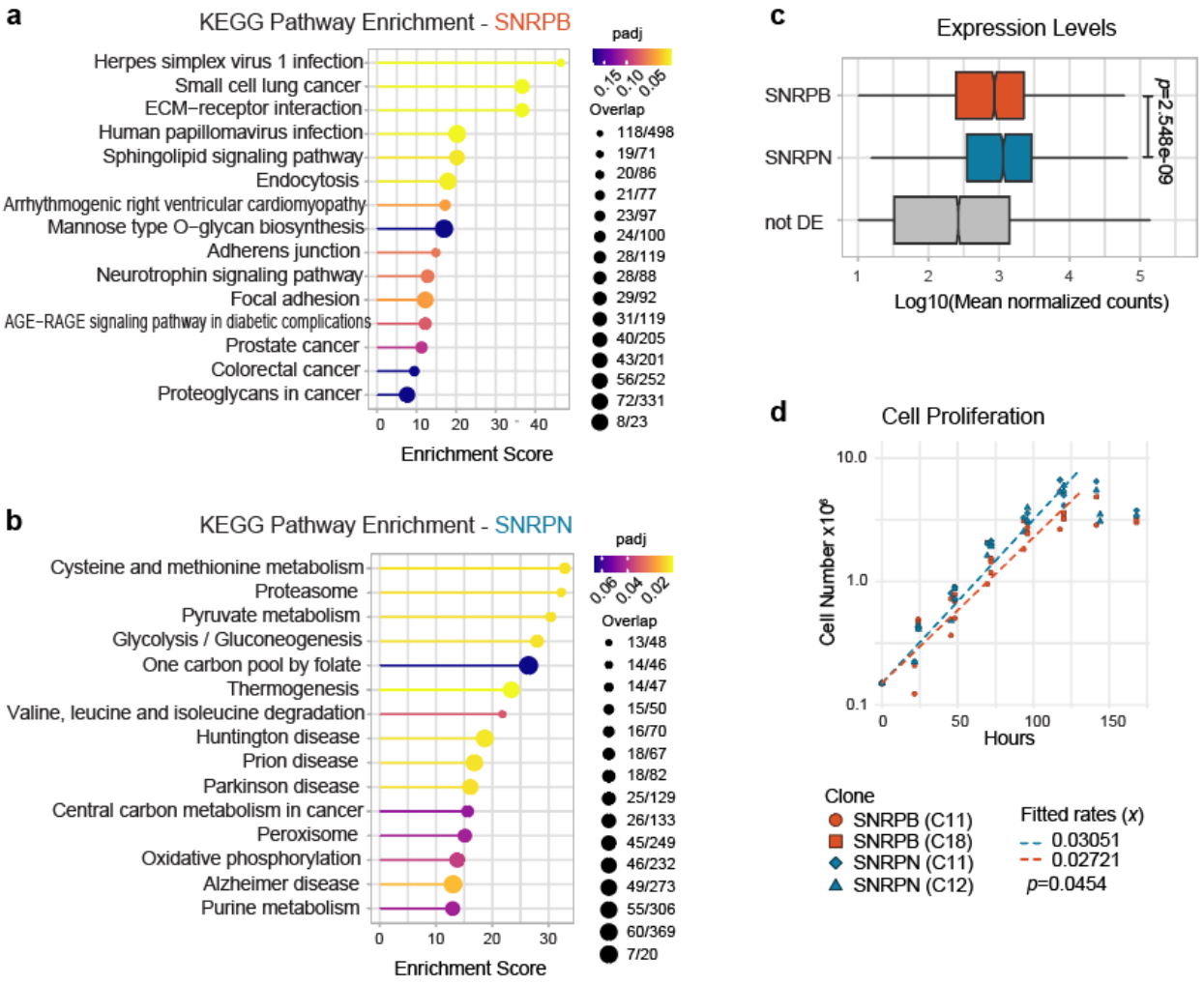

Figure 4. 3. SNRPN expression promotes a metabolic gene expression program and enhances cellular proliferation compared to SNRPB. (a, b) KEGG pathway enrichment analysis of genes significantly upregulated in SNRPB- (a) and SNRPN-expressing cells (b). Enrichment scores are plotted on the x-axis, with dot size corresponding to gene overlap and color representing adjusted p-values (padj). **(c)** Expression levels of genes significantly upregulated in SNRPB, SNRPN, or not differentially expressed, shown as log10-transformed mean normalized counts. Statistical significance assessed using Wilcoxon rank sum exact test. **(d)** Cell proliferation curves for SNRPB- and SNRPN-expressing clones. Cell counts were measured at multiple time points. *p*-values were calculated by using a linear regression model with an interaction term between time and cell line: log(cell number) ~ Hour * Cell Line. *p*-values correspond to the interaction term from the model coefficients, testing for differences in growth rates.

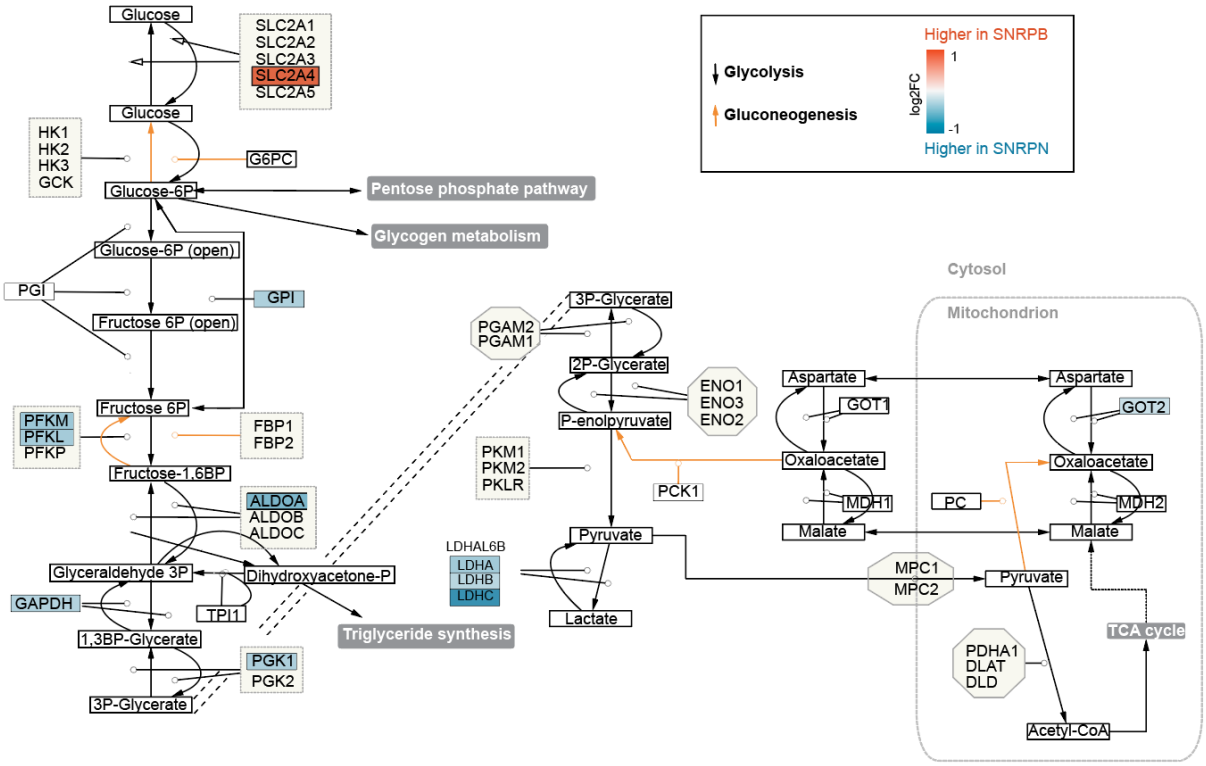

Figure 4. 4. SNRPN expression preferentially stabilizes transcripts encoding glycolytic and gluconeogenic enzymes. Metabolic pathway map highlighting glycolysis and gluconeogenesis genes with significantly higher expression in SNRPB- or SNRPN-expressing cells, based on DESeq2 differential expression analysis. Genes are color-coded by $\log_2$ fold change: red indicates higher expression in SNRPB-expressing cells, and blue indicates SNRPN-expressing cells. Orange arrows indicate gluconeogenic reactions. Black arrows indicate glycolytic flux.

4.2. SNRPB and SNRPN paralogues differ in their arginine methylation states

The finding that SNRPB and SNRPN stabilize distinct transcripts is particularly striking given that these paralogs encode nearly identical proteins, with their few amino acid differences present in the poorly characterized C-terminal Proline-rich region (Figure 1. 4). We profiled the interaction partners of SNRPB (Figure 4. 5. a) and SNRPN (Figure 4. 5. b) using the C-terminal HA-tag, comparing them to an untagged control cell line (Figure 4. 5. c). As expected, both paralogues interacted reliably with the Sm/SMN complex and key snRNP components (Figure 4. 5. a, b, d). Both the high- and low-confidence interactors showed a high overlap between SNRPB and SNRPN (Figure 4. 5. e), and were similar with regards to the strength of their interactions, which remained largely comparable across both interactomes (Figure 4. 5. f, g, Pearson R^2=0.79). However, a few notable exceptions were observed, among some were

uniquely enriched, and others showed a significantly stronger enrichment in one paralogue compared to the other (Figure 4. 5. f, g). For the SNRPB cells, these included the RNA editing enzyme APOBEC3B, the DNA topoisomerase 3-alpha (TOP3A), or the Lysine Methyltransferase 2D (KMT2D). For SNRPN, we found several methylosome components more strongly enriched (Arginine methyltransferase PRMT5; the substrate adaptors CLNS1A, also known as pICln, RIOK1, and WDR77). The methylosome complex participates in the regulation of snRNP biogenesis through Arginine methylation and through this mechanism controls interactions with other splicing factors (e.g. the SMN protein) as well as subnuclear localization (Friesen et al. 2001; Pu et al. 1999). Arginine methylation is also important for the release of RNAs from chromatin ensuring a productive splicing process (DeAngelo et al. 2024; Maron et al. 2022). Sm proteins like SNRPB are among the most prominent targets of multiple arginine methyltransferases (W.-J. Li et al. 2021), but a role and differential regulation in the context of SNRPN and/or different tissues has not been explored yet. Given the differences in methylosome association, we conducted a comprehensive analysis of posttranslational modifications (PTMs) through high-stringency immunoprecipitation of SNRPB/N, followed by quantitative mass spectrometry. To achieve high sequence coverage, we used both trypsin and elastase digestion strategies. While phosphorylation and citrullination sites could not be detected, we identified several lysine mono- and dimethylation sites, as well as proline hydroxylation sites, which exhibited similar patterns in both paralogues. Additionally, we found multiple arginine mono- and dimethylation sites, with several positions methylated in SNRPN but unmethylated in SNRPB (Figure 4. 6). While the Arg-Gly-rich region (positions 90-160) showed overall similarity in methylation status, differences emerged in the Pro-rich region (position 160 onwards). Notably, monomethylation on Arg196 and Arg209, as well as dimethylation of Arg209, was detected exclusively in SNRPN, along with methylation of Arg residues that are unique to SNRPN (Arg236, Arg239). Together this data shows that SNRPN displays stronger association with the methylosome complex, reflected in a distinctive Arg-methylation pattern.

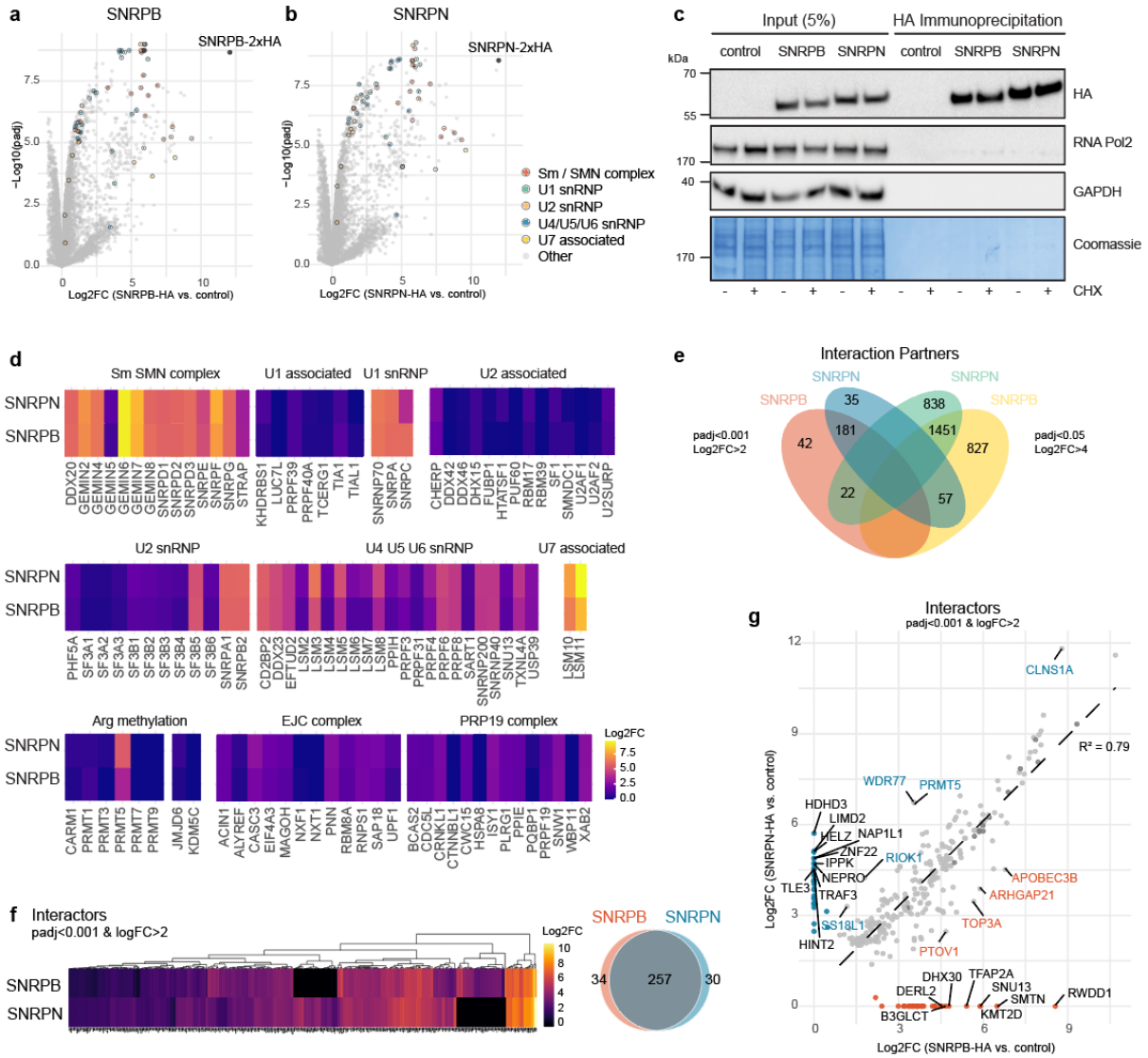

Figure 4. 5. SNRPB and SNRPN interactomes show shared and distinct protein interactions, with differential association to the methylosome complex. (a, b) Volcano plots of HA immunoprecipitations (IP)-mass spectrometry comparing HA-tagged SNRPB (a) and SNRPN (b) to untagged control cells. Statistically significant interactors are highlighted and colored by snRNP complex associations. **(c)** Western blot validation of HA pulldowns in untagged control cells, and cells expressing HA-tagged SNRPB or SNRPN, with and without cycloheximide (CHX) treatment (100 µg/mL, 4 hours). RNA POL2, GAPDH, and Coomassie staining serve as loading controls. **(d)** Heatmaps of selected interaction partners from distinct snRNP and RNA-processing complexes, grouped by function. Log_2 fold changes (HA-IP vs. control IP) are shown for both SNRPB and SNRPN. **(e)** Venn diagram showing overlap of interactors for SNRPB and SNRPN at two stringency thresholds: high confidence (padj < 0.001, $log_2FC > 2$) and medium confidence (padj < 0.05, $log_2FC > 1$). **(f)** Hierarchical clustering of high-confidence interactors (padj < 0.001, $log_2FC > 2$) for SNRPB and SNRPN (left), and venn diagram showing the number of uniquely and commonly enriched proteins at this high confidence threshold. **(g)** Scatter plot comparing enrichment of shared interactors in SNRPB and SNRPN IPs. Dashed line indicates equal enrichment. Selected proteins with strong paralog-specific enrichment are labeled. Pearson correlation coefficient $R^2 = 0.79$.

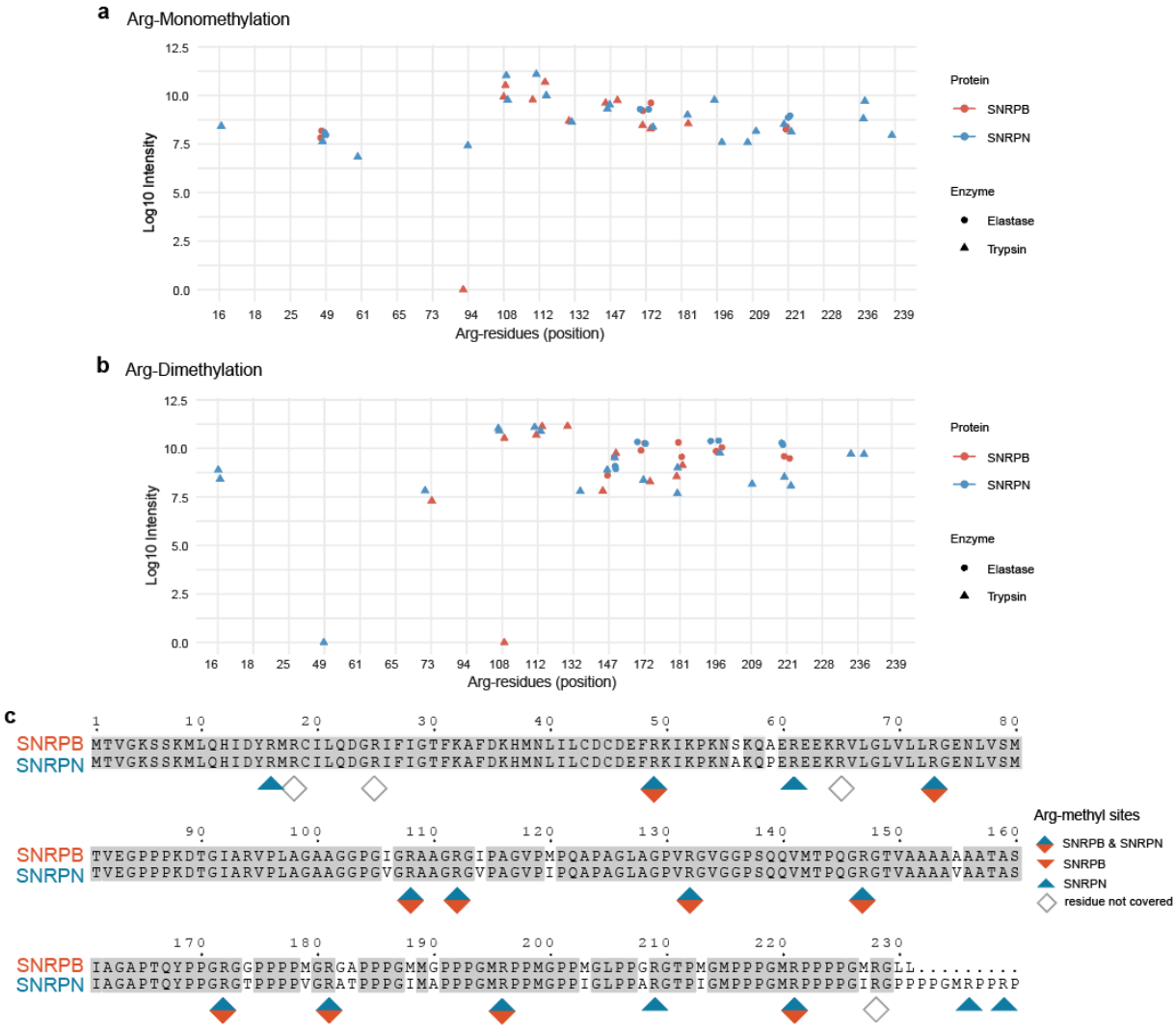

Figure 4. 6. SNRPN displays a distinct arginine methylation pattern compared to SNRPB, with differences localized to the C-terminal proline-rich region. (a, b) Quantification of arginine monomethylation (a) and arginine dimethylation (b) intensities for each detected methylated Arginine (Arg) residue in SNRPB and SNRPN, as identified by mass spectrometry. Data are shown separately for samples digested with elastase (circles) and trypsin (triangles). **(c)** Linear alignment of SNRPB and SNRPN protein sequences with annotated methylation sites. Colored diamonds indicate methylation detected in both paralogues, exclusively in SNRPB (orange), or exclusively in SNRPN (blue). Open diamonds mark arginine residues not covered by mass spectrometry.

4.3. Translation-dependent Arginine methylation distinguishes SNRPN from its paralogue SNRPB

Next, we investigated whether the PTM-state in the Pro-rich region is influenced by specific environmental conditions and contexts. SNRPB is one of the prominent auto-antigens in Systemic Lupus Erythematosus (SLE) (van Beers and Schreurs 2022), and the anti-Smith Antigen Antibody Y12, originally isolated from a patient with SLE, requires dimethylarginine modification for recognition. Yet, Y12 was unsuitable for our purposes because it binds a modified epitope (amino acids 100–120, Arg-Gly-rich domain), which lies upstream of our region of interest (Gao et al. 2019; Brahms et al. 2000). By western blot, we however identified the monoclonal antibody 12F5 (referred to as “SmB/B’/N”), which successfully recognized the C-terminal fragments 190-231 (SNRPB) and 190-240 (SNRPN), but failed to detect a truncated SNRPB (1-190) protein (Figure 4. 7. a, b). To monitor overall protein levels throughout the study, we used an HA-epitope antibody in SNRPB/N cells, confirming equal protein expression across samples. Additionally, we employed an antibody raised against SNRPB protein purified from E. coli, which lacks major eukaryotic PTMs, such as arginine methylation or phosphorylation (referred to as “SNRPB”).

In SNRPB/N cells, 12F5 detected both proteins with largely equal intensity, with a tendency for stronger intensity in SNRPB compared to SNRPN (Figure 4. 7. c). However, following treatment with two well-established arginine methyltransferase inhibitors (Cheng et al. 2011; W.-J. Li et al. 2021), HA-tag intensities remained unchanged, while SNRPN, but to a much less extent SNRPB intensity, decreased (Figure 4. 7. c). Conversely, in a point mutant, where all 6 Arg-residues in the Pro-rich region are mutated to Lysine (R6K, Figure 4. 7. d), the opposite effect was observed and the intensity increased substantially (Figure 4. 7. e). This indicates that 12F5 is sensitive to an epitope change unique to SNRPN, which requires Arg-methylation in the Pro-rich region. Although we could not identify the exact nature of this epitope change, we were intrigued by SNRPN’s distinct susceptibility to Arg-methylation inhibition and henceforth, used 12F5 as an experimental tool to screen multiple compounds and conditions for differential PTM states of SNRPB/N.

We observed a strong reduction in SNRPN detection by 12F5 following treatment with Actinomycin D (transcription inhibitor), Cycloheximide (CHX) and Puromycin (translation inhibitors) (Figure 4. 7. f, g). Moderate sensitivity of SNRPN was also detected after heat shock and INK128 treatment, which inhibits mTOR kinase (Huiyuan Zhang et al. 2015) (Figure 4. 7. g, h). However, no differences were observed after splicing inhibition with pladienolide B (PlaB) (Figure 4. 7. i, j). Instead, SNRPB and SNRPN proteins appeared to be stabilized by PlaB, as indicated by a concordant increase in HA and 12F5 signal (Figure 4. 7. i). Treatments with Camptothecin (DNA Topoisomerase I inhibitor), STM2457 (m6A-RNA methylation inhibitor),

Bortezomib (proteasome inhibitor), and Deferoxamine (iron chelator) did not produce any effects (Figure 4. 7. g), suggesting that the observed differences are specific and not due to general cellular stress or perturbations in transcriptome/proteome homeostasis.

Besides key roles in protein synthesis and nutrient sensing via mTOR signaling, mRNA translation is a requirement for nonsense mediated RNA decay (NMD). Following an initial translation event, NMD recognizes and degrades transcripts with premature stop codons, which are typical by-products of splicing errors. However, SNPRB/N remained unaffected after NMD inhibition with the SMG1 inhibitor 11e (Nasif et al. 2023) (Figure 4. 8. a), although multiple NMD targets were stabilized demonstrating successful inhibitor treatment (Figure 4. 8. b). In addition, the effects of CHX were not suppressed by PlaB, indicating that productive splicing is not a prerequisite for CHX-induced PTM change (Figure 4. 8. c). We validated that overall protein stability differences after CHX treatment are not a confounding factor (1) using the polyclonal SNRPB antibody raised in *E.coli* along with (2) intensity quantification of the protein levels with the C-terminal mNeon-tag by flow cytometry (Figure 4. 8. d, e). A very mild and equal decrease in overall SNRPB/N protein levels was detected after CHX. To exclude artifacts due to the sample preparation method, we repeated the experiment with an independent protein extraction method based on trichloracetic acid (TCA), which - as the canonical protocol - uncovered the epitope change with 12F5 (Figure 4. 8. f). Because fluorescent tags can influence protein function (D/"orner et al. 2024), we also validated our findings using two alternative constructs: (1) cell lines expressing a short C-terminal 2XHA-V5 tag, and (2) a construct with the mNEON tag positioned at the N-terminus. Both approaches validated the aforementioned results – CHX sensitivity was observed for SNRPN, but not for SNRPB transgenes (data not shown).

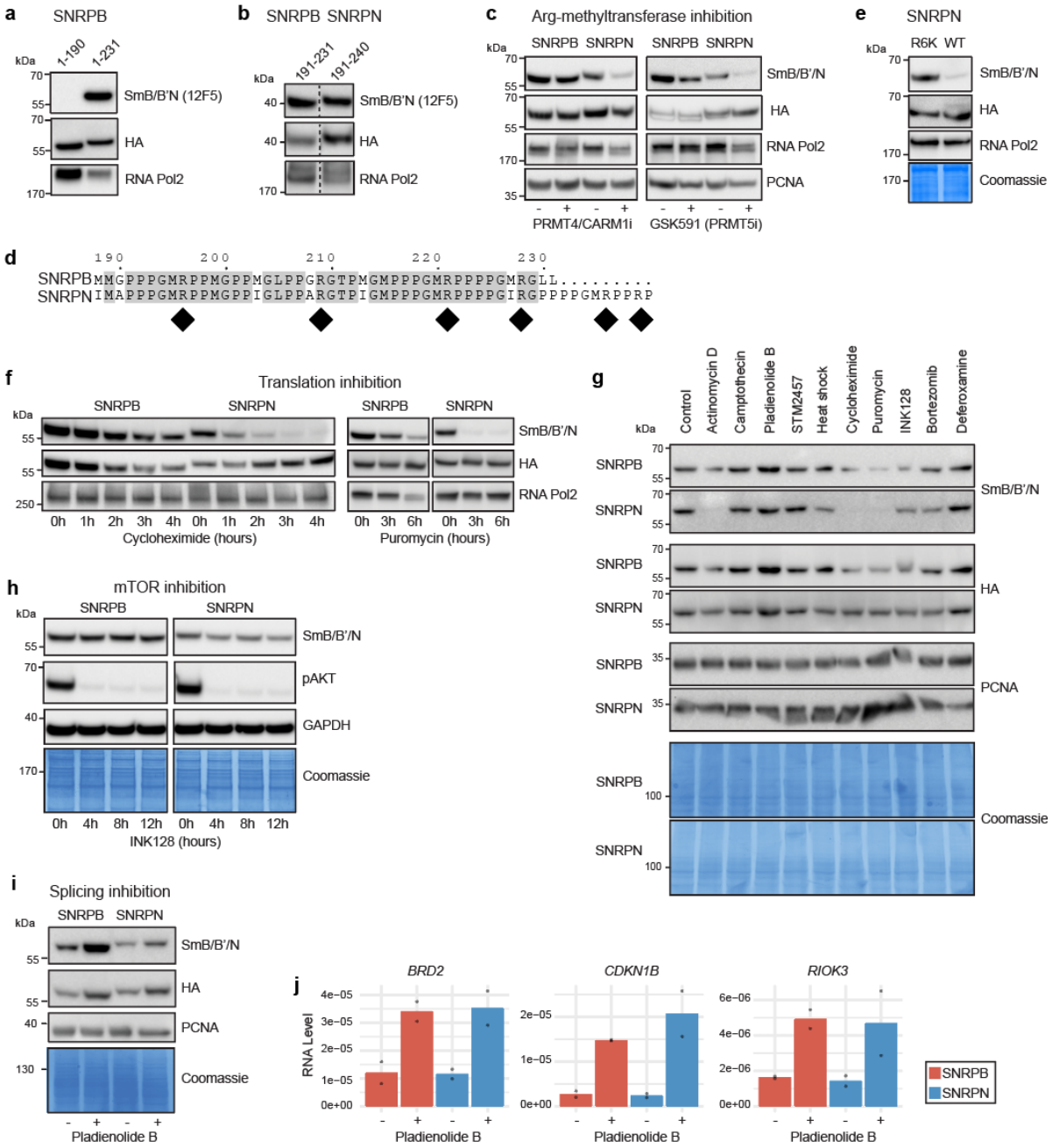

Figure 4. 7. Translation inhibition modulates SNRPB/N states through an arginine methylation-dependent mechanism. (a, b) Epitope mapping of SmB/B'/N monoclonal antibody (12F5) using truncation mutants (SNRPB 1-190, SNRPB 190-231 and SNRPN 190-240) and full-length (SNRPB 1-231) via Western blot. RNA Pol2 serves as loading control. **(c)** Western blot of lysates treated with the type I PRMT intibitor (PRMT4/CARM1i, 5 μM, 27 hours) or type II PRMT5 inhibitor (GSK591, 10 μM, 6-days) obtained from SNRPB- and SNRPN-expressing cells. RNA Pol2 and PCNA serve as loading controls. **(d)** Linear alignment of SNRPB and SNRPN sequences, highlighting the pro-rich region. Diamonds mark the six Arginine residues mutated to Lysine in the R6K mutant. **(e)** Western blot of lysates obtained from SNRPN R6K mutant- and wild-type SNRPN-expressing cells. RNA Pol2 and Coomassie staining serve as loading controls. **(f)** Western blot of lysates treated with 100 μg/mL of Cycloheximide (left) or 20 μM of Puromycin (right) obtained from SNRPB- and SNRPN-expressing cells.

Lysates were obtained at different time points. RNA Pol2 serves as loading control. **(g)** Screening the effect of various stress and pathway perturbation conditions on SNRPB- and SNRPN-expressing cells via Western blot. PCNA and Coomassie staining serve as loading controls. Treatments: Actinomycin D (5 μg/mL, 6-hours), Camptothecin (2 μM, 6-hours), Pladienolide B (100 nM, 16-hours), STM2457 (20 μM, 6-hours), heat shock (43 ^{o}C, 1-hour), Cycloheximide (100 μg/mL, 4-hours), Puromycin (20 μM, 8-hours), INK128 (320 μM, 8-hours), Bortezomib (100 nM, 6-hours), and Deferoxamine (200 nM, 3-hours). **(h)** Western blot of lysates treated with 320 μM of INK128 obtained from SNRPB- and SNRPN-expressing cells. Lysates were obtained at different time points. GAPDH and Coomassie staining serve as loading controls. **(i)** Western blot of lysates treated with 100 nM Pladienoloide B (PlaB) for 16-hours obtained from SNRPB- and SNRPN-expressing cells. PCNA and Coomassie staining serve as loading controls. **(i, j)** Validation of PlaB activity via qRT-PCR. Expression levels were normalized to geometric mean of *RNA 18SN1* and *RNA18SN5* expressions. x-axis represents control (DMSO, -) and PlaB treatment (+) conditions.

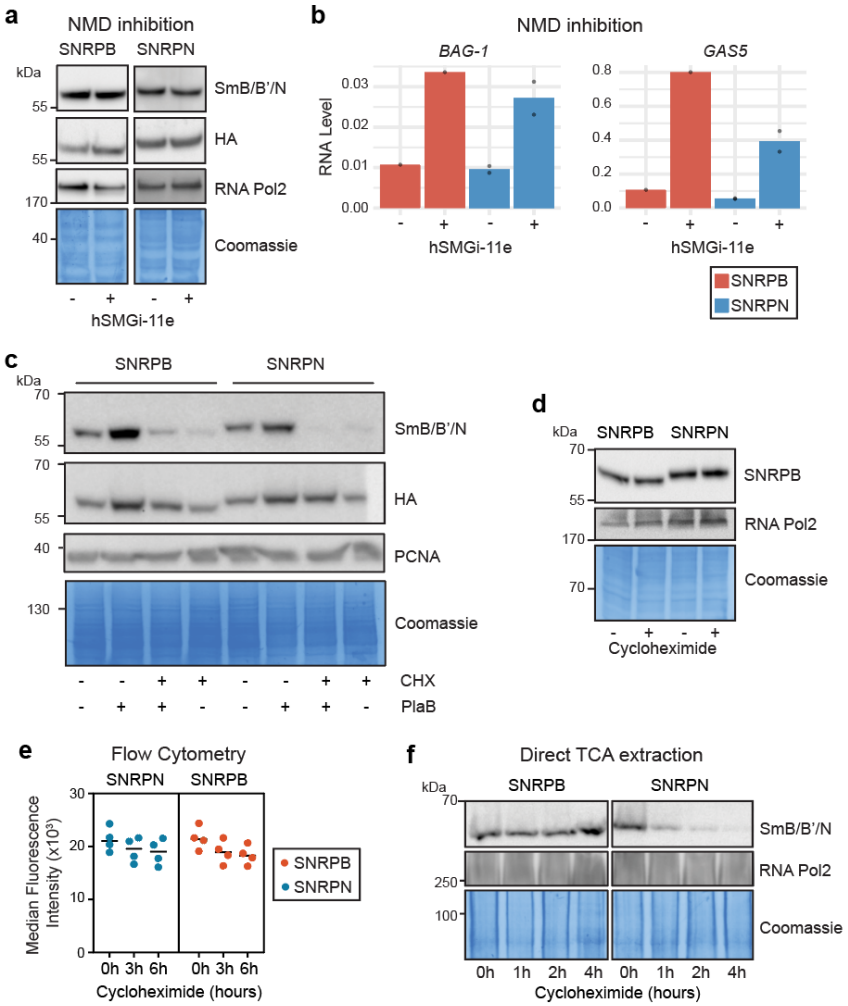

Figure 4. 8. Cycloheximide-induced changes in SNRPN detection by the SmB/B'/N monoclonal antibody (12F5) are not rescued by nonsense mediated RNA decay or splicing inhibition, and are independent of proteasomal degradation. (a) Western blot of lysates treated with 0.6 µM of nonsense mediated RNA decay (NMD) inhibitor (hSMG1i-11e inhibitor) for 24-hours obtained from SNRPB- and SNRPN-expressing cells. RNA Pol2 and Coomassie staining serve as loading controls. **(b)** qRT-PCR validating inhibition of NMD using NMD target genes. Expression levels were normalized to *RPLP0* expression. x-axis represents control (DMSO, -) and hSMGi-11e treatment (+) conditions. **(c)** Western blot of lysates co-treated with Cycloheximide (CHX, 100 µg/mL, 4-hours) and splicing inhibitor Pladienolide B (PlaB, 100 nM, 16-hours). EtOH and DMSO were used as controls of CHX and PlaB, respectively. PCNA and Coomassie staining serve as loading controls. **(d)** Western blot of lysates treated with 100 µg/mL of Cycloheximide for 4-hours. Polyclonal SNRPB antibody raised against recombinant SNRPB expressed in *E.coli* (lacking posttranslational modifications) was used. RNA Pol2 and Coomassie staining serve as loading controls. **(e)** Flow cytometry analysis of lysates treated with 100 µg/mL of Cycloheximide for 0, 3 and 6-hours obtained from SNRPB- and SNRPN-expressing cells. **(f)** Western blot of lysates treated with 100 µg/mL of Cycloheximide obtained from SNRPB- and SNRPN-expressing cells. Samples were collected at different time points. Trichloracetic acid (TCA)-based extraction method was used instead of canonical protein isolation method.

We next wanted to narrow-down the Arg-methylation sites that are part of the SNRPN-PTM cascade induced by translational inhibition. For this, we immunoprecipitated SNRPB/N with/without CHX using the C-terminal HA-tag (data not shown), again followed by PTM quantification by mass spectrometry. Focusing on the pro-rich region after amino acid 190, we could not identify relevant changes for Lysine mono- and dimethylation, or Proline hydroxylation (Figure 4. 9). Arg-mono and dimethylation sites residing in the Arg-Gly rich region remained largely unaffected by CHX treatment (Figure 4. 10. a, b). However, multiple Arg-monomethylation sites within the pro-rich region of SNRPN dropped to undetectable levels after CHX treatment (Figure 4. 10. a), supporting that Arg-methylation is part of the axis leading to the distinct behavior of SNRPB/N.

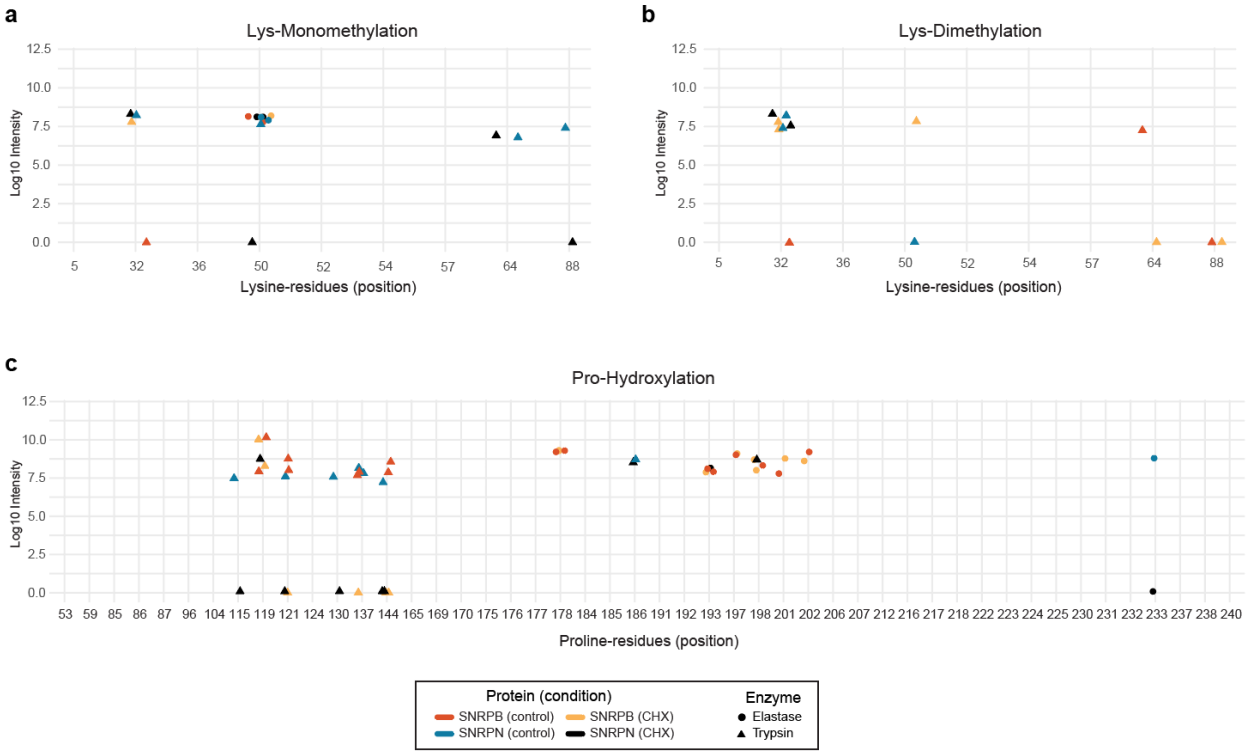

Figure 4. 9. Cycloheximide treatment does not alter Lysine methylation or Proline hydroxylation in SNRPB and SNRPN. (a, b) Mass spectrometry quantification of Lysine monomethylation (a) and Lysine dimethylation (b) intensities for each detected methylated Lysine (Lys) residue in SNRPB and SNRPN. Cells were treated with EtOH (control) or 100 µg/mL of Cycloheximide for 4-hours. Data are shown separately for samples digested with elastase (circles) and trypsin (triangles). x-axis represent the Lysine positions on SNRPB/N. y-axis represent $\log_{10}$ intensities. **(c)** Mass spectrometry quantification of Proline hydroxylation intensities across detected Proline (Pro) residues of SNRPB and SNRPN. Cells were treated with EtOH (control) or 100 µg/mL of Cycloheximide for 4-hours. Data are shown separately for samples digested with elastase (circles) and trypsin (triangles). x-axis represent the Proline positions on SNRPB/N. y-axis represent $\log_{10}$ intensities.

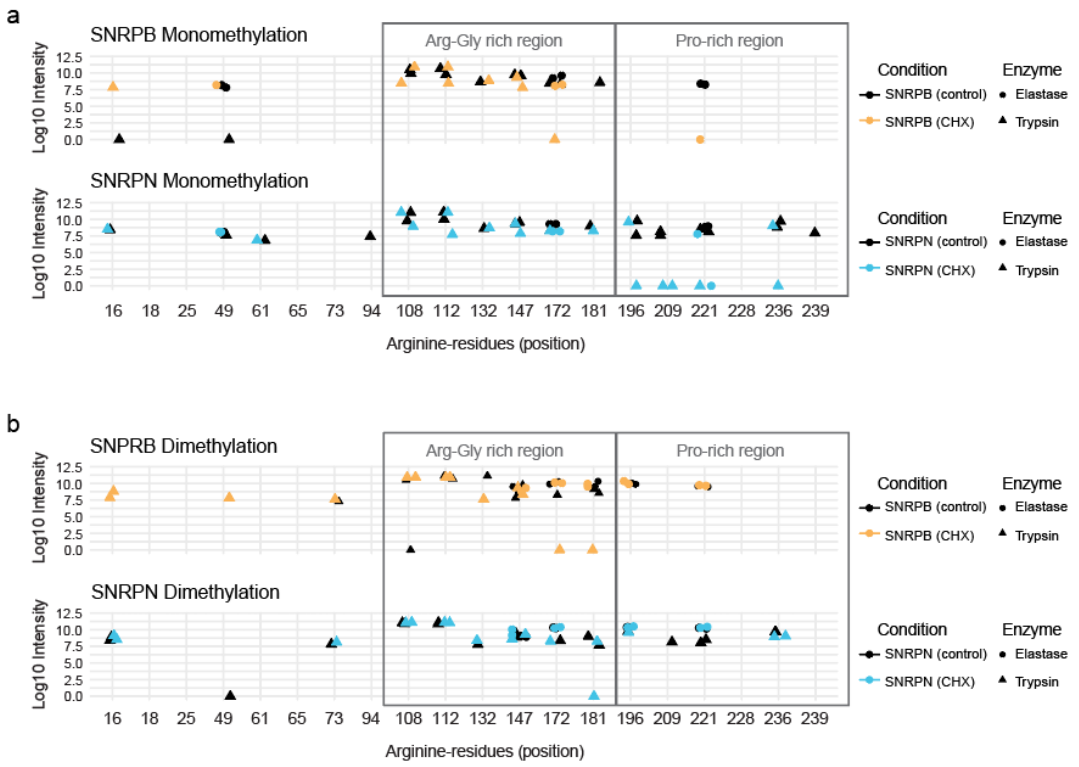

Figure 4. 10. Cycloheximide treatment induces a selective loss of Arginine methylation signals in SNRPN, but not in SNRPB. Mass spectrometry quantification of Arginine monomethylation **(a)** and Arginine dimethylation **(b)** intensities for each detected methylated Arginine (Arg) residue in SNRPB and SNRPN. Cells were treated with EtOH (control) or 100 µg/mL of Cycloheximide for 4-hours. Data are shown separately for samples digested with elastase (circles) and trypsin (triangles). The Arg-Gly-rich and proline-rich regions are indicated by the rectangle boxes.

Accordingly, an SNRPN-R6K mutant, in which all six Arginine residues in the proline-rich region were replaced by Lysine residues, no longer responded to CHX treatment (Figure 4. 11. a). Similarly, mutating four specific Arginine residues (R196, R221, R228, R236) rendered SNRPN resistant, whereas single (R196, R221, R209), double (R196/R221, R236/R239), or triple (R209/R236/R239) mutants retained CHX sensitivity, comparable to the wild-type protein (Figure 4. 11. a). Notably, the two C-terminal Arginine residues unique to SNRPN (R236 and R239), absent in SNRPB due to its shorter C-terminus, are not alone responsible for the observed response (Figure 4. 11. b). Supporting this, replacing the C-terminus of SNRPN with that of SNRPB (SNRPN$^{1\text{-}229}$+LL) preserved CHX sensitivity, similar to full-length SNRPN (Figure 4. 11. b). Conversely, swapping the C-terminal extension of SNRPB with that of SNRPN (SNRPB$^{1\text{-}229}$+PPP) conferred sensitivity (Figure 4. 11. b), suggesting a compound mechanism where both the C-terminus and the additional Arginine residues collectively mediate the response to translation inhibition.

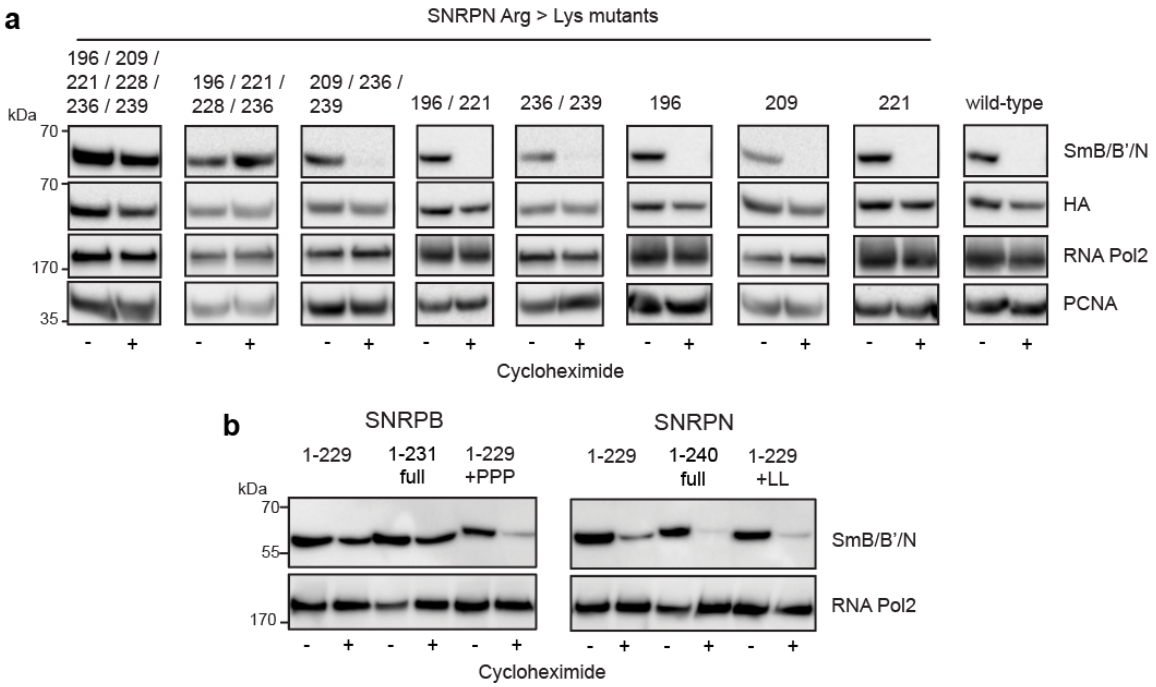

Figure 4. 11. Arginine residues in the SNRPN C-terminal region are required for SmB/B'/N monoclonal antibody (12F5) recognition after cycloheximide treatment. (a) Western blot of lysates obtained from Arginine-to-Lysine (Arg > Lys) mutants and wild-type SNRPN. Cells were treated with EtOH (-) or 100 µg/mL of Cycloheximide (+) for 4-hours. Mutants contain combinations or individual substitutions at residues Arg196, Arg209, Arg221, Arg228, Arg236, and Arg239. RNA Pol2 and PCNA serve as loading controls. **(b)** Western blot of truncation (1-229), wild-type (1-231 for SNRPB and 1-240 for SNRPN) and mutant constructs of SNRPB (1-229+PPP) and SNRPN (1-229+LL) under 4-hour EtOH (-) or Cycloheximide (+) treatments. RNA Pol2 serves as loading control.

4.4. Nuclear context and the SNRPN-specific epitope loss by CHX-responsive interactions

To investigate the cellular context of the Arginine-SNRPB/N axis we performed staining and microscopy to characterize SNRPB/N localization after translation inhibition. In control conditions (-CHX), the mNeon signal was predominantly nuclear as indicated by a nuclear-to-cytoplasm ratio of around 9 for both paralogues (Figure 4. 12. a, b). Cajal bodies remained intact after CHX treatment (Figure 4. 13. a) and remained co-localized with SNRPB/N-mNeon, but the number of both Coilin and mNeon foci per cell significantly decreased (Figure 4. 13. b, c). The SmB/B'/N (12F5) signal showed weaker nuclear enrichment in untreated and control conditions compared to the mNeon signal (Figure 4. 12. b, c). Interestingly, SNRPN cells exhibited a nuclear-to-cytoplasmic ratio close to 1 (12F5 staining), indicating an equal

distribution, which was significantly different from SNRPB-expressing cells (ratio around 2) (Figure 4. 12. a, b). Upon CHX treatment, the mNeon intensity - reflecting the overall levels of SNRPB/N protein - decreased in the cytoplasm, while it remained unaffected in the nucleus (Figure 4. 12. c). 12F5 signal in the cytoplasm decreased for both paralogues following CHX, but nuclear 12F5 intensity remained unaffected for SNRPB, while being fully lost for SNRPN (Figure 4. 12. c). This was also reflected in the dynamics of SNRPB/N association with Cajal bodies. Fluorescence recovery after photobleaching (FRAP) experiments showed that in control conditions (-CHX), the SNRPB/N dynamics with Cajal bodies are similar (Figure 4. 14. a, b). However, after CHX treatment there was a significant difference, where SNRPN association with foci became slower compared to SNRPB (Mean half recovery time SNRPB 1.83 sec, SNRPN 2.22 sec; padj=0.0292), while there were no differences in the mobile fraction (around 70% in all conditions) (Figure 4. 14. a, c).

Comparing the 12F5 with the mNeon signal indicates that the cytoplasmic population (likely the unmethylated protein (Paushkin et al. 2002) and Figure 4. 7. e) is a minor fraction of the overall SNRPB/N. Considering that cytoplasmic mNeon signal decreases upon CHX - potentially explaining part of the 12F5 signal loss - and that nuclear 12F5-intensities already differ in untreated conditions, these microscopy analyses suggest that (1) the SNPRN-associated epitope change preventing 12F5 recognition occurs in the nucleus already under normal conditions; (2) it is boosted upon translation inhibition by CHX; and (3) SNRPB in the nucleus is protected from the change.

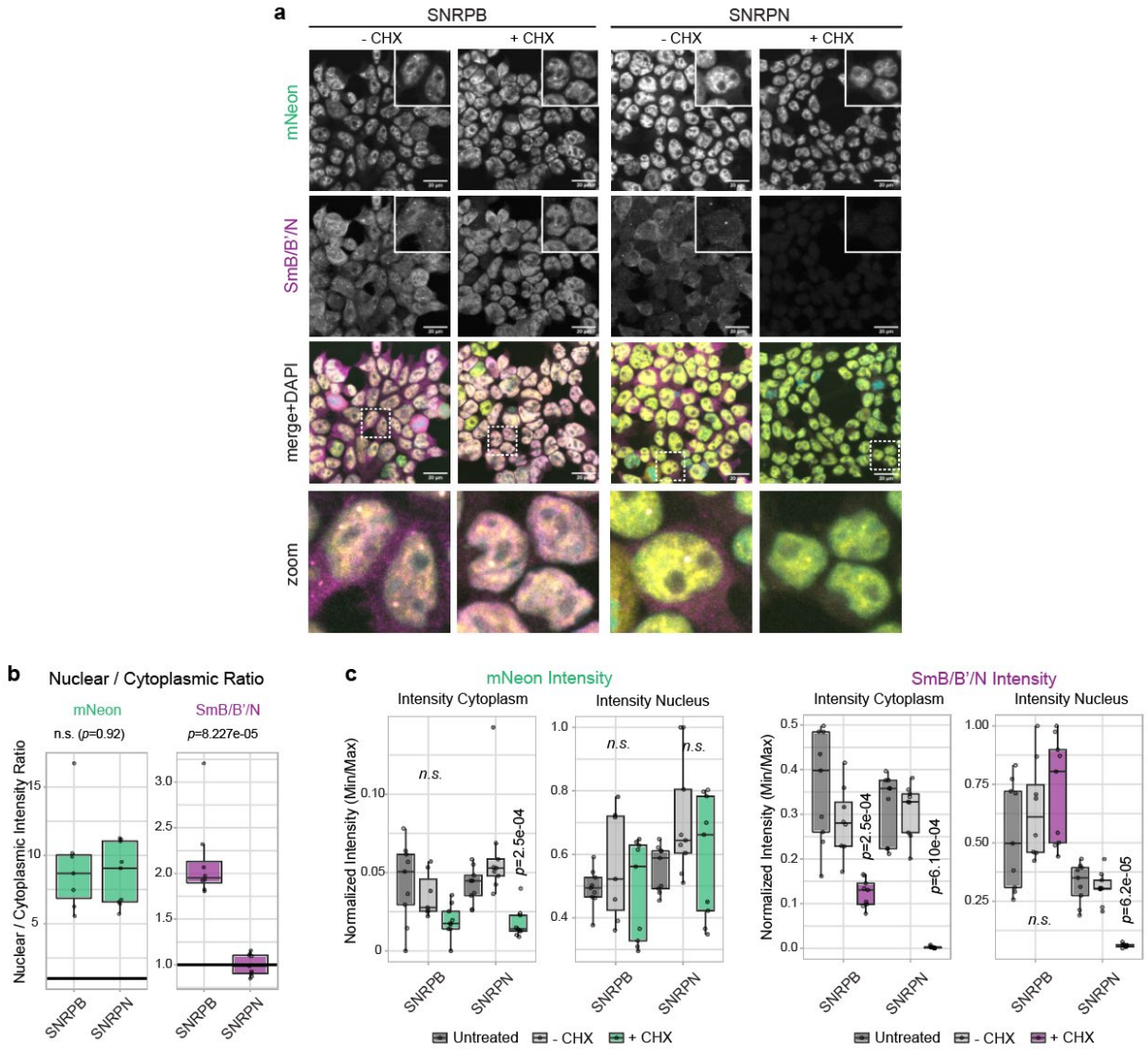

Figure 4. 12. Cycloheximide treatment induces a selective nuclear loss of 12F5 epitope in SNRPN, but not in SNRPB. **(a)** Representative fluorescence microscopy pictures of SNRPB- and SNPRN-expressing cells treated with EtOH (-CHX) or Cycloheximide (+CHX, 100 µg/mL, 4-hours). The auto fluorescent mNeon signal (green in merged panel) marks expression of the Snrpb and Snrpn transgenes. SNRPB and SNRPN were detected by immunostaining with the 12F5 monoclonal antibody (SmB/B'/N) (magenta in merged panel). DAPI stains nuclei (blue in merged panel). The areas marked with a dashed square are magnified in the "zoom" panel. Data obtained from two independent replicates. Scale bars: 20 µM **(b)** Quantification of fluorescence microscopy in (b) for the mNeon and 12F5-immunostained (SmB/B'N) channel. The boxplot shows the nuclear / cytoplasmic intensity ratios in each quantified field-of-view shown as an overlaid datapoint. The *p*-values were obtained by a Wilcoxon rank sum exact test. **(c)** Quantification of fluorescence microscopy in (b) for the mNeon and 12F5-immunostained (SmB/B'N) channel. The boxplot shows the normalized intensities for the cytoplasm (left) and nucleus (right). The adjusted *p*-values were obtained with a Pairwise Wilcoxon rank sum exact test with Benjamini-Hochberg correction.

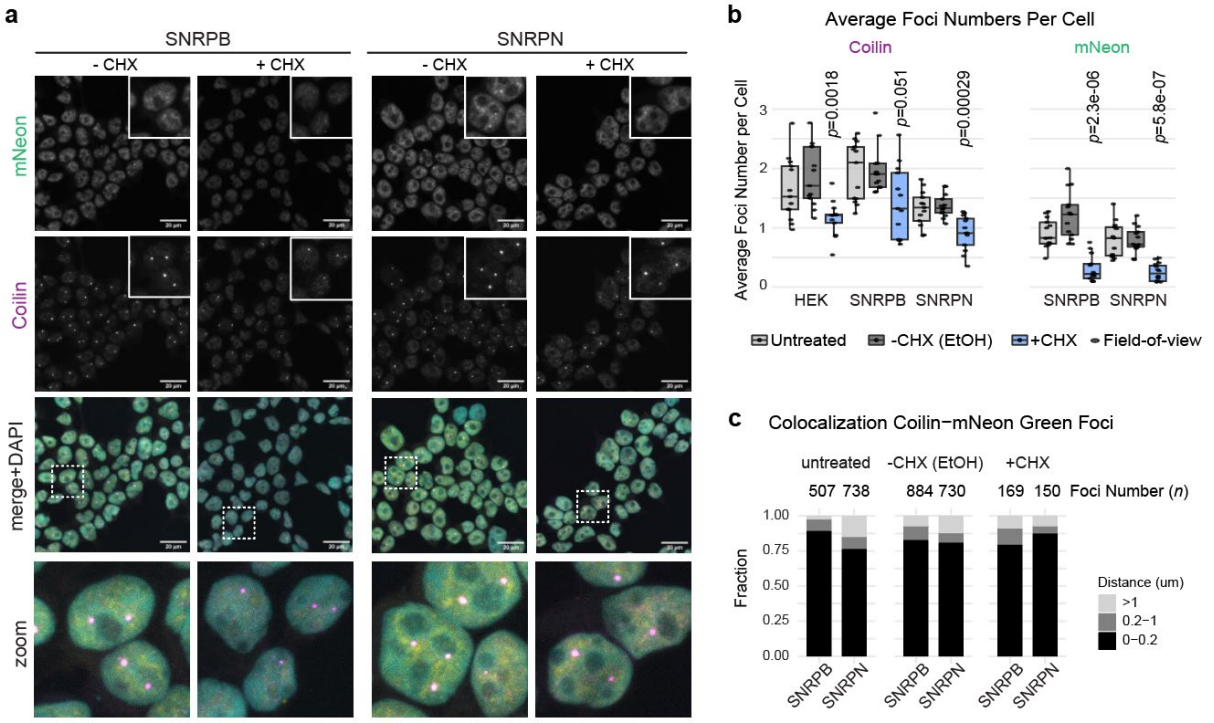

Figure 4. 13. Cycloheximide treatment reduces the number of nuclear foci, but not the colocalization of Cajal bodies with SNRPB and SNRPN. (a) Representative fluorescence microscopy pictures of SNRPB- and SNPRN-expressing cells treated with EtOH (-CHX) or Cycloheximide (+CHX, 100 µg/mL, 4-hours). The auto fluorescent mNeon signal (green in merged panel) marks expression of the Snrpb and Snrpn transgenes. Cajal bodies were detected by immunostaining with the Coilin monoclonal antibody (magenta in merged panel). DAPI stains nuclei (blue in merged panel). The areas marked with a dashed square are magnified in the "zoom" panel. Data obtained from two independent replicates. Scale bars: 20 µM **(b)** Quantification of (a). Boxplot showing the average foci numbers per cell in a given field of view. Foci were identified from the Coilin (left) and mNeon (right) channels and divided per the total number of cells (manually counted) in a given field of view. Each dot represents the result of one field of view and the boxplot shows the distribution across fields-of-view. The total quantified cell numbers were HEK untreated (*n*=578), HEK-CHX (*n*=541), HEK+CHX (*n*=359), SNRPB untreated (*n*=580), SNRPB-CHX (*n*=737), SNRPB+CHX (*n*=579), SNRPN untreated (*n*=918), SNRPN-CHX (*n*=876), SNRPN+CHX (*n*=692). The adjusted p-values were obtained with a Pairwise Wilcoxon rank sum exact test with Benjamini-Hochberg correction and shown for the Ethanol (-CHX) versus +CHX condition(padj<0.05). The untreated control experiment was stained and acquired simultaneously and is shown in Figure 4.1.e. **(c)** Quantification of (a). Stacked bar plot showing the distance between Coilin and mNeon foci as a fraction in 3 groups (>1 µm,0.2-1 µm and 0-0.2 µm). The number of identified foci is given in the figure, for the cell numbers see (b).

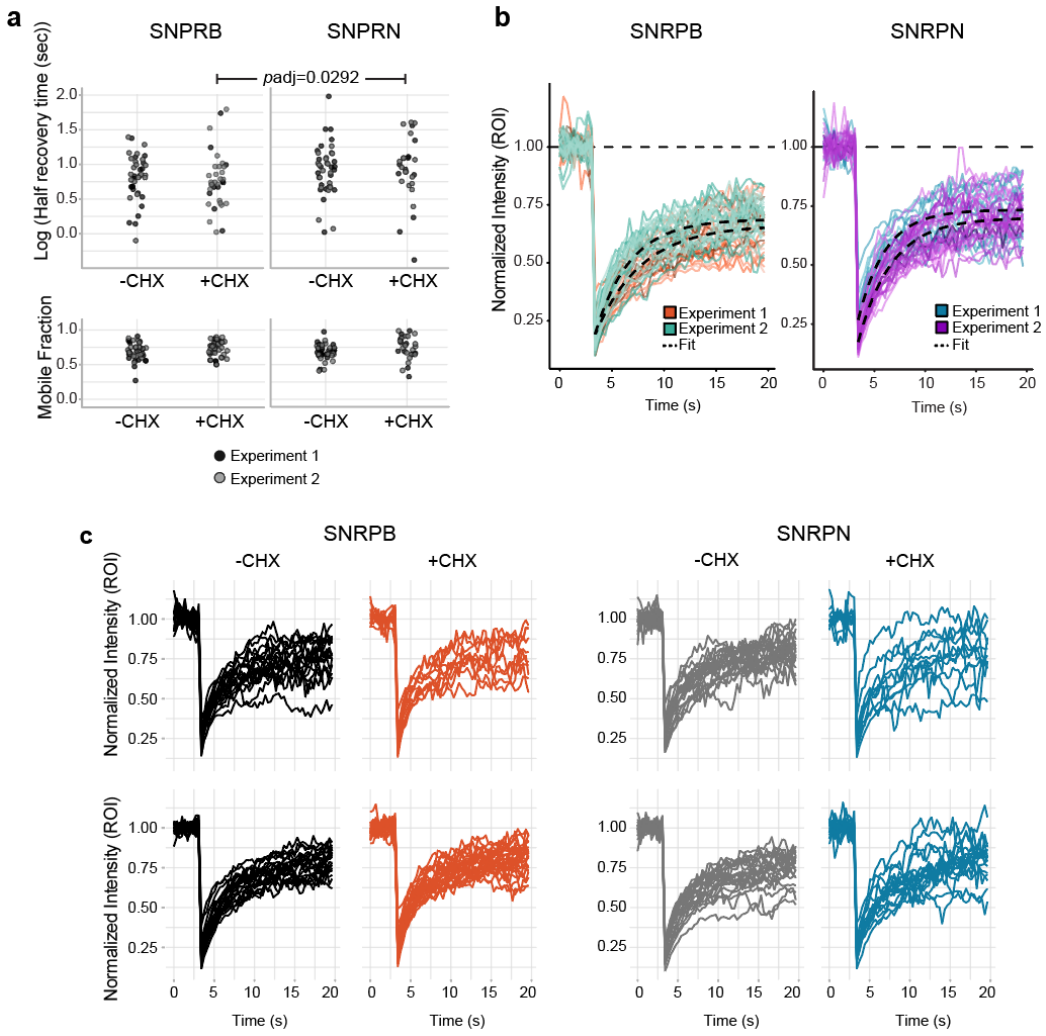

Figure 4. 14. Cycloheximide treatment selectively alters SNRPN dynamics in Cajal bodies. (a) Quantification of FRAP (fluorescence recovery after photobleaching) kinetics of SNRPB and SNRPN before (-CHX) and after cycloheximide (+CHX, 100 µg/mL, 4-hours) treatment. The top panel shows the log-transformed half-recovery times and the bottom panel shows the mobile fraction of mNeon-tagged SNRPB and SNRPN in Cajal bodies per bleached focus, under Ethanol (-CHX; Control) and cycloheximide treated (+CHX) conditions. Each dot represents a single focus from two independent replicates (black and gray). The adjusted p-value shown compares the half-recovery times of SNRPN between -CHX and +CHX conditions. **(b)** Normalized FRAP recovery curves for individual foci of SNRPB (left) and SNRPN (right) from two independent experiments. Solid lines represent raw data: dashed lines show fitted recovery curves. **(c)** Raw intensity recovery traces from two example experiments showing SNRPB (left) and SNRPN (right) foci under Ethanol (-CHX; Control) and cycloheximide treated (+CHX, 100 µg/mL, 4-hours) conditions. Each line corresponds to one bleached focus. FRAP was performed by bleaching mNeon-tagged SNRPB and SNRPN foci in living cells and recording fluorescence recovery over time. Intensity traces were normalized by subtracting background signal and adjusting for nuclear intensity and pre-bleach baseline.

To analyze this, we profiled SNRPB/N interaction partners in CHX versus the control condition. The interaction with the major spliceosome components as well as the methylosome complex remained largely unaffected for both paralogues (Figure 4. 15. a). Among all identified interaction partners, many retained comparable association with SNRPB/N, especially the ones that were highly enriched (log2FC > 6) (Figure 4. 15. a, b). However, there were also some interaction partners that changed after CHX treatment (Figure 4. 15, c, d). Given the IF results (Figure 4. 12. a, c), we focused on nuclear proteins, many of which showed concordant changes after CHX in both SNRPB and SNRPN (diagonal / yellow dots in Figure 4. 16. a). However, there were also some with different behavior for the paralogues after CHX (Figure 4. 16. a). Examples of proteins only interacting in the SNRPB+CHX condition were MEIS1, LMO7, PGAM2, DENND4A. Among the proteins that gained interaction with SNRPN after CHX, but did score in any of the other conditions were PHIP, ZNF280C, BAZ1B, H2AX, MACROH2A1 or GTF3A - those are related to stress response and DNA repair processes. HDHD3 (putative hydrolase with unknown function), INTS8 (cleaves small nuclear RNAs U1 and U2 within the nucleus), TLE3 (transcriptional co-repressor which displays Arg-me binding sensitivity for CBP (Dittmar et al. 2019) and ATR (serine/threonine kinase and DNA damage sensor) lost interaction with SNRPN after CHX but never interacted with SNRPB. Proteins exclusively lost in the SNRPN+CHX conditions were chromatin factors such as CENPH (Centromere protein), EYA4 (Phosphatase for H2AX-Y142ph), KBTBD6 (Ubiquitin-Ligase cofactor) or ZBTB33 (Transcription factor for repressive chromatin). Similar results were obtained when simply performing overlaps among significantly enriched proteins (p_{adj}<0.001, log_2FC > 2) (Figure 4. 16. b). We performed various functional enrichment analysis (KEGG, GOTerm, etc.), which did not reveal any functional connection. Indeed, among the interaction partners a minority were subunits of the same complex, but were rather singletons (Figure 4. 16. c). However, we found that the interactors were significantly enriched for containing monomethyl-Arginine (MMA), but not dimethyl-Arginine sites (Figure 4. 16. d), thus forming a hub of “MMA” proteins together with SNRPB/N.

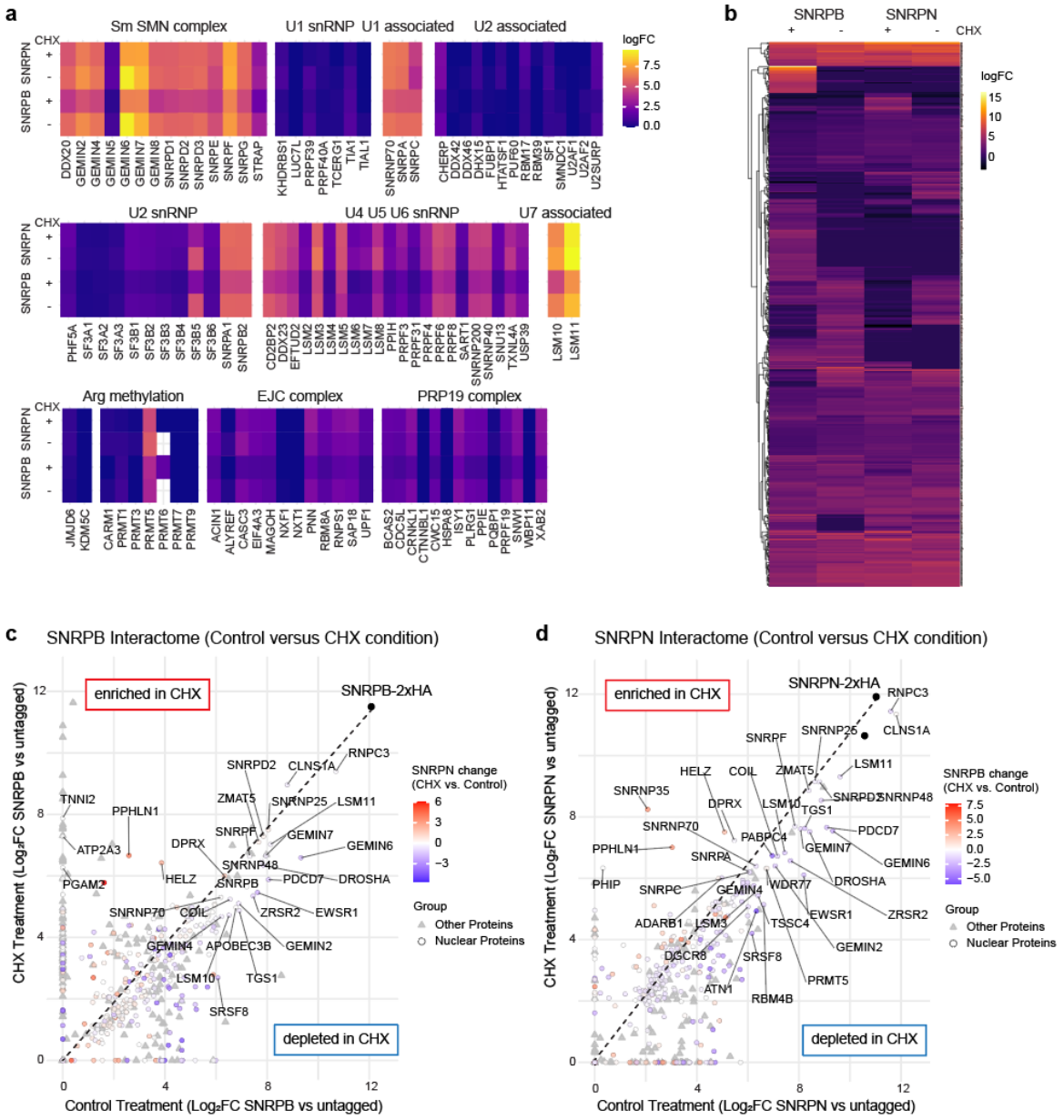

Figure 4. 15. Cycloheximide treatment alters the interactomes of both SNRPB and SNRPN while leaving core spliceosomal and methylosome interactions largely intact. **(a)** Heatmaps displaying the $\log_2$ fold enrichment of known interaction partners of SNRPB and SNRPN – including components of the Sm/SMN complex, U snRNPs-associated factors, and Arginine methylation machinery – under Ethanol (-CHX; Control) and cycloheximide-treated (+CHX, 100 µg/mL, 4-hours) conditions. **(b)** Heatmap showing the clustering of all proteins significantly enriched in the interactomes of SNRPB and SNRPN across under Ethanol (-CHX; Control) and CHX-treated (+CHX, 100 µg/mL, 4-hours) conditions. Proteins with similar interaction profiles are grouped together based on their enrichment patterns in control and CHX-treated samples. **(c, d)** Scatter plots comparing the interactomes of SNRPB (c) and SNRPN (d) between untagged control and CHX conditions. Axes show $\log_2$ fold enrichment of SNRPB/N versus untagged control in Ethanol (control) condition on the x-axis and CHX-treated condition on the y-axis. Proteins enriched (upper left) or depleted (lower right) in CHX are labeled.

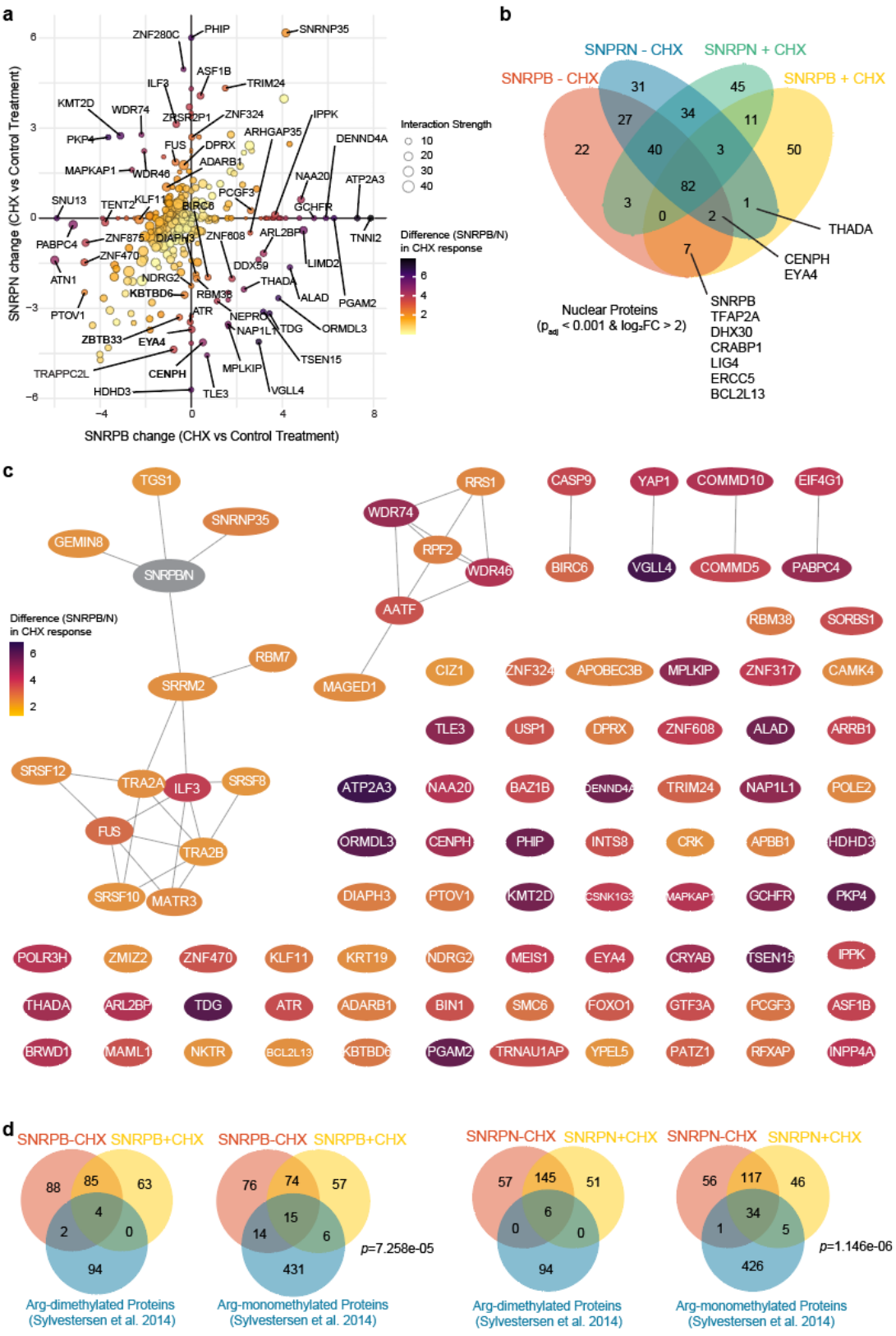

Figure 4. 16. Cycloheximide-sensitive SNRPB/N interactors form a monomethyl-Arginine-enriched protein network. (a) Comparative scatter plots showing the interaction changes of SNRPB and SNRPN following cycloheximide treatment (100 µg/mL, 4-hours), based on log_2 fold changes relative to control (EtOH treatment). **(b)** Venn diagram showing the overlap of significantly enriched proteins in SNRPB and SNRPN immunoprecipitates under Ethanol (-CHX; Control) and

cycloheximide-treated (+CHX, 100 µg/mL, 4-hours) conditions. Significantly enriched nuclear interactors are listed (p_{adj}<0.001, log_2FC>2). **(c)** Network diagram of the selected SNRPN interactors whose association was preferentially altered following CHX treatment (100 µg/mL, 4-hours). Each circle represents a protein, and connecting lines indicate known or predicted functional interactions. **(d)** Venn diagrams comparing Arginine-methylated proteins previously reported (Sylvestersen et al. 2014) to those enriched in SNRPB and SNRPN interactomes under Ethanol (-CHX; Control) and CHX-treated (+CHX, 100 µg/mL, 4-hours) conditions. Statistical significance of overlaps was assessed using a two-sided Fisher's exact test.

4.5. Paralogue-specific modulation of SNRPB/N in different tissues and upon metabolic insults

Using 12F5 along with the polyclonal SNRPB antibody as a tool, we examined SNRPN expression and modification across various contexts. As expected, SNRPN was detected in mouse brain lysates via Western blot using the polyclonal antibody, but interestingly, no signal was observed with 12F5 (Figure 4. 17. a). We then we screened various cell lines and found that human induced pluripotent stem cells (hiPSCs) express high amounts of SNRPN, though 12F5 detected it only weakly (Figure 4. 17. a). Unlike HEK cells, hiPSCs do not express SNRPB splice variant SNRPB' (Figure 4. 17. b), and expression and translation of SNRPN in hiPSCs were further confirmed in published RNA-seq and ribosome profiling data (Tomuro et al. 2024) (Figure 4. 17. C, see also (Rohm et al. 2025)). SNRPN in hiPSCs was sensitive to CHX (Figure 4. 17. d). Similarly, hiPSC-derived human neurons expressed high levels of SNRPN, with 12F5 detection being faint and fully abolished by CHX (Figure 4. 17. e). Contrary to earlier reports (Sharpe, Williams, and Latchman 1990), we detected only SNRPB, not SNRPN, in F9 cells (Figure 4. 17. f). In addition, 12F5 detected a CHX-sensitive SNRPB' (SNRPB splice variant) in chicken cells (Figure 4. 17. g).

We suspected that the different growth media in these cells and nutritional influences in the animals from which our tissues were isolated might be responsible for these differences – presumably revolving around the mTOR pathway, a critical upstream regulator of nutrient sensing and protein translation. We scrutinized the basal growth media components for key differences between hiPSCs (E8 media), hiPSC-derived neurons (BrainPhys media) and HEK cells (DMEM high glucose) (Figure 4. 18. a). DMEM differs tremendously from the other media by the high concentrations of Glucose and L-Glutamine. E8 media (0.684 mM) contains higher Arginine concentrations than DMEM (0.398 mM) or BrainPhys (0.4886 mM). Other amino acids show no differences that would explain the behavior of SNRPN in DMEM growth media. We thus investigated the impact of changing these components and the metabolic state of the cells. Intriguingly, Arginine depletion from the media phenocopied the effect of CHX inducing

a loss of the 12F5 band for SNRPN, while SNRPB was unaffected (Figure 4. 18. b). Hypoxic conditions, which push HEK cells to favor glycolysis over OXPHOS, rendered SNRPB sensitive to CHX treatment (Figure 4. 18. c).

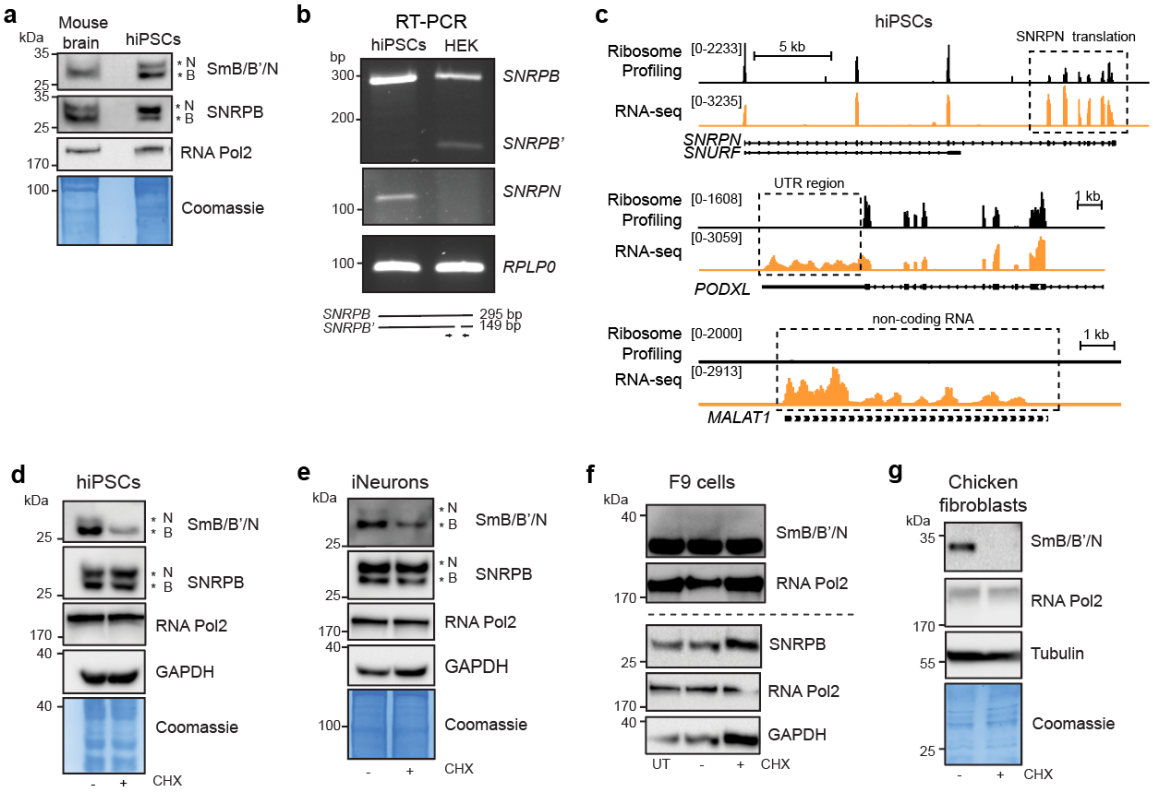

Figure 4. 17. SNRPB/N expression and 12F5 antibody reactivity vary across cell types and are sensitive to cycloheximide treatment. (a) Western blot of mouse brain and hiPSC lysates using 12F5 antibody (SmB/B'/N, PTM-sensitive) and SNRPB antibody (PTM-insensitive). RNA Pol2 and Coomassie staining serve as loading controls. **(b)** RT-PCR of *SNRPB, SNRPB'*, and *SNRPN* in hiPSCs and HEK cells shows the absence of *SNRPB'* in hiPSCs. *RPLP0* was used as a control. **(c)** RNA-seq (orange) and ribosome profiling data (black) from hiPSCs (Tomuro et al. 2024; Rohm et al. 2025) showing *SNRPN* expression. *PODXL* and *MALAT1* serve as positive controls for UTR-associated and non-coding transcripts, respectively. **(d, e)** Western blots of hiPSCs (d) and hiPSC-derived neurons (iNeurons) (e) treated with EtOH (-) or Cycloheximide (+, 100 µg/mL, 4-hours) using 12F5 and SNRPB antibodies. 12F5 detects SNRPN weakly in both cell types, while no signal is detected upon CHX. RNA Pol2, GAPDH and Coomassie staining serve as loading controls. **(f)** Western blot of F9 cells untreated (UT) or treated with EtOH (-) or Cycloheximide (+, 100 µg/mL, 4-hours) using 12F5 and SNRPB antibodies shows detection of SNRPB only. RNA Pol2 and GAPDH serve as loading controls. **(g)** Western blot of chicken fibroblasts treated with EtOH (-) or Cycloheximide (+, 100 µg/mL, 4-hours) showing 12F5 detects SNRPB splice variant SNRPB'. Tubulin and Coomassie staining serve as loading controls.

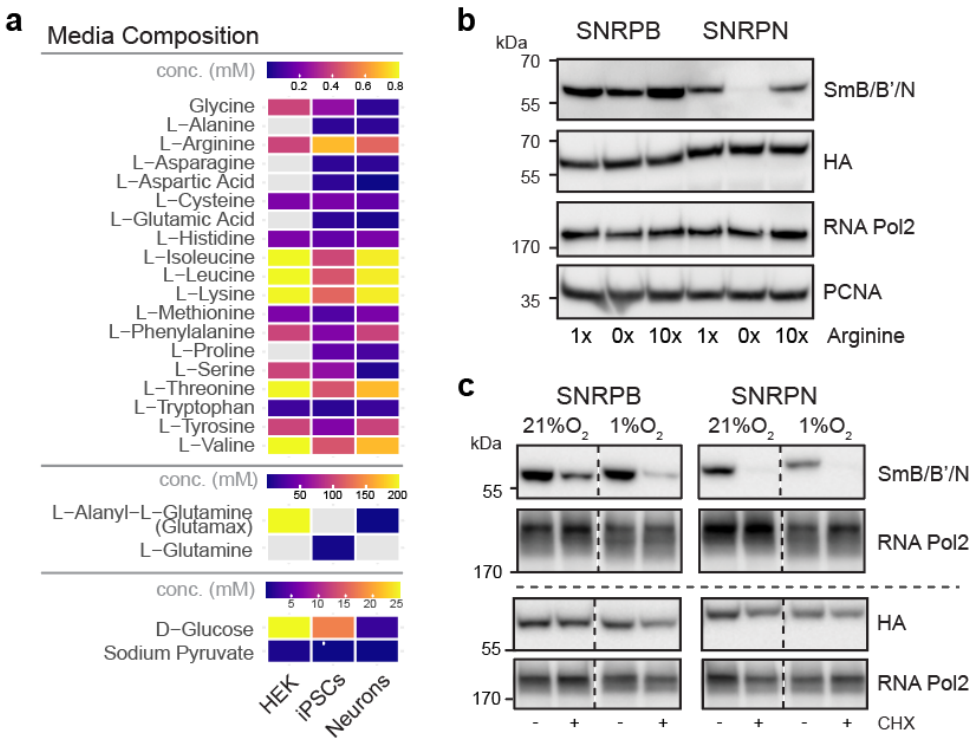

Figure 4. 18. Detection of SNRPN by the PTM-sensitive 12F5 antibody is regulated by nutrient composition and cellular metabolic state. (a) Heatmap comparison of basal media composition for HEK cells (DMEM), hiPSCs (E8), and hiPSC-derived neurons (BrainPhys) showing concentrations of Glucose, L-Glutamine, and selected amino acid, including L-Arginine. **(b)** Western blot of HEK cells expressing SNRPB or SNRPN cultured in media containing 1x, 0x, and 10x L-Arginine. RNA Pol2 and PCNA serve as loading controls. **(c)** Western blot of HEK cells expressing SNRPB or SNRPN cultured under normoxic (21% O_2) or hypoxic (1% O_2) conditions. Cells were treated with EtOH (-) or Cycloheximide (+, 100 µg/mL, 4-hours). RNA Pol2 serves as loading control.

4.6. Nutrient-responsive splicing programs orchestrated by SNRPB/N

To investigate the transcriptomes following translation inhibition, we performed RNA-seq after 4-hours CHX treatment in SNRPB and SNRPN cells. Principal component analysis (PCA) revealed distinct profiles between the two cell types that were further amplified after treatment (Figure 4. 19. a). As expected, CHX induced widespread gene expression changes: 3,348 genes were upregulated and 2,809 downregulated in SNRPB cells, while 4,887 were upregulated and 3,982 downregulated in SNRPN cells (Figure 4. 19. b). We examined the behavior of genes that we had previously found to be preferentially stabilized in SNRPB and SNRPN cells (Figure 4. 2. b). These showed no consistent trend after treatment – some were upregulated and others downregulated (Figure 4. 19. d). Additionally, we assessed specifically the subgroup of SNRPB/N targets whose expression remained unchanged following CHX (1,137 CHX-resistant in SNRPB, 803 CHX-resistant in SNRPN) (Figure 4. 19. d). However, KEGG pathway and other functional analyses revealed no significant enrichment among these genes (data not shown).

Therefore, we aimed at identifying cell-type-specific responses to CHX and generated Venn diagrams (Figure 4. 19. c). Although there was a substantial number of genes overlapped between the two cell types (3,131 upregulated and 2,510 downregulated), CHX also triggered unique responses: 1,752 genes were uniquely upregulated and 1,471 downregulated in SNRPN cells, compared to 216 upregulated and 299 downregulated only in SNRPB cells (Figure 4. 19. c). KEGG analysis showed that SNRPN-specific CHX-responsive genes were enriched in pathways including Riboflavin metabolism, Glutamine metabolism, Arginine/Proline metabolism, and Ubiquitin-mediated proteolysis (Figure 4. 19. e). In SNRPB cells, enrichment was observed for example in Selenocompound and Sulfur metabolism, albeit with lower significance (Figure 4. 19. f).

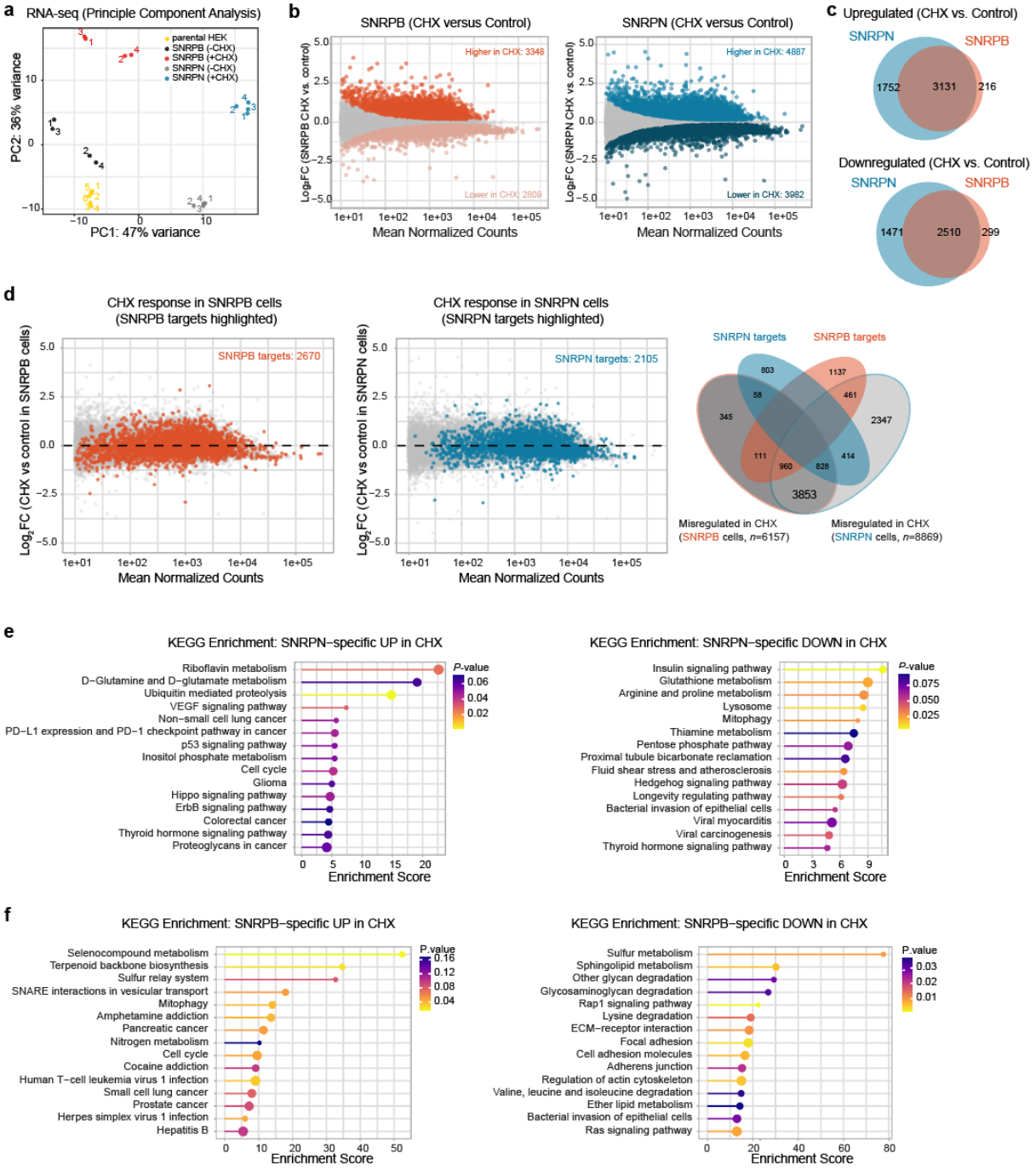

Figure 4. 19. Transcriptomic responses to cycloheximide treatment differ between SNRPB and SNRPN cells. (a) Principal component analysis (PCA) of RNA-seq data from parental HEK cells, and SNRPB and SNRPN cells treated with EtOH (-CHX) or CHX (100 µg/mL, 4-hours). **(b)** MA plots showing differential gene expression after CHX treatment in SNRPB (left) and SNRPN (right) cells. **(c)** Venn diagrams displaying overlapping and unique sets of CHX-upregulated (top) and downregulated (bottom) genes in SNRPB and SNRPN cells. **(d)** Differential expression plots showing the response previously identified SNRPB- and SNRPN-specific target genes (from Figure 4. 2. b) to CHX in SNRPB (left) and SNRPN (middle) cells. The Venn diagram (right) shows CHX-responsive and CHX-resistant SNRPB/N targets across both cell lines. **(e, f)** KEGG enrichment for CHX-specific responses in SNRPN (e) and SNRPB (f) cells.

Upon investigation of the gene features, we found that CHX-upregulated genes in SNRPN cells were generally longer, with increased cumulative intron length and a higher frequency of genes with very long introns (Figure 4. 20. a). In contrast, CHX-downregulated genes tended to have longer introns in SNRPB cells, suggesting their preferential destabilization (Figure 4. 20. a). In addition, CHX-responsive, downregulated genes had fewer introns than non-regulated genes, with minor differences between cell lines (Figure 4. 20. b). In SNRPN cells, there was a larger fraction of genes with a high number of introns (16 or more) that stabilized in CHX. Given that transcript processing is a key determinant of mature mRNA abundance, these findings suggest that, under conditions of translation inhibition or nutrient stress, SNRPN has a greater capacity than SNRPB to efficiently splice and stabilize transcripts containing long introns.

To investigate whether these features – besides affecting splicing more generally – also has implications for alternative splicing we analyzed our data using rMATS. After stringent filtering, we focused on events with significant differential alternative splicing (FDR < 0.01) between CHX-treated and control samples. Although numerous events met this threshold, manual inspection with the genome browser revealed that many were not specific to SNRPB/N cells but instead reflected a general response (e.g., *AKAP8L;* Figure 4. 20. c). Interestingly CHX treatment led to a pronounced reduction in alternative splicing (Figure 4. 20. d), indicating a global shift toward constitutive isoform usage and reduced isoform diversity. Exon skipping was the least decreased alternative splicing event, while the other events (Alternative 5' or 3' splice site, Mixed Events and Intron Retention) were drastically decreased. We asked whether the few alternative splicing events that are more pronounced in CHX (i.e. creating more isoform diversity upon treatment) overlap between SNRPN and SNRPB cells. There was very little overlap, and after manual inspection of the few remaining events we noticed that again many were false positives.

Supporting this, independent analyses using IRFinder and VAST-tools comparing SNRPN to SNRPB cells identified fewer than 10 significant events, suggesting that modulation of splicing efficiency – rather than alternative splicing – is the predominant global outcome orchestrated by these paralogues after translation inhibition.

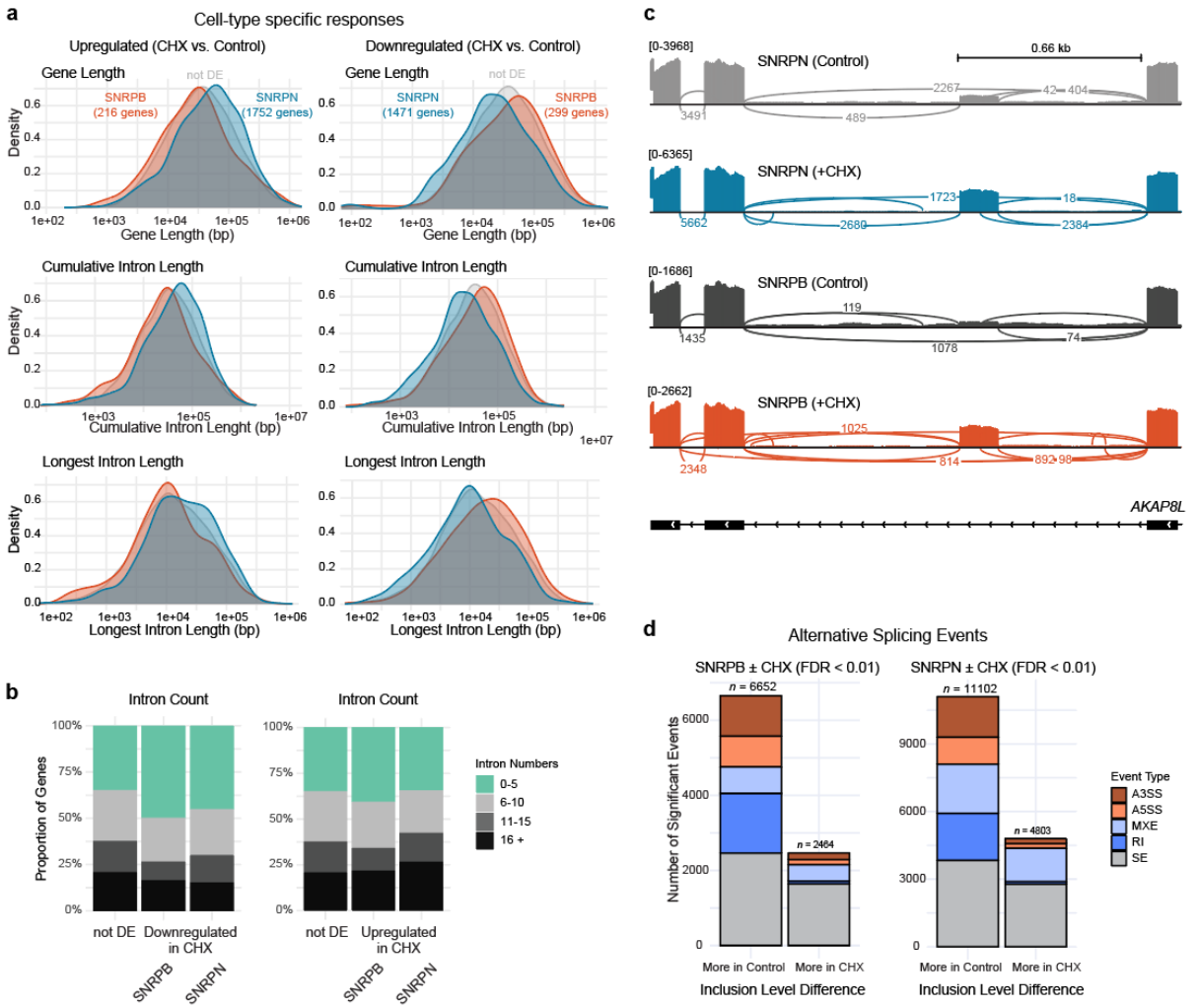

Figure 4. 20. Cycloheximide treatment reveals distinct gene architecture and alternative splicing responses in SNRPB and SNRPN cells. **(a)** Density plots showing the distribution of gene length, cumulative intron length, and the longest intron length for genes upregulated (left) or downregulated (right) after CHX treatment (100 µg/mL, 4-hours) relative to control (EtOH treatment) in SNRPB- (red) and SNRPN-expressing cells (blue). **(b)** Bar plots showing the proportion of genes with different intron counts (0-5, 6-10, 11-15, 16+) among unchanged (not DE), downregulated and upregulated genes in SNPRB- and SNPRN-expressing cells. **(c)** Sashimi plots showing read coverage and splice junctions at the *AKAP8L* locus in control (EtOH-treated) and CHX-treated (100 µg/mL, 4-hours) conditions for SNRPB- and SNRPN-expressing cells. **(d)** Bar plots summarizing the number of significant alternative splicing events (FDR < 0.01) identified by rMATS between control (EtOH-treated) and CHX-treated (100 µg/mL, 4-hours) samples obtained from SNRPB- and SNRPN-expressing cells. Events are classified as skipped exons (SE), retained introns (RI), mutually exclusive exons (MXE), and alternative 5' or 3' splice sites (A5SS, A3SS). Events are grouped by direction of inclusion level change (more in control versus more in CHX), with the total number of events and significant events per category indicated.

5. Discussions

5.1. SNRPB and SNRPN differentially stabilize transcripts despite high sequence similarity

The distinct expression patterns of SNRPB and SNRPN across tissues suggest that these paralogues may have evolved to support distinct cellular contexts, despite their high sequence similarity (>90%) (Figure 1. 4) (Saltzman, Pan, and Blencowe 2011; Thompson et al. 2018). Our results demonstrate that, when expressed in an identical cellular environment, SNRPB and SNRPN exhibit differential effects on gene expression, stabilizing distinct subsets of transcripts (Figure 4. 2. b). This divergence occurs despite their near-identical protein sequences, indicating that even small sequence variations, particularly in their RG and proline-rich motifs, or differences in interaction partners can lead to functional specialization.

We found that the introduction of ectopic SNRPB and SNRPN into HEK cells did not elevate protein levels beyond the endogenous SNRPB expression, suggesting stringent dosage control (Figure 4. 1. b). This supports the idea that precise regulation of these core splicing factors is critical for cellular function (Yan Wang et al. 2015). Following knock-out of endogenous SNRPB/B', cells expressing the transgenic paralogues displayed clear differences in transcriptome profiles. SNRPB-expressing cells largely resembled parental HEK cells, while SNRPN-expressing cells exhibited a distinct transcriptomic pattern, clustering separately from both parental and SNRPB-expressing cells (Figure 4. 2. a). Given that SNRPN replaces SNRPB in specific tissues such as the brain and hearth (Thompson et al. 2018), these findings suggest that SNRPB maintains transcriptome homeostasis, while SNRPN expression shifts the transcriptome toward a distinct state that may be optimized for specific physiological demands.

Despite their established roles in the spliceosome, our analysis revealed that SNRPB and SNRPN do not predominantly regulate alternative splicing. While initial rMATS analysis identified thousands of splicing events, most were not differentially regulated between SNRPB- and SNRPN-expressing cells (Figure 4. 2. e). A secondary analysis using VAST-Tools detected only a single event, which upon manual inspection appeared to be a false positive. Intron retention analysis using IRFinder identified a small number of differential events (Supplementary Table 8. 1), but these were mostly artifacts except for a single case in the *ITPKC* gene (Figure 4. 2. f). This suggests that, rather than promoting specific alternative splicing events, SNRPB and SNRPN influence global splicing efficiency in a manner that differentially affects transcript stability.

5.2. SNRPN expression promotes a metabolically active, growth-favoring cellular state

Functional enrichment analysis further underscored the divergent effects of these paralogues on gene regulation. SNRPB-stabilized transcripts were enriched in pathways related to cellular adhesion and surface signaling, including ECM-receptor interactions and adherens junctions (Figure 4. 3. a, b). In contrast, SNRPN-stabilized transcripts were associated with metabolic processes such as cysteine, pyruvate and glycolysis metabolism. The stabilization of numerous mitochondrial ribosomal proteins in SNRPN-expressing cells, as well as the overall higher expression of metabolic genes (Figure 4. 3. c), suggests a potential role for SNRPN in modulating cellular metabolism. This enrichment may reflect the ability of SNRPN to enhance splicing efficiency of transcripts encoding metabolic enzymes, potentially meeting the high energy demand of the brain, where SNRPN is expressed, and supporting the reliance of neural tissue on tightly regulated energy metabolic processes (Chausse et al. 2024; Rae et al. 2024).

Moreover, this difference in transcript profiles was reflected at the cellular level, with SNRPN-expressing cells proliferating significantly faster than SNRPB-expressing cells (Figure 4. 3. d). The connection between mitochondrial ribosomal proteins and cell proliferation raises the possibility that SNRPN contributes to a cellular state favoring growth, while SNRPB supports a more homeostatic transcriptional program. Mitochondrial ribosomal proteins (MRPs), which are encoded in the nucleus, translated in the cytosol and imported into the mitochondria, are essential components of the mitochondrial translation machinery. Once inside the mitochondrial matrix, mitochondrial ribosomal proteins, both the large (MRPL) and the small subunits (MRPS), form mitochondrial ribosome complex together with 16S rRNA, 12S rRNA, and other mitochondrial ribosomal components – a complex required for the translation of mitochondria-encoded electron transport chain components (Cheong et al. 2020). As energy production via oxidative phosphorylation is tightly linked to mitochondrial function, the increased stabilization of mitochondrial ribosomal transcripts in SNRPN-expressing cells may enhance mitochondrial translation capacity and, in turn, support elevated metabolic output. This may be particularly important under conditions of highly energetic demand, such as cell proliferation, where mitochondrial biogenesis and fusion are known to be upregulated to meet increased ATP requirements (Cheong et al. 2020). The enrichment of mitochondrial ribosomal components and metabolic enzymes therefore points to a SNRPN-driven cellular state optimized for growth, in contrast to the more homeostatic program maintained by SNRPB.

Taken together, our findings indicate that SNRPB and SNRPN are not only redundant splicing factors but have evolved distinct functional roles. Rather than driving alternative splicing, these paralogues appear to differentially regulate the stability of specific transcript classes, which in turn affects cellular phenotype. Their functional divergence may result from differences in protein-protein interactions and posttranslational modification states.

5.3. SNRPB and SNRPN paralogues differ in their arginine methylation states

The functional divergence between SNRPB and SNRPN in stabilizing distinct transcripts raises interesting questions about how two paralogues, which encode almost identical proteins with >90% sequence similarity and the same domain architecture, can achieve this (Figure 1. 4). Our findings reveal that arginine methylation is a key factor underlying their functional divergence, with SNRPN exhibiting stronger associations with components of the methylosome complex, including PRMT5 and its adaptors CLNS1A (pICln), RIOK1, and WDR77 (Figure 4. 5. g). These interactions likely enhance the capacity of SNRPN for arginine methylation, distinguishing it from SNRPB at the posttranslational level. The substrate specificity of PRMT5 is regulated by adaptor proteins, which recruit specific substrates to the methylosome. For example, CLNS1A (pICln) facilitates the methylation of spliceosome subunits (SNRPB/B', SNRPD1, and SNRPD2) and ribosomal proteins (LSM4, LSM10, and LSM11), enabling PRMT5 to regulate splicing activity and RNA processing (Mulvaney et al. 2021). Similarly, RIOK1 recruits nucleolin and ribosomal protein RPS10 to the PRMT5 complex, contributing to ribosome biogenesis (Mulvaney et al. 2021). WDR77 (MEP50) further enhances the enzymatic activity of PRMT5 by promoting symmetric dimethylation of arginine residues on diverse substrates, including histone tails and splicing factors (Krzyzanowski et al. 2022). Together, these adaptors likely modulate the differential methylation patterns observed between SNRPB and SNRPN, particularly within the proline-rich region.

In contrast, SNRPB exhibited fewer interactions with components of the methylosome complex, suggesting that it may rely less on arginine methylation for its function. Instead, SNRPB showed stronger associations with other interaction partners, such as APOBEC3B, TOP3A, and KMT2D (Figure 4. 5. g). APOBEC3B is a member of the AID/APOBEC family of cytosine deaminases, which catalyze the deamination of cytosine to uracil in single stranded DNA (Pecori et al. 2022). While primarily implicated in intrinsic antiviral responses and cancer mutagenesis (Caswell et al. 2024), its interaction with SNRPB suggests a potential role in RNA editing or other RNA-related processes. Additionally, SNRPB interacts with TOP3A, a type I topoisomerase that alters DNA topology by creating temporary single-strand breaks to relieve supercoiling stress and resolve DNA interlinkages (Erdinc et al. 2023). In the nucleus, TOP3A forms part of the BTRR complex, which resolves recombination intermediates during DNA repair and facilitates sister chromatid decatenation during mitosis. The interaction of SNRPB with TOP3A may reflect its involvement in coordinating transcriptional and replicative processes with RNA splicing. Furthermore, the association of SNRPB with KMT2D, a lysine methyltransferase that catalyzes H3K4 methylation to promote open chromatin and activate target genes (J. Wu et al. 2024), suggests role in coupling splicing regulation with chromatin

dynamics and transcriptional activation. Collectively, these interactions imply that SNRPB operates within a broader functional context, potentially integrating RNA metabolism with chromatin remodeling and genome stability.

Our mass spectroscopy analysis revealed several Arginine residues that were methylated exclusively in SNRPN. For example, monomethylation on Arg196 and Arg209, as well as dimethylation on Arg209, were detected only in SNRPN (Figure 4. 6). Additionally, arginine residues unique to SNRPN (Arg236 and Arg239) were also found to be methylated. These modifications likely alter the structural conformation or binding affinity of SNRPN, potentially influencing its interactions with other splicing factors or target transcripts. In contrast, SNRPB exhibited fewer methylation events, consistent with its weaker association with the methylosome. This difference in methylation status may explain why SNRPB stabilizes transcripts associated with cellular surface functions, while SNRPN stabilizes transcripts linked to metabolic pathways.

5.4. Translation-dependent Arginine methylation distinguishes SNRPN from its paralogue SNRPB

Our findings identify a previously unrecognized behavior of SRNPN in response to translational inhibition, distinguishing it from its paralogue SNRPB, in an Arginine methylation-dependent manner. Using the 12F5 antibody as a readout, we demonstrate that inhibition of translation alters the PTM landscape of SRNPN in a manner not observed for SNRPB, despite their high sequence similarity and shared domain architecture. This selective response points toward a tightly regulated and context-dependent modification mechanism that may reflect divergent biological roles of the two proteins.

Initial antibody screening revealed that 12F5 detects C-terminal fragments of both SNRPB and SNRPN (Figure 4. 7. a, b), but fails to recognize the 1-190 fragment. While the exact residues forming the 12F5 epitope remain unidentified, we have enough evidence supporting its sensitivity to Arginine methylation. Chemical inhibition of PRMTs led to a strong decrease in 12F5 signal for SNRPN but not for SNRPB, even though HA-tag levels remained constant (Figure 4. 7. c). The signal loss was reversed in a mutant where all six Arginine residues in the proline-rich region were substituted with Lysine residues (R6K), leading to marked increase in detection (Figure 4. 7. e). These observations suggest that the 12F5 epitope is sensitive to Arginine methylation status, and SNRPN is uniquely regulated in this context.

The differential sensitivity of SNRPB and SNRPN to translation inhibitors, cycloheximide (CHX) and puromycin, underscores the link between active translation and the regulation of SNRPN's PTM state (Figure 4. 7. f, g). Both inhibitors disrupt distinct steps of protein synthesis – CHX

by stalling ribosomes during elongation, and puromycin by triggering premature termination (Schneider-Poetsch et al. 2010; Enam et al. 2020; Aviner 2020). Despite these mechanistic differences, both treatments led to a marked reduction in SNRPN detection by the 12F5 antibody, without affecting the overall protein levels, as confirmed by HA-tag and flow cytometry (Figure 4. 7. c, Figure 4. 8. e). This suggests that ongoing translation is required to maintain the Arg-methylation state of SNRPN, or alternatively, that translation inhibition actively promotes demethylation or conformational changes in the proline-rich region. Importantly, these effects were not observed for the SNRPB, highlighting a unique and selective regulatory mechanism for SNRPN.

A similar reduction in SNRPN signal was observed with Actinomycin D, a transcription inhibitor that intercalates into DNA and forms a stable complex, thereby blocking RNA polymerase progression (Ratnadiwakara and Änkö 2018). This suggests a potential coupling between transcription and translation in maintaining the methylation state of SNRPN (Figure 4. 7. g). In contrast, treatment with Pladienolide B (PlaB), a natural macrolide that inhibits splicing by binding to SF3b subcomplex of the spliceosome and inducing accumulation of unspliced pre-mRNAs (Yokoi et al. 2011), did not reduce the 12F5 signal. Instead, PlaB treatment resulted in increased overall levels of both SNRPB and SNRPN proteins (Figure 4. 7. i). These findings argue against a direct role for productive splicing in regulating the observed PTM dynamics, and suggest that translational activity more specifically influences the Arg-methylation status of SNRPN.

5.5. Mechanistic insights into the regulation of SNRPN by translation and Arginine methylation

Interestingly, SNRPN was unaffected by inhibition of NMD via SMG1 inhibitor (Nasif et al. 2023), despite global stabilization of canonical NMD targets (Sato and Singer 2021), suggesting that CHX-induced changes are not a consequence of altered NMD activity. This was further supported by the lack of rescue effect when PlaB was co-administered with CHX (Figure 4. 8. c), demonstrating that CHX-mediated PTM regulation is not dependent on newly spliced transcripts. Furthermore, flow cytometry and western blotting using a methylation-insensitive SNRPB antibody confirmed that the CHX-induced reduction in 12F5 signal is not due to general protein destabilization (Figure 4. 8. d, e), and we obtained the same result using a different protein extraction method (Figure 4. 8. f), which shows that the effect is not just due to a technical issue.

Mass spectrometry revealed that the methylation-sensitive region lies within the proline-rich C-terminus, downstream of residue 190, with multiple Arg-monomethylation sites dropping to undetectable levels after CHX treatment (Figure 4. 10, a). This region is absent from the

conserved RG domain, which remained unchanged (Figure 4. 10, b). To our knowledge, this is the first demonstration of translation-dependent Arginine methylation within the proline-rich region of SNRPN, distinguishing it from its paralogue SNRPB and pointing to a previously unrecognized layer of posttranslational control.

The unique behavior of SNRPN was further dissected through targeted mutagenesis. Mutation of the six Arginine residues (R196, R209, R221, R228, R236, R239) in the proline-rich region abolished the response to CHX (Figure 4. 11. a), establishing these sites as required for dynamic PTM changes. Notably, mutation of four Arginine residues (R196, R221, R228, R236) was sufficient to make SNRPN resistant, while combinations lacking these residues retained partial sensitivity (Figure 4. 11. a). This suggests a threshold or cumulative mechanism where multiple Arginine residues contribute to epitope integrity or modification.

The role of the C-terminal extension, which differs between SNRPB and SNRPN, was explored through swapping experiment. Importantly, replacing the C-terminus of SNRPN with that of SNRPB did not impair CHX sensitivity (Figure 4. 11. b), while the reciprocal swap caused sensitivity to SNRPB, indicating that the proline-rich region together with the extended C-terminus are necessary and sufficient for this regulatory axis. While R236 and R239 are unique to SNRPN, they are not solely responsible for the phenotype, pointing toward a distributed contribution of multiple residues. This supports the idea that evolutionary differences in the C-terminal region of SNRPN may have allowed it to acquire a specialized regulatory function in response to translational signals, diverging from the behavior of SNRPB despite their overall similarity.

The functional implications of translation-regulated Arginine methylation remain to be explained. Arginine methylation is known to affect protein-protein interactions, subcellular localization, and RNA binding capacity (Zakrzewicz et al. 2012; Al-Hamashi, Diaz, and Huang 2020), and such dynamic modulation may enable SNRPN to act as a sensor or effector in response to changes in translational activity. In this context, SNRPN may integrate translational cues to modulate its interactions with specific binding partners or adapt its role within the spliceosomal machinery. This layer of regulation could be particularly relevant under conditions of cellular stress or altered metabolic states, where translation is reprogrammed and posttranslational mechanisms rapidly reshape functional networks without changes in protein abundance. The fact that SNRPB, despite its high sequence similarity, does not show comparable sensitivity highlights a functional divergence between the paralogues. Given that SNRPB and SNRPN arose from a gene duplication event, their differential regulation through PTM such as Arginine methylation might reflect subfunctionalization or neofunctionalization. In this case, extended C-terminal tail and unique Arginine residues of SNRPN could have been

selectively retained to facilitate dynamic regulation by translational activity – an adaptation not required for the ubiquitously expressed SNRPB.

5.6. Translation inhibition triggers SNRPN-specific nuclear changes

Our microscopy and interaction profiling show that SNRPN undergoes a CHX-sensitive change in the nucleus, which affects its behavior and binding partners. Both SNRPB and SNRPN were mainly nuclear under normal conditions (-CHX) (Figure 4. 12. a, b). After CHX treatment, the nuclear 12F5 signal was completely lost for SNRPN, while it remained stable for SNRPB (Figure 4. 12. c). At the same time, the mNeon signal remained unaffected in the nucleus. This shows that the SNRPN-specific epitope loss happens inside the nucleus and is not simply a result of changes in the cytoplasm. It also shows that SNRPB is protected from this change.

Cajal bodies remained detectable after CHX treatment and continued to co-localize with SNRPB and SNRPN, consistent with the stable nuclear retention of both paralogues (Figure 4. 13. a). However, the number of Coilin foci per cell significantly decreased after CHX treatment, as did the number of SNRPB/N-positive foci (Figure 4. 13. b, c). This suggests that although the general localization to Cajal bodies is maintained, translation inhibition leads to a remodeling of these nuclear structures, reducing their number.

The FRAP experiments further support this idea. Under control conditions (-CHX), both paralogues showed similar recovery dynamics (Figure 4. 14). However, after CHX treatment, SNRPN recovery became slower, while SNRPB remained the same. This suggests that after translation inhibition, SNRPN changes its interactions or posttranslational status in the nucleus.

When we looked at the binding partners of SNRPB and SNRPN, we found that most interactions with core complexes like the spliceosome and the methylosome stayed stable (Figure 4. 15. a). However, some nuclear proteins showed changes after CHX treatment, and some changes were specific to SNRPN (Figure 4. 16. a). SNRPN gained new interactions with stress-related and DNA damage-associated proteins like PHIP, ZNF280C, and H2AX (Figure 4. 16. a). At the same time, it lost interactions with chromatin-associated proteins like CENPH and ZBTB33. This suggests that SNRPN switches its partners inside the nucleus after translation inhibition, moving away from chromatin factors toward stress-related proteins.

The proteins that changed binding were not strongly connected to each other by standard pathway analysis (Figure 4. 16. c). This suggests that the changes affect individual proteins rather than big complexes. However, we found that many of the proteins that bind to SNRPB and SNRPN were rich in monomethyl-Arginine sites (Figure 4. 16. d), meaning that SNRPB and SNRPN and their partners form a “MMA hub” inside the nucleus. Since the SNRPN-

specific loss of the 12F5 signal happens together with a loss of Arginine methylation, it is likely that these nuclear changes depend on the methylation state of SNRPN.

Our findings suggest a model where SNRPN-specific methylation patterns control how it interacts with other proteins in the nucleus, especially after translation is blocked. This could happen through loss of methyl groups, changes in protein binding, or changes in SNRPN structure. It would be interesting to test whether similar effects happen under natural stress conditions like arginine or glucose starvation (Hsu et al. 2021; Lin et al. 2024).

In summary, SNRPN-specific loss of the 12F5 epitope after CHX treatment reflects a nuclear event involving selective changes in protein interactions. This adds a new layer of difference between SNRPB/N paralogues and shows that translation-related signals can shape nuclear protein networks through regulation of methylation.

5.7. Metabolic and developmental regulation of 12F5 epitope accessibility in SNRPB/N

Our data demonstrates that the expression and epitope accessibility of SNRPB paralogues vary across cellular and metabolic contexts. Using the combination of a polyclonal SNRPB (PTM-insensitive) and the monoclonal 12F5 (SmB/B'/N) antibody, which differentially detects SNRPB and SNRPN depending on modification status, we observed tissue- and cell type-specific patterns.

As expected, SNRPN was readily detected in mouse brain lysates using the polyclonal antibody, but the 12F5 monoclonal failed to recognize it (Figure 4. 17. a). This supports the hypothesis that posttranslational modifications hinder 12F5 binding in native tissue settings. Notably, this behavior extended to cultured cells with endogenous SNRPN expression. For instance, human induced pluripotent stem cells (hiPSCs), which exhibit robust SNRPN expression confirmed by RNA-seq and ribosome profiling (Figure 4. 17. c) (Tomuro et al. 2024; Rohm et al. 2025), displayed only weak 12F5 signal, while SNRPB detection was unaffected (Figure 4. 17. a). This low detection of SNRPN by 12F5 in hiPSCs was not due to lack of expression as transcriptomics and proteomics. Interestingly, hiPSCs do not express the splice isoform SNRPB', unlike HEK cells which endogenously express both SNRPB and SNRPB' (Figure 4. 17. b), making it possible to compare SNRPB and SNRPN without SNRPB'.

Cycloheximide treatment abolished the already faint 12F5 signal for SNRPN in hiPSCs, revealing its sensitivity to posttranslational modifications (Figure 4. 17. d). A similar phenotype was seen in hiPSC-derived neurons, which also express high levels of SNRPN. In these cells, 12F5 detection was faint at baseline and completely lost upon CHX treatment (Figure 4. 17. e), consistent with a dynamic, modification-dependent epitope.

To test whether this epitope sensitivity was unique to pluripotent and neuronal contexts or reflected a broader regulatory mechanism, we next examined SNRPN detection in F9 embryonal carcinoma cells – another developmentally relevant model. Surprisingly, we detected no SNRPN in F9 cells (Figure 4. 17. f), contrary to earlier reports claiming that undifferentiated F9 cells express both SNRPB and SNRPN at a 46:54 ratio, respectively (Sharpe, Williams, and Latchman 1990). These discrepancies may arise from differences in F9 sublineage, culture conditions, or the developmental stage of the cells at the time of analysis. The original study also reported rapid downregulation of SNRPN during differentiation (Sharpe, Williams, and Latchman 1990), suggesting that our F9 cells may have been partially or fully differentiated upon arrival.

Interestingly, we found that 12F5 strongly detected a CHX-sensitive band corresponding to SNRPB' in chicken cells, further supporting the idea that 12F5 binding is modulated by modification status (Figure 4. 17. g). Chicken express only the longer isoform SNRPB' that shows high similarity to human SNRPB' protein, and notably do not express SNRPN (Turner et al. 2023). This provides a clean model in which 12F5 reactivity is solely attributable to SNRPB' and not confounded by the presence of SNRPN. Given that SNRPB' and SNRPN share 93% sequence identity (Turner et al. 2023), the CHX-sensitive nature of the epitope in both chicken SNRPB' and human SNRPN strongly supports a shared posttranslational feature driving antibody accessibility. This observation reinforces the hypothesis that modification-sensitive epitopes may regulate or reflect paralogue-specific functions in development and disease.

5.8. Arginine methylation and potentially citrullination modulate the 12F5 epitope in response to nutrient and stress signaling

To understand the upstream factors that may regulate this epitope accessibility, we hypothesized that nutrient availability and metabolic signaling – especially via mTOR – might play a role. Our reasoning stemmed from observed differences in SNRPN behavior across media types: HEK cells cultured in high Glucose, high Glutamine DMEM showed robust SNRPN expression but stable 12F5 detection, whereas hiPSCs and hiPSC-derived neurons cultured in more defined media (E8 and BrainPhys, respectively) exhibited weaker 12F5 signals despite confirmed SNRPN expression (Figure 4. 18. a). A notable distinction was the Arginine concentration – highest in E8, and lowest in DMEM – suggesting that extracellular Arginine availability may modulate SNRPN recognition. Experimentally, Arginine depletion recapitulated CHX effect, abolishing the 12F5 band for SNRPN while keeping SNRPB detection stable (Figure 4. 18. b), consistent with a model in which translation and Arginine availability jointly modulate epitope accessibility.

These findings point to a modification landscape governed by nutrient signaling, particularly via mTOR. Arginine is a key activator of mTORC1 - one of the mTOR complexes - (C.-L. Chen et al. 2021). PRMT5 is functionally downstream of mTOR signaling, and PRMT5-mediated methylation is critical for AKT1 phosphorylation (L. Huang et al. 2022), linking Arginine metabolism to broader PTM crosstalk. However, our previous data shows that 12F5 robustly detects both SNRPB and SNRPN when expressed in *E.coli* and *Sf9* insect cells (Supplementary Figure 9. 1). Since *E.coli* lacks machinery for Arginine methylation, this confirms that the presence of unmethylated Arginine residues is sufficient for 12F5 binding. Thus, while Arginine methylation modulates epitope accessibility, its absence does not inherently prevent 12F5 binding. An additional layer of modification is likely to contribute. One candidate is citrullination, a posttranslational modification in which Arginine is converted to Citrulline by Peptidylarginine deiminases (PADs) (Rebak et al. 2024). Citrullination alters the charge and hydrogen bonding potential of the Arginine side chain (Rebak et al. 2024), potentially disrupting epitope recognition by 12F5. Although SNRPN contains one experimentally validated citrullination site at R49 (Rebak et al. 2024), our data localize the 12F5 epitope to the C-terminal region between amino acids 190 and 231 (Figure 4. 7. a), excluding R49 as a direct contributor to epitope masking. Therefore, the hypothesis that epitope accessibility is modulated by citrullination must involve other, unannotated Arginine residues within this C-terminal region.

PADs preferentially act on unmodified Arginine residues, and monomethylated Arginine is a significantly poorer substrate for these enzymes. This substrate selectivity suggests that methylation can act as a protective modification that prevents citrullination, reinforcing the concept that PADs and PRMTs are biochemically antagonistic (Xu and Richard 2021). In this respect, the dynamic between methylation and citrullination may reflect a competitive regulatory mechanism, rather than two independent PTMs.

We next asked whether cellular metabolic state influences these modifications. In our experiments, hypoxia sensitized SNRPB to CHX treatment, mimicking the behavior of SNRPN under stress conditions (Figure 4. 18. c). This suggests that SNRPB, normally insensitive to CHX, acquires a modification under hypoxia that reduces 12F5 detection. One interpretation is that hypoxia alters Arginine metabolism or modulates PAD activity, enabling citrullination of Arginine residues within 12F5 epitope. In line with this, studies in cancer models have shown that PAD enzymes work in a calcium-dependent manner (Rebak et al. 2024; Zhu et al. 2022) and PAD activity is induced in tumor environments due to redox stress or nutrient unavailability (Zhu et al. 2022). Furthermore, mTOR signaling, which integrates nutrient and oxygen availability, is a known regulator of PRMT5 activity and Arginine utilization (L. Huang et al.

2022). Under mTOR inhibition or hypoxia, the balance between methylation and citrullination may shift toward PAD-mediated modification.

Taken together, our findings point to a model in which the 12F5 epitope is dynamically regulated by competing Arginine modifications, likely methylation and citrullination, in response to metabolic signals. These modifications modulate paralogue-specific detection and potentially function. Importantly, the PTM sensitivity of the epitope makes 12F5 not just a detection reagent, but a molecular readout of the metabolic and signaling state of the cell.

5.9. Differential transcriptome responses reveal paralogue-specific adaptation to translation inhibition

Our RNA seq analysis revealed that SNRPB and SNRPN cells respond to translation inhibition by cycloheximide (CHX) with distinct transcriptomic profiles, supporting the notion that these paralogues differentially regulate gene expression in stress conditions (Figure 4. 19. a). Although both cell types exhibited widespread transcriptional changes, the magnitude and specificity of these changes were more pronounced in SNRPN cells, as reflected by a higher number of CHX-responsive genes (Figure 4. 19. b). These differences cannot be explained solely by previously defined “stable” SNRPB/N targets, which showed no uniform trend under CHX (Figure 4. 19. d), suggesting that CHX triggers additional layers of regulation beyond baseline transcript stability.

Interestingly, while a substantial core response to CHX was shared between SNRPB and SNRPN cells, SNRPN cells exhibited a significantly broader repertoire of unique gene regulation events (Figure 4. 19. c). Functional enrichment analysis implicated SNRPN-specific gene regulation in nutrient metabolism pathways, including D-Glutamine and D-Glutamate metabolism, Arginine/Proline metabolism as well as Ubiquitin-mediated proteolysis (Figure 4. 19. e). These results raise the possibility that SNRPN is more tightly linked to nutrient-sensing and metabolic adaptation pathways than its paralogue, potentially reflecting its restricted expression in the brain, which are known for their high metabolic demands (Chausse et al. 2024; Rae et al. 2024).

In contrast, fewer unique gene expression changes were observed in SNRPB cells, and the associated pathways – such as sulfur and selenium metabolism – showed relatively lower statistical significance (Figure 4. 19. f). These findings align with our previous observation that SNPRB-expressing cells are less responsive to nutrient perturbations in terms of 12F5 epitope modulation (Figure 4. 18. b).

5.10. SNRPN stabilizes complex transcripts under translation inhibition and promotes efficient splicing

A striking difference between the two paralogues emerged when analyzing gene architecture. In SNRPN cells, CHX-upregulated genes were longer and carried more intronic content, including very long introns (Figure 4. 20. a). In contrast, SNRPB cells showed preferential downregulation of long-intron-containing genes. These observations suggest that SNRPN may better support the efficient splicing and stabilization of complex transcripts under conditions of impaired translation. Indeed, in SNRPN cells, CHX treatment led to stabilization of a disproportionately high number of transcripts with 16 or more introns (Figure 4. 20. b). This may reflect differences in posttranslational regulation of SNRPN, as suggested by its distinct Arginine methylation profile and CHX-dependent interaction changes.

Despite the extensive gene expression changes, CHX treatment led to a marked reduction in alternative splicing (Figure 4. 20. d). This effect was seen across most types of events – alternative splice site usage, mixed events, and intron retention – but less so for exon skipping. While this shift toward constitutive splicing could reflect a general response to stress or reduced translation, our manual inspection revealed that most differential splicing events were not paralogue-specific and may instead represent a global response to CHX (Figure 4. 20. c). Supporting this, independent splicing analysis using IRFinder and VAST-tools identified very few robust events distinguishing SNRPB from SNRPN cells.

Taken together, these results suggest that, in the context of translation inhibition, the main role of SNRPB/N is not to regulate splicing diversity, but rather to modulate splicing efficiency – especially for long and complex transcripts. This effect is more prominent in SNRPN cells, consistent with our previous findings of higher posttranslational responsiveness and altered epitope accessibility in SNRPN compared to SNRPB. These findings point to a paralogue-specific mechanism for coping with metabolic or nutrient stress, where SNRPN enables the stabilization and processing of transcripts that are otherwise susceptible to degradation.

6. Conclusions and future perspectives

This study demonstrates that, although *SNRPB* and *SNRPN* are paralogues with near-identical primary sequences and they share canonical functions in spliceosome biology, SNRPB and SNRPN diverge meaningfully in their posttranslational regulation, interaction profiles, and transcript stabilization functions. We show that these paralogues respond differently to translational inhibition, with SNRPN – but not SNRPB – losing recognition by an SmB/B'/N antibody (12F5) in a context dependent on translation inhibitor. This change is accompanied by a reduction in Arginine methylation levels, suggesting a strong link between translational activity and the posttranslational modification landscape of SNRPN. These results point toward a tightly regulated and perhaps co-translationally modified state of SNRPN that governs its interaction potential and visibility to antibodies.

Mutagenesis experiments further highlight the complexity of this regulation. Replacing six Arginine (R) residues with Lysine (K) residues eliminated the CHX-sensitive phenotype, but only certain combinations of mutations were effective. In all cases where the phenotype was lost, R228 was among the mutated residues, while combinations lacking R228 retained sensitivity. This points to a key role for R228 in modulating posttranslational behavior of SNRPN. Interestingly, we did not detect methylation at R228 in our mass spectrometry, raising the possibility that it is citrullinated – a modification that would prevent methylation and could influence antibody recognition. To test this directly, we are generating an R228K mutant to see whether blocking citrullination or mimicking the unmethylated state affects the CHX response. Additional mutants, such as replacing six Arginine residues with Glutamine (Q) residues or only R228 (R228Q), could also be informative. Since Glutamine mimics the size and charge-neutrality of citrulline, such mutants can serve as functional proxies to test whether citrullination, rather than methylation, underlies the observed phenotype.

The possibility that citrullination competes with methylation adds an additional regulatory layer. Since these modifications are mutually exclusive on the same Arginine, one could block the other. Inhibiting PAD enzymes, which catalyze citrullination, is our next step. If PAD inhibition restores antibody recognition of SNRPN after CHX treatment, it would support a model in which translation-dependent demethylation is followed by citrullination, leading to epitope loss. These studies could be complemented by PAD overexpression or knockdown to identify the responsible enzyme, and in vitro assays using purified proteins to test direct modification.

Our results also revealed that SNRPN preferentially stabilizes transcripts related to metabolic processes, whereas SNRPB supports expression of genes involved in signaling and cytoskeletal dynamics. This observation suggests that these proteins are not only biochemically distinct but are also functionally specialized. To explore the biological consequences of this transcript selectivity, comparative metabolomics in SNRPB- versus

SNRPN-expressing cells would be informative. Identifying whether transcript-level changes translate into measurable shifts in cellular metabolism could clarify a regulatory role of SNRPN at the interface of splicing and metabolic adaptation.

Since modifications of SNRPN appear responsive to the metabolic state of the cell, it is plausible that nutrient availability influences its regulatory behavior. Experiments involving Glucose deprivation or Lysine deprivation could test whether metabolic stress further alters its modification status or transcript-stabilizing functions. Such work may identify SNRPN as a link between translation, metabolism, and RNA regulation.

Given the observed link to translation, it may be useful to test whether SNRPN transiently associates with the ribosome or modifying enzymes during protein synthesis. Proximity labeling could capture weak or dynamic interactions that are missed by standard proteomics, helping clarify when and where SNRPN is modified.

Finally, the absence of strong growth phenotypes in overexpression or depletion studies raises the question of subtle or context-dependent functional impacts. Competitive growth assays under stress conditions or differential cues could help reveal underappreciated roles of SNRPN in maintaining cellular homeostasis or adapting to environmental changes. These assays may be especially powerful in neuronal models, where SNRPN is naturally enriched and where energy-demanding processes intersect with high RNA complexity. While our study has extended beyond ectopic expression systems by including iPSCs, iPSC-derived neurons, and CHX-injected mouse brain tissue to better reflect endogenous contexts, further in vivo validation will be important. For example, once a citrullination-dependent regulatory mechanism is confirmed under cell culture conditions, intracerebroventricular injection of PAD inhibitors in mice could help determine whether citrullination directly modulates SNRPN epitope accessibility, location, or function in the brain. Such approaches would deepen our understanding of the physiological relevance of posttranslational modifications in modulating SNRPN biology, particularly in the nervous system.

In conclusion, this work identifies SNRPN as a context-sensitive regulator whose function is shaped by translational and metabolic input. Its divergence from SNRPB appears to be driven not by major differences in sequence or expression level, but by subtle, condition-dependent post-translational modifications. Elucidating these regulatory mechanisms is particularly relevant given the involvement of SNRPN in neurodevelopmental disorder Prader-Willi syndrome, where impaired splicing efficiency or reduced stabilization of complex transcripts may contribute to disease pathology. More broadly, this study illustrates how gene duplicates can acquire distinct, stress-responsive regulatory features, despite high sequence conservation. These findings offer a conceptual framework for understanding how environmental cues influence protein function at the posttranslational level. Future research

integrating targeted mutagenesis, metabolic manipulation, citrullination pathway analysis, and advanced proteomics will be essential in fully defining the physiological relevance and potential pathological implications of SNRPN specialization.

7. References

Achilleos, Annita, and Paul A. Trainor. 2012. “Neural Crest Stem Cells: Discovery, Properties and Potential for Therapy.” *Cell Research* 22 (2): 288–304.

Acuña, Myriah L., Andrea García-Morin, Rebeca Orozco-Sepúlveda, Carlos Ontiveros, Alejandra Flores, Arely V. Diaz, Isabel Gutiérrez-Zubiate, et al. 2023. “Alternative Splicing of the SUMO1/2/3 Transcripts Affects Cellular SUMOylation and Produces Functionally Distinct SUMO Protein Isoforms.” *Scientific Reports* 13 (1): 2309.

Al-Hamashi, Ayad A., Krystal Diaz, and Rong Huang. 2020. “Non-Histone Arginine Methylation by Protein Arginine Methyltransferases.” *Current Protein & Peptide Science* 21 (7): 699–712.

Anczuków, Olga, Avi Z. Rosenberg, Martin Akerman, Shipra Das, Lixing Zhan, Rotem Karni, Senthil K. Muthuswamy, and Adrian R. Krainer. 2012. “The Splicing Factor SRSF1 Regulates Apoptosis and Proliferation to Promote Mammary Epithelial Cell Transformation.” *Nature Structural & Molecular Biology* 19 (2): 220–28.

Angelopoulou, Efthalia, Efstratios-Stylianos Pyrgelis, Chetana Ahire, Prachi Suman, Awanish Mishra, and Christina Piperi. 2023. “Functional Implications of Protein Arginine Methyltransferases (PRMTs) in Neurodegenerative Diseases.” *Biology* 12 (9). https://doi.org/10.3390/biology12091257.

Aslam, Akhmed, Saloni Mittal, Frederic Koch, Jean-Christophe Andrau, and G. Sebastiaan Winkler. 2009. “The Ccr4-NOT Deadenylase Subunits CNOT7 and CNOT8 Have Overlapping Roles and Modulate Cell Proliferation.” *Molecular Biology of the Cell* 20 (17): 3840–50.

Auwerx, Chiara, Maarja Jõeloo, Marie C. Sadler, Nicolò Tesio, Sven Ojavee, Charlie J. Clark, Reedik Mägi, Estonian Biobank Research Team, Alexandre Reymond, and Zoltán Kutalik. 2024. “Rare Copy-Number Variants as Modulators of Common Disease Susceptibility.” *Genome Medicine* 16 (1): 5.

Aviner, Ranen. 2020. “The Science of Puromycin: From Studies of Ribosome Function to Applications in Biotechnology.” *Computational and Structural Biotechnology Journal* 18 (April): 1074–83.

Azhar, Muhammad, Caoling Xu, Xue Jiang, Wenqing Li, Yuzhu Cao, Xiaoli Zhu, Xuemei Xing, et al. 2023. “The Arginine Methyltransferase Prmt1 Coordinates the Germline Arginine Methylome Essential for Spermatogonial Homeostasis and Male Fertility.” *Nucleic Acids Research* 51 (19): 10428–50.

Babic, Ivan, Andrew Jakymiw, and Donald J. Fujita. 2004. “The RNA Binding Protein Sam68 Is Acetylated in Tumor Cell Lines, and Its Acetylation Correlates with Enhanced RNA Binding Activity.” *Oncogene* 23 (21): 3781–89.

Bacrot, Séverine, Mathilde Doyard, Céline Huber, Olivier Alibeu, Niklas Feldhahn, Daphné Lehalle, Didier Lacombe, et al. 2015. “Mutations in SNRPB, Encoding Components of the Core Splicing Machinery, Cause Cerebro-Costo-Mandibular Syndrome.” *Human Mutation* 36 (2): 187–90.

Bai, Rui, Ruixue Wan, Lin Wang, Kui Xu, Qiangfeng Zhang, Jianlin Lei, and Yigong Shi. 2021. “Structure of the Activated Human Minor Spliceosome.” *Science (New York, N.Y.)* 371 (6535): eabg0879.

Basilicata, M. Felicia, and Claudia Isabelle Keller Valsecchi. 2021. “The Good, the Bad, and the Ugly: Evolutionary and Pathological Aspects of Gene Dosage Alterations.” *PLoS Genetics* 17 (12): e1009906.

Bedford, Mark T., and Steven G. Clarke. 2009. “Protein Arginine Methylation in Mammals: Who, What, and Why.” *Molecular Cell* 33 (1): 1–13.

Beers, Joyce J. B. C. van, and Marco W. J. Schreurs. 2022. “Anti-Sm Antibodies in the Classification Criteria of Systemic Lupus Erythematosus.” *Journal of Translational Autoimmunity* 5 (April): 100155.

Benjamini, Yoav, and Yosef Hochberg. 1995. “Controlling the False Discovery Rate: A Practical and Powerful Approach to Multiple Testing.” *Journal of the Royal Statistical Society. Series B, Statistical Methodology* 57 (1): 289–300.

Bergthorsson, Ulfar, Dan I. Andersson, and John R. Roth. 2007. “Ohno’s Dilemma: Evolution of New Genes under Continuous Selection.” *Proceedings of the National Academy of Sciences of the United States of America* 104 (43): 17004–9.

Biancotti, Juan-Carlos, Kavita Narwani, Nicole Buehler, Berhan Mandefro, Tamar Golan-Lev, Ofra Yanuka, Amander Clark, David Hill, Nissim Benvenisty, and Neta Lavon. 2010. “Human Embryonic Stem Cells as Models for Aneuploid Chromosomal Syndromes.” *Stem Cells (Dayton, Ohio)* 28 (9): 1530–40.

Biswas, Subhankar, and C. Mallikarjuna Rao. 2018. “Epigenetic Tools (The Writers, The Readers and The Erasers) and Their Implications in Cancer Therapy.” *European Journal of Pharmacology* 837 (October): 8–24.

Blanc, Roméo S., and Stéphane Richard. 2017. “Arginine Methylation: The Coming of Age.” *Molecular Cell* 65 (1): 8–24.

Boisvert, François-Michel, Carol Anne Chénard, and Stéphane Richard. 2005. “Protein Interfaces in Signaling Regulated by Arginine Methylation.” *Science’s STKE: Signal Transduction Knowledge Environment* 2005 (271): re2.

Bonner, Elizabeth A., and Stanley C. Lee. 2023. “Therapeutic Targeting of RNA Splicing in Cancer.” *Genes* 14 (7). https://doi.org/10.3390/genes14071378.

Borao, Sonia, José Ayté, and Stefan Hümmer. 2021. “Evolution of the Early Spliceosomal Complex-from Constitutive to Regulated Splicing.” *International Journal of Molecular Sciences* 22 (22): 12444.

Brahms, H., J. Raymackers, A. Union, F. de Keyser, L. Meheus, and R. Lührmann. 2000. “The C-Terminal RG Dipeptide Repeats of the Spliceosomal Sm Proteins D1 and D3 Contain Symmetrical Dimethylarginines, Which Form a Major B-Cell Epitope for Anti-Sm Autoantibodies.” *The Journal of Biological Chemistry* 275 (22): 17122–29.

Bressler, J., T. F. Tsai, M. Y. Wu, S. F. Tsai, M. A. Ramirez, D. Armstrong, and A. L. Beaudet. 2001. “The SNRPN Promoter Is Not Required for Genomic Imprinting of the Prader-Willi/Angelman Domain in Mice.” *Nature Genetics* 28 (3): 232–40.

Bryant, Jean-Paul, John Heiss, and Yeshavanth Kumar Banasavadi-Siddegowda. 2021. “Arginine Methylation in Brain Tumors: Tumor Biology and Therapeutic Strategies.” *Cells (Basel, Switzerland)* 10 (1): 124.

Caswell, Deborah R., Philippe Gui, Manasi K. Mayekar, Emily K. Law, Oriol Pich, Chris Bailey, Jesse Boumelha, et al. 2024. “The Role of APOBEC3B in Lung Tumor Evolution and Targeted Cancer Therapy Resistance.” *Nature Genetics* 56 (1): 60–73.

Chanarat, Sittinan, and Shravan Kumar Mishra. 2018. “Emerging Roles of Ubiquitin-like Proteins in Pre-MRNA Splicing.” *Trends in Biochemical Sciences* 43 (11): 896–907.

Chausse, Bruno, Nikolai Malorny, Andrea Lewen, Gernot Poschet, Nikolaus Berndt, and Oliver Kann. 2024. “Metabolic Flexibility Ensures Proper Neuronal Network Function in Moderate Neuroinflammation.” *Scientific Reports* 14 (1): 14405.

Checchi, Paula M., and Joanne Engebrecht. 2011. “Heteromorphic Sex Chromosomes: Navigating Meiosis without a Homologous Partner.” *Molecular Reproduction and Development* 78 (9): 623–32.

Chen, Chia-Lin, Sheng-Chieh Hsu, Tan-Ya Chung, Cheng-Ying Chu, Hung-Jung Wang, Pei-Wen Hsiao, Shauh-Der Yeh, David K. Ann, Yun Yen, and Hsing-Jien Kung. 2021. “Arginine Is an Epigenetic Regulator Targeting TEAD4 to Modulate OXPHOS in Prostate Cancer Cells.” *Nature Communications* 12 (1): 2398.

Chen, Tao, Bin Zhang, Thomas Ziegenhals, Archana B. Prusty, Sebastian Fröhler, Clemens Grimm, Yuhui Hu, et al. 2019. “A Missense Mutation in SNRPE Linked to Non-Syndromal Microcephaly Interferes with U SnRNP Assembly and Pre-MRNA Splicing.” *PLoS Genetics* 15 (10): e1008460.

Chen, Yong, Ting Ma, Tingting Zhang, and Lei Ma. 2023. “Trends in the Evolution of Intronless Genes in Poaceae.” *Frontiers in Plant Science* 14 (February): 1065631.

Chen, Yuhan, Qingyang Huang, Wen Liu, Qiong Zhu, Chun-Ping Cui, Liang Xu, Xing Guo, et al. 2018. “Mutually Exclusive Acetylation and Ubiquitylation of the Splicing Factor SRSF5 Control Tumor Growth.” *Nature Communications* 9 (1). https://doi.org/10.1038/s41467-018-04815-3.

Chen, Zhixian, Jianfeng Gan, Zhi Wei, Mo Zhang, Yan Du, Congjian Xu, and Hongbo Zhao. 2022. “The Emerging Role of PRMT6 in Cancer.” *Frontiers in Oncology* 12 (March): 841381.

Cheng, Donghang, Sergio Valente, Sabrina Castellano, Gianluca Sbardella, Roberto Di Santo, Roberta Costi, Mark T. Bedford, and Antonello Mai. 2011. “Novel 3,5-Bis(Bromohydroxybenzylidene)Piperidin-4-Ones as Coactivator-Associated Arginine Methyltransferase 1 Inhibitors: Enzyme Selectivity and Cellular Activity.” *Journal of Medicinal Chemistry* 54 (13): 4928–32.

Cheong, Agnes, Danielle Archambault, Rinat Degani, Elizabeth Iverson, Kimberly D. Tremblay, and Jesse Mager. 2020. “Nuclear-Encoded Mitochondrial Ribosomal Proteins Are Required to Initiate Gastrulation.” *Development (Cambridge, England)* 147 (10): dev188714.

Correa, Bruna R., Patricia Rosa de Araujo, Mei Qiao, Suzanne C. Burns, Chen Chen, Richard Schlegel, Seema Agarwal, Pedro A. F. Galante, and Luiz O. F. Penalva. 2016. “Functional Genomics Analyses of RNA-Binding Proteins Reveal the Splicing Regulator SNRPB as an Oncogenic Candidate in Glioblastoma.” *Genome Biology* 17 (1): 125.

Cox, Jürgen, Marco Y. Hein, Christian A. Luber, Igor Paron, Nagarjuna Nagaraj, and Matthias Mann. 2014. “Accurate Proteome-Wide Label-Free Quantification by Delayed Normalization and Maximal Peptide Ratio Extraction, Termed MaxLFQ.” *Molecular & Cellular Proteomics: MCP* 13 (9): 2513–26.

Cox, Jürgen, and Matthias Mann. 2008. “MaxQuant Enables High Peptide Identification Rates, Individualized p.p.b.-Range Mass Accuracies and Proteome-Wide Protein Quantification.” *Nature Biotechnology* 26 (12): 1367–72.

Cox, Jürgen, Nadin Neuhauser, Annette Michalski, Richard A. Scheltema, Jesper V. Olsen, and Matthias Mann. 2011. “Andromeda: A Peptide Search Engine Integrated into the MaxQuant Environment.” *Journal of Proteome Research* 10 (4): 1794–1805.

Cozzani, Emanuele, Massimo Drosera, Giulia Gasparini, and Aurora Parodi. 2014. “Serology of Lupus Erythematosus: Correlation between Immunopathological Features and Clinical Aspects.” *Autoimmune Diseases* 2014 (February): 321359.

Crawford, Thomas O., Basil T. Darras, John W. Day, Sally Dunaway Young, Tina Duong, Leslie L. Nelson, Doreen Barrett, et al. 2024. “Safety and Efficacy of Apitegromab in Patients with Spinal Muscular Atrophy Types 2 and 3: The Phase 2 TOPAZ Study.” *Neurology* 102 (5): e209151.

Cretu, Constantin, Jana Schmitzová, Almudena Ponce-Salvatierra, Olexandr Dybkov, Evelina I. De Laurentiis, Kundan Sharma, Cindy L. Will, Henning Urlaub, Reinhard Lührmann, and Vladimir Pena. 2016. “Molecular Architecture of SF3b and Structural Consequences of Its Cancer-Related Mutations.” *Molecular Cell* 64 (2): 307–19.

Crow, Karen D., and Günter P. Wagner. 2006. “Proceedings of the SMBE Tri-National Young Investigators’ Workshop 2005. What Is the Role of Genome Duplication in the Evolution of Complexity and Diversity?” *Molecular Biology and Evolution* 23 (5): 887–92.

Curry-Hyde, Ashton, Bei Jun Chen, James D. Mills, and Michael Janitz. 2018. “Microexons: Novel Regulators of the Transcriptome.” *Journal of Human Transcriptome* 2 (1): 1–6.

Dávila López, Marcela, Magnus Alm Rosenblad, and Tore Samuelsson. 2008. “Computational Screen for Spliceosomal RNA Genes Aids in Defining the Phylogenetic Distribution of Major and Minor Spliceosomal Components.” *Nucleic Acids Research* 36 (9): 3001–10.

DeAngelo, Joseph D., Maxim I. Maron, Jacob S. Roth, Aliza M. Silverstein, Varun Gupta, Stephanie Stransky, Joel Basken, et al. 2024. “Productive MRNA Chromatin Escape Is Promoted by PRMT5 Methylation of SNRPB.” *BioRxivorg*. https://doi.org/10.1101/2024.08.09.607355.

DeBoever, Christopher, Emanuela M. Ghia, Peter J. Shepard, Laura Rassenti, Christian L. Barrett, Kristen Jepsen, Catriona H. M. Jamieson, Dennis Carson, Thomas J. Kipps, and Kelly A. Frazer. 2015. “Transcriptome Sequencing Reveals Potential Mechanism of Cryptic 3’ Splice Site Selection in SF3B1-Mutated Cancers.” *PLoS Computational Biology* 11 (3): e1004105.

DepMap, Broad. 2024. “DepMap 24Q4 Public.” Figshare+. https://doi.org/10.25452/FIGSHARE.PLUS.27993248.V1.

Deribe, Yonathan Lissanu, Tony Pawson, and Ivan Dikic. 2010. “Post-Translational Modifications in Signal Integration.” *Nature Structural & Molecular Biology* 17 (6): 666–72.

Diss, Guillaume, Isabelle Gagnon-Arsenault, Anne-Marie Dion-Coté, Hélène Vignaud, Diana I. Ascencio, Caroline M. Berger, and Christian R. Landry. 2017. “Gene Duplication Can Impart Fragility, Not Robustness, in the Yeast Protein Interaction Network.” *Science (New York, N.Y.)* 355 (6325): 630–34.

Dittmar, Gunnar, Daniel Perez Hernandez, Elisabeth Kowenz-Leutz, Marieluise Kirchner, Günther Kahlert, Radoslaw Wesolowski, Katharina Baum, et al. 2019. “PRISMA: Protein Interaction Screen on Peptide Matrix Reveals Interaction Footprints and Modifications-Dependent Interactome of Intrinsically Disordered C/EBPβ.” *IScience* 13 (March): 351–70.

Dong, Rui, Xuejun Li, and Kwok-On Lai. 2021. “Activity and Function of the PRMT8 Protein Arginine Methyltransferase in Neurons.” *Life (Basel, Switzerland)* 11 (11): 1132.

D/"orner, Kerstin, Michelle Gut, Daan Overwijn, Fan Cao, Matej Siketanc, Stephanie Heinrich, Nicole Beuret, Timothy Sharpe, Kresten Lindorff-Larsen, and Maria Hondele. 2024. “Tag with Caution - How Protein Tagging Influences the Formation of Condensates.” *BioRxiv*. https://doi.org/10.1101/2024.10.04.616694.

Douglas, Andrew G. L., and Matthew J. A. Wood. 2011. “RNA Splicing: Disease and Therapy.” *Briefings in Functional Genomics* 10 (3): 151–64.

Drobek, Michaela. 2022. “Paralogous Genes Involved in Embryonic Development: Lessons from the Eye and Other Tissues.” *Genes* 13 (11): 2082.

Dvinge, Heidi, Jamie Guenthoer, Peggy L. Porter, and Robert K. Bradley. 2019. “RNA Components of the Spliceosome Regulate Tissue- and Cancer-Specific Alternative Splicing.” *Genome Research* 29 (10): 1591–1604.

Enam, Syed Usman, Boris Zinshteyn, Daniel H. Goldman, Madeline Cassani, Nathan M. Livingston, Geraldine Seydoux, and Rachel Green. 2020. “Puromycin Reactivity Does Not Accurately Localize Translation at the Subcellular Level.” *ELife* 9 (August). https://doi.org/10.7554/eLife.60303.

Erce, Melissa A., Chi N. I. Pang, Gene Hart-Smith, and Marc R. Wilkins. 2012. “The Methylproteome and the Intracellular Methylation Network.” *Proteomics* 12 (4–5): 564–86.

Erdinc, Direnis, Alejandro Rodríguez-Luis, Mahmoud R. Fassad, Sarah Mackenzie, Christopher M. Watson, Sebastian Valenzuela, Xie Xie, et al. 2023. “Pathological Variants in TOP3A Cause Distinct Disorders of Mitochondrial and Nuclear Genome Stability.” *EMBO Molecular Medicine* 15 (5): e16775.

Falkowska, Anna, Izabela Gutowska, Marta Goschorska, Przemysław Nowacki, Dariusz Chlubek, and Irena Baranowska-Bosiacka. 2015. “Energy Metabolism of the Brain, Including the Cooperation between Astrocytes and Neurons, Especially in the Context of Glycogen Metabolism.” *International Journal of Molecular Sciences* 16 (11): 25959–81.

Fan, Jing, Kimberly A. Krautkramer, Jessica L. Feldman, and John M. Denu. 2015. “Metabolic Regulation of Histone Post-Translational Modifications.” *ACS Chemical Biology* 10 (1): 95–108.

Fernandopulle, Michael S., Ryan Prestil, Christopher Grunseich, Chao Wang, Li Gan, and Michael E. Ward. 2018. “Transcription Factor-Mediated Differentiation of Human IPSCs into Neurons.” *Et al [Current Protocols in Cell Biology]* 79 (1): e51.

Filali, Mohammed, Jianping Qiu, Sita Awasthi, Utz Fischer, Dimitri Monos, and Malek Kamoun. 1999. “Monoclonal Antibody Specific to a Subclass of Polyproline-arg Motif Provides Evidence for the Presence of an SnRNA-free Spliceosomal Sm Protein Complex in Vivo: Implications for Molecular Interactions Involving Proline-rich Sequences of Sm B/B′ Proteins.” *Journal of Cellular Biochemistry* 74 (2): 168–80.

Finkel, Richard S., Samuel H. Hughes, Julieann Parker, Matthew Civitello, Alfonso Lavado, Heather C. Mefford, Lutz Mueller, Heidemarie Kletzl, and Prenatal SMA Risdiplam Study Group. 2025. “Risdiplam for Prenatal Therapy of Spinal Muscular Atrophy.” *The New England Journal of Medicine*, February. https://doi.org/10.1056/NEJMc2300802.

Friesen, W. J., S. Paushkin, A. Wyce, S. Massenet, G. S. Pesiridis, G. Van Duyne, J. Rappsilber, M. Mann, and G. Dreyfuss. 2001. “The Methylosome, a 20S Complex Containing JBP1 and PICln, Produces Dimethylarginine-Modified Sm Proteins.” *Molecular and Cellular Biology* 21 (24): 8289–8300.

Gao, Guozhen, Liang Zhang, Oscar D. Villarreal, Wei He, Dan Su, Ella Bedford, Phoebe Moh, et al. 2019. “PRMT1 Loss Sensitizes Cells to PRMT5 Inhibition.” *Nucleic Acids Research* 47 (10): 5038–48.

Glenn, C. C., S. Saitoh, M. T. Jong, M. M. Filbrandt, U. Surti, D. J. Driscoll, and R. D. Nicholls. 1996. “Gene Structure, DNA Methylation, and Imprinted Expression of the Human SNRPN Gene.” *American Journal of Human Genetics* 58 (2): 335–46.

Gohr, André, Federica Mantica, Antonio Hermoso-Pulido, Javier Tapial, Yamile Márquez, and Manuel Irimia. 2022. “Computational Analysis of Alternative Splicing Using VAST-TOOLS and the VastDB Framework.” *Methods in Molecular Biology (Clifton, N.J.)* 2537: 97–128.

Gray, T. A., S. Saitoh, and R. D. Nicholls. 1999. “An Imprinted, Mammalian Bicistronic Transcript Encodes Two Independent Proteins.” *Proceedings of the National Academy of Sciences of the United States of America* 96 (10): 5616–21.

Gray, Todd A., Megan J. Smithwick, Melanie A. Schaldach, Diana L. Martone, Jennifer A. Marshall Graves, John R. McCarrey, and Robert D. Nicholls. 1999. “Concerted Regulation and Molecular Evolution of the Duplicated SNRPB’/B and SNRPNIoci.” *Nucleic Acids Research* 27 (23): 4577–84.

Griffin, Casey, and Jean-Pierre Saint-Jeannet. 2020. “Spliceosomopathies: Diseases and Mechanisms.” *Developmental Dynamics: An Official Publication of the American Association of Anatomists* 249 (9): 1038–46.

Grimaldi, K., D. A. Horn, L. D. Hudson, G. Terenghi, P. Barton, J. M. Polak, and D. S. Latchman. 1993. “Expression of the SmN Splicing Protein Is Developmentally Regulated in the Rodent Brain but Not in the Rodent Heart.” *Developmental Biology* 156 (2): 319–23.

Grosso, Ana Rita, Anita Q. Gomes, Nuno L. Barbosa-Morais, Sandra Caldeira, Natalie P. Thorne, Godfrey Grech, Marieke von Lindern, and Maria Carmo-Fonseca. 2008. “Tissue-Specific Splicing Factor Gene Expression Signatures.” *Nucleic Acids Research* 36 (15): 4823–32.

Guo, Ailan, Hongbo Gu, Jing Zhou, Daniel Mulhern, Yi Wang, Kimberly A. Lee, Vicky Yang, et al. 2014. “Immunoaffinity Enrichment and Mass Spectrometry Analysis of Protein Methylation.” *Molecular & Cellular Proteomics: MCP* 13 (1): 372–87.

Hammoudi, Valentin, Georgios Vlachakis, M. Eric Schranz, and Harrold A. van den Burg. 2016. “Whole-Genome Duplications Followed by Tandem Duplications Drive Diversification of the Protein Modifier SUMO in Angiosperms.” *The New Phytologist* 211 (1): 172–85.

Han, Dong, Mengxi Huang, Ting Wang, Zhiping Li, Yanyan Chen, Chao Liu, Zengjie Lei, and Xiaoyuan Chu. 2019. “Lysine Methylation of Transcription Factors in Cancer.” *Cell Death & Disease* 10 (4): 290.

Hartley, Antja-Voy, and Tao Lu. 2020. “Modulating the Modulators: Regulation of Protein Arginine Methyltransferases by Post-Translational Modifications.” *Drug Discovery Today* 25 (9): 1735–43.

Hoogenhof, Maarten M. G. van den, Yigal M. Pinto, and Esther E. Creemers. 2016. “RNA Splicing.” *Circulation Research* 118 (3): 454–68.

Hsu, Sheng-Chieh, Chia-Lin Chen, Mei-Ling Cheng, Cheng-Ying Chu, Chun A. Changou, Yen-Ling Yu, Shauh-Der Yeh, et al. 2021. “Arginine Starvation Elicits Chromatin Leakage and

CGAS-STING Activation via Epigenetic Silencing of Metabolic and DNA-Repair Genes." *Theranostics* 11 (15): 7527–45.

Huang, Lei, Xiao-Ou Zhang, Esteban J. Rozen, Xiaomei Sun, Benjamin Sallis, Odette Verdejo-Torres, Kim Wigglesworth, et al. 2022. "PRMT5 Activates AKT via Methylation to Promote Tumor Metastasis." *Nature Communications* 13 (1): 3955.

Huang, Liang-Kai, and Mao-Jiun J. Wang. 1995. "Image Thresholding by Minimizing the Measures of Fuzziness." *Pattern Recognition* 28 (1): 41–51.

Hughes, Christopher S., Sophie Moggridge, Torsten Müller, Poul H. Sorensen, Gregg B. Morin, and Jeroen Krijgsveld. 2019. "Single-Pot, Solid-Phase-Enhanced Sample Preparation for Proteomics Experiments." *Nature Protocols* 14 (1): 68–85.

Huntriss, J. D., J. A. Barr, D. A. Horn, D. G. Williams, and D. S. Latchman. 1994. "Mice Lacking Snrpn Expression Show Normal Regulation of Neuronal Alternative Splicing Events." *Molecular Biology Reports* 20 (1): 19–25.

Huntriss, J. D., D. S. Latchman, and D. G. Williams. 1993. "Lupus Autoantibodies Discriminate between the Highly Homologous Sm Polypeptides B/B' and SmN by Binding an Epitope Restricted to B/B'." *Clinical and Experimental Immunology* 92 (2): 263–67.

Hutten, Saskia, Georgia Chachami, Ulrike Winter, Frauke Melchior, and Angus I. Lamond. 2014. "A Role for the Cajal-Body-Associated SUMO Isopeptidase USPL1 in SnRNA Transcription Mediated by RNA Polymerase II." *Journal of Cell Science* 127 (Pt 5): 1065–78.

Hyjek-Składanowska, Malwina, Mateusz Bajczyk, Marcin Gołębiewski, Przemysław Nuc, Agnieszka Kołowerzo-Lubnau, Artur Jarmołowski, and Dariusz Jan Smoliński. 2020. "Core Spliceosomal Sm Proteins as Constituents of Cytoplasmic MRNPs in Plants." *The Plant Journal: For Cell and Molecular Biology* 103 (3): 1155–73.

Inglis, Alison J., Alina Guna, Ángel Gálvez-Merchán, Akshaye Pal, Theodore K. Esantsi, Heather R. Keys, Evgeni M. Frenkel, Robert Oania, Jonathan S. Weissman, and Rebecca M. Voorhees. 2023. "Coupled Protein Quality Control during Nonsense-Mediated MRNA Decay." *Journal of Cell Science* 136 (10). https://doi.org/10.1242/jcs.261216.

Irimia, Manuel, Robert J. Weatheritt, Jonathan D. Ellis, Neelroop N. Parikshak, Thomas Gonatopoulos-Pournatzis, Mariana Babor, Mathieu Quesnel-Vallières, et al. 2014. "A Highly Conserved Program of Neuronal Microexons Is Misregulated in Autistic Brains." *Cell* 159 (7): 1511–23.

Jaqaman, Khuloud, Dinah Loerke, Marcel Mettlen, Hirotaka Kuwata, Sergio Grinstein, Sandra L. Schmid, and Gaudenz Danuser. 2008. “Robust Single-Particle Tracking in Live-Cell Time-Lapse Sequences.” *Nature Methods* 5 (8): 695–702.

Jung, Hyunchul, Kang Seon Lee, and Jung Kyoon Choi. 2021. “Comprehensive Characterisation of Intronic Mis-Splicing Mutations in Human Cancers.” *Oncogene* 40 (7): 1347–61.

Kambach, C., S. Walke, R. Young, J. M. Avis, E. de la Fortelle, V. A. Raker, R. Lührmann, J. Li, and K. Nagai. 1999. “Crystal Structures of Two Sm Protein Complexes and Their Implications for the Assembly of the Spliceosomal SnRNPs.” *Cell* 96 (3): 375–87.

Kaminska, Dorota. 2024. “The Role of RNA Splicing in Liver Function and Disease: A Focus on Metabolic Dysfunction-Associated Steatotic Liver Disease.” *Genes* 15 (9): 1181.

Kapur, J. N., P. K. Sahoo, and A. K. C. Wong. 1985. “A New Method for Gray-Level Picture Thresholding Using the Entropy of the Histogram.” *Computer Vision, Graphics, and Image Processing* 29 (3): 273–85.

Kapustin, Yuri, Elcie Chan, Rupa Sarkar, Frederick Wong, Igor Vorechovsky, Robert M. Winston, Tatiana Tatusova, and Nick J. Dibb. 2011. “Cryptic Splice Sites and Split Genes.” *Nucleic Acids Research* 39 (14): 5837–44.

Kara, Eleanna, Aoife P. Kiely, Christos Proukakis, Nicola Giffin, Seth Love, Jason Hehir, Khadija Rantell, et al. 2014. “A 6.4 Mb Duplication of the α-Synuclein Locus Causing Frontotemporal Dementia and Parkinsonism: Phenotype-Genotype Correlations.” *JAMA Neurology* 71 (9): 1162–71.

Khatri, Deepak, Audrey Putoux, Audric Cologne, Sophie Kaltenbach, Alicia Besson, Eloïse Bertiaux, Justine Guguin, et al. 2023. “Deficiency of the Minor Spliceosome Component U4atac SnRNA Secondarily Results in Ciliary Defects in Human and Zebrafish.” *Proceedings of the National Academy of Sciences of the United States of America* 120 (9): e2102569120.

Kim, Kee K., Yong C. Kim, Robert S. Adelstein, and Sachiyo Kawamoto. 2011. “Fox-3 and PSF Interact to Activate Neural Cell-Specific Alternative Splicing.” *Nucleic Acids Research* 39 (8): 3064–78.

Knill, Chris, Ellie J. Henderson, Craig Johnson, Vun Yee Wah, Kevin Cheng, Annie J. Forster, and Nobue Itasaki. 2024. “Defects of the Spliceosomal Gene SNRPB Affect Osteo- and Chondro-Differentiation.” *The FEBS Journal* 291 (2): 272–91.

Koonin, Eugene V. 2005. “Orthologs, Paralogs, and Evolutionary Genomics.” *Annual Review of Genetics* 39: 309–38.

Kretova, Miroslava, Tomas Selicky, Ingrid Cipakova, and Lubos Cipak. 2023. “Regulation of Pre-MRNA Splicing: Indispensable Role of Post-Translational Modifications of Splicing Factors.” *Life* 13 (3). https://doi.org/10.3390/life13030604.

Krzyzanowski, Adrian, Lea Marie Esser, Anthony Willaume, Renaud Prudent, Christoph Peter, Peter ’t Hart, and Herbert Waldmann. 2022. “Development of Macrocyclic PRMT5-Adaptor Protein Interaction Inhibitors.” *Journal of Medicinal Chemistry* 65 (22): 15300–311.

Kumar, Vipul, Frederick W. Alt, and Richard L. Frock. 2016. “PAXX and XLF DNA Repair Factors Are Functionally Redundant in Joining DNA Breaks in a G1-Arrested Progenitor B-Cell Line.” *Proceedings of the National Academy of Sciences of the United States of America* 113 (38): 10619–24.

Kuzmin, Elena, John S. Taylor, and Charles Boone. 2022. “Retention of Duplicated Genes in Evolution.” *Trends in Genetics: TIG* 38 (1): 59–72.

Lambuta, Ruxandra A., Luca Nanni, Yuanlong Liu, Juan Diaz-Miyar, Arvind Iyer, Daniele Tavernari, Natalya Katanayeva, Giovanni Ciriello, and Elisa Oricchio. 2023. “Whole-Genome Doubling Drives Oncogenic Loss of Chromatin Segregation.” *Nature* 615 (7954): 925–33.

Larsen, Sara C., Kathrine B. Sylvestersen, Andreas Mund, David Lyon, Meeli Mullari, Maria V. Madsen, Jeremy A. Daniel, Lars J. Jensen, and Michael L. Nielsen. 2016. “Proteome-Wide Analysis of Arginine Monomethylation Reveals Widespread Occurrence in Human Cells.” *Science Signaling* 9 (443): rs9.

Larue, Graham E., Marek Eliáš, and Scott W. Roy. 2020. “Expansion and Transformation of the Minor Spliceosomal System in the Slime Mold*Physarum Polycephalum*.” *BioRxiv*. bioRxiv. https://doi.org/10.1101/2020.10.12.336362.

Lee, Jee-San, Nathalie Lamarche-Vane, and Stéphane Richard. 2022. “Microexon Alternative Splicing of Small GTPase Regulators: Implication in Central Nervous System Diseases.” *Wiley Interdisciplinary Reviews. RNA* 13 (2): e1678.

Lee, Seul-Yi, Tuan Anh Vuong, Hyun-Kyung So, Hyun-Ji Kim, Yoo Bin Kim, Jong-Sun Kang, Ilmin Kwon, and Hana Cho. 2020. “PRMT7 Deficiency Causes Dysregulation of the HCN Channels in the CA1 Pyramidal Cells and Impairment of Social Behaviors.” *Experimental & Molecular Medicine* 52 (4): 604–14.

Lerner, M. R., and J. A. Steitz. 1979. “Antibodies to Small Nuclear RNAs Complexed with Proteins Are Produced by Patients with Systemic Lupus Erythematosus.” *Proceedings of the National Academy of Sciences of the United States of America* 76 (11): 5495–99.

Li, Wen-Juan, Yao-Hui He, Jing-Jing Yang, Guo-Sheng Hu, Yi-An Lin, Ting Ran, Bing-Ling Peng, et al. 2021. “Profiling PRMT Methylome Reveals Roles of HnRNPA1 Arginine Methylation in RNA Splicing and Cell Growth.” *Nature Communications* 12 (1): 1946.

Li, Zhongwei, Chaozhen Chen, Hongmei Yong, Lei Jiang, Pengfei Wang, Sen Meng, Sufang Chu, et al. 2023. “PRMT2 Promotes RCC Tumorigenesis and Metastasis via Enhancing WNT5A Transcriptional Expression.” *Cell Death & Disease* 14 (5): 322.

Lin, Luyao, Qingxia Yuan, Jiayi Gu, Guangyu Bai, Xianling Cong, Qianying Hu, Jingyao Hou, et al. 2024. “CARM1-Mediated OGT Arginine Methylation Promotes Non-Small Cell Lung Cancer Glycolysis by Stabilizing OGT.” *Cell Death & Disease* 15 (12): 927.

Liu, Qing, Jinke Xu, Yunhua Zhu, Yuxing Mo, Xue-Feng Yao, Ruozhong Wang, Wenzhen Ku, et al. 2020. “The Copy Number Variation of OsMTD1 Regulates Rice Plant Architecture.” *Frontiers in Plant Science* 11: 620282.

Long, Yunxin, Weng Hong Sou, Kristen Wing Yu Yung, Haizhen Liu, Stephanie Winn Chee Wan, Qingyun Li, Chuyue Zeng, et al. 2019. “Distinct Mechanisms Govern the Phosphorylation of Different SR Protein Splicing Factors.” *The Journal of Biological Chemistry* 294 (4): 1312–27.

Lorenzi, Claudio, Sylvain Barriere, Katharina Arnold, Reini F. Luco, Andrew J. Oldfield, and William Ritchie. 2021. “IRFinder-S: A Comprehensive Suite to Discover and Explore Intron Retention.” *Genome Biology* 22 (1): 307.

Lorković, Zdravko J., Julia Hilscher, and Andrea Barta. 2004. “Use of Fluorescent Protein Tags to Study Nuclear Organization of the Spliceosomal Machinery in Transiently Transformed Living Plant Cells.” *Molecular Biology of the Cell* 15 (7): 3233–43.

Lynch, Danielle C., Timothée Revil, Jeremy Schwartzentruber, Elizabeth J. Bhoj, A. Micheil Innes, Ryan E. Lamont, Edmond G. Lemire, et al. 2014. “Disrupted Auto-Regulation of the Spliceosomal Gene SNRPB Causes Cerebro-Costo-Mandibular Syndrome.” *Nature Communications* 5 (1): 4483.

Machyna, Martin, Patricia Heyn, and Karla M. Neugebauer. 2013. “Cajal Bodies: Where Form Meets Function.” *Wiley Interdisciplinary Reviews. RNA* 4 (1): 17–34.

Mahajan, Aparna, Martin Herrmann, and Luis E. Muñoz. 2016. “Clearance Deficiency and Cell Death Pathways: A Model for the Pathogenesis of SLE.” *Frontiers in Immunology* 7 (February): 35.

Mallapaty, Smriti. 2025. “Rare Genetic Disorder Treated in Womb for the First Time.” *Nature* 638 (8052): 869.

Maraschi, Annamaria, Valentina Gumina, Jessica Dragotto, Claudia Colombrita, Miguel Mompeán, Emanuele Buratti, Vincenzo Silani, Marco Feligioni, and Antonia Ratti. 2021. “SUMOylation Regulates TDP-43 Splicing Activity and Nucleocytoplasmic Distribution.” *Molecular Neurobiology* 58 (11): 5682–5702.

Marasco, Luciano E., Gwendal Dujardin, Rui Sousa-Luís, Ying Hsiu Liu, Jose N. Stigliano, Tomoki Nomakuchi, Nick J. Proudfoot, Adrian R. Krainer, and Alberto R. Kornblihtt. 2022. “Counteracting Chromatin Effects of a Splicing-Correcting Antisense Oligonucleotide Improves Its Therapeutic Efficacy in Spinal Muscular Atrophy.” *Cell* 185 (12): 2057-2070.e15.

Maron, Maxim I., Alyssa D. Casill, Varun Gupta, Jacob S. Roth, Simone Sidoli, Charles C. Query, Matthew J. Gamble, and David Shechter. 2022. “Type I and II PRMTs Inversely Regulate Post-Transcriptional Intron Detention through Sm and CHTOP Methylation.” *ELife* 11 (January). https://doi.org/10.7554/eLife.72867.

Matter, L., K. Schopfer, J. A. Wilhelm, T. Nyffenegger, R. F. Parisot, and E. M. De Robertis. 1982. “Molecular Characterization of Ribonucleoprotein Antigens Bound by Antinuclear Antibodies. A Diagnostic Evaluation.” *Arthritis and Rheumatism* 25 (11): 1278–83.

McGowen, Michael R., Clay Clark, and John Gatesy. 2008. “The Vestigial Olfactory Receptor Subgenome of Odontocete Whales: Phylogenetic Congruence between Gene-Tree Reconciliation and Supermatrix Methods.” *Systematic Biology* 57 (4): 574–90.

McKay, Susannah L., and Tracy L. Johnson. 2010. “A Bird’s-Eye View of Post-Translational Modifications in the Spliceosome and Their Roles in Spliceosome Dynamics.” *Molecular BioSystems* 6 (11): 2093–2102.

Mentch, Samantha J., and Jason W. Locasale. 2016. “One-Carbon Metabolism and Epigenetics: Understanding the Specificity.” *Annals of the New York Academy of Sciences* 1363 (1): 91–98.

Merico, Annamaria, Pavol Sulo, Jure Piskur, and Concetta Compagno. 2007. “Fermentative Lifestyle in Yeasts Belonging to the Saccharomyces Complex.” *The FEBS Journal* 274 (4): 976–89.

Moriyama, Yuuta, and Kazuko Koshiba-Takeuchi. 2018. “Significance of Whole-Genome Duplications on the Emergence of Evolutionary Novelties.” *Briefings in Functional Genomics* 17 (5): 329–38.

Mourão, André, Sophie Bonnal, Komal Soni, Lisa Warner, Rémy Bordonné, Juan Valcárcel, and Michael Sattler. 2016. “Structural Basis for the Recognition of Spliceosomal SmN/B/B’

Proteins by the RBM5 OCRE Domain in Splicing Regulation." *ELife* 5 (November). https://doi.org/10.7554/eLife.14707.

Mulvaney, Kathleen M., Christa Blomquist, Nischal Acharya, Ruitong Li, Matthew J. Ranaghan, Meghan O'Keefe, Diego J. Rodriguez, et al. 2021. "Molecular Basis for Substrate Recruitment to the PRMT5 Methylosome." *Molecular Cell* 81 (17): 3481-3495.e7.

Musiani, Daniele, Jabez Bok, Enrico Massignani, Liling Wu, Tommaso Tabaglio, Marica Rosaria Ippolito, Alessandro Cuomo, et al. 2019. "Proteomics Profiling of Arginine Methylation Defines PRMT5 Substrate Specificity." *Science Signaling* 12 (575): eaat8388.

Muzafar, Suraya, Ravi Datta Sharma, Neeraj Chauhan, and Rajendra Prasad. 2021. "Intron Distribution and Emerging Role of Alternative Splicing in Fungi." *FEMS Microbiology Letters* 368 (19). https://doi.org/10.1093/femsle/fnab135.

Nasif, Sofia, Martino Colombo, Anne-Christine Uldry, Markus S. Schröder, Simone de Brot, and Oliver Mühlemann. 2023. "Inhibition of Nonsense-Mediated MRNA Decay Reduces the Tumorigenicity of Human Fibrosarcoma Cells." *NAR Cancer* 5 (3): zcad048.

Ohtani, Misato. 2018. "Plant SnRNP Biogenesis: A Perspective from the Nucleolus and Cajal Bodies." *Frontiers in Plant Science* 8 (January). https://doi.org/10.3389/fpls.2017.02184.

Oromendia, Ana B., and Angelika Amon. 2014. "Aneuploidy: Implications for Protein Homeostasis and Disease." *Disease Models & Mechanisms* 7 (1): 15–20.

Osemwenkhae, P. O., and N. B. Aguebor-Ogie. 2021. "Analysis of Intronless Genes Involved in Oscillation and Differentiation." *Journal of Applied Sciences & Environmental Management* 25 (9): 1551–58.

Ottesen, Eric W., and Ravindra N. Singh. 2024. "Synergistic Effect of an Antisense Oligonucleotide and Small Molecule on Splicing Correction of the Spinal Muscular Atrophy Gene." *Neuroscience Insights*. SAGE Publications.

Ouyang, Yang, Qi Wu, Juanjuan Li, Si Sun, and Shengrong Sun. 2020. "S-Adenosylmethionine: A Metabolite Critical to the Regulation of Autophagy." *Cell Proliferation* 53 (11): e12891.

Ozçelik, T., S. Leff, W. Robinson, T. Donlon, M. Lalande, E. Sanjines, A. Schinzel, and U. Francke. 1992. "Small Nuclear Ribonucleoprotein Polypeptide N (SNRPN), an Expressed Gene in the Prader-Willi Syndrome Critical Region." *Nature Genetics* 2 (4): 265–69.

Parada, Guillermo E., Roberto Munita, Ilias Georgakopoulos-Soares, Hugo J. R. Fernandes, Veronika R. Kedlian, Emmanouil Metzakopian, Maria Estela Andres, Eric A. Miska, and Martin

Hemberg. 2021. “MicroExonator Enables Systematic Discovery and Quantification of Microexons across Mouse Embryonic Development.” *Genome Biology* 22 (1): 43.

Park, Byung-Yong, Melanie Tachi-Duprat, Chibuike Ihewulezi, Arun Devotta, and Jean-Pierre Saint-Jeannet. 2022. “The Core Splicing Factors EFTUD2, SNRPB and TXNL4A Are Essential for Neural Crest and Craniofacial Development.” *Journal of Developmental Biology* 10 (3). https://doi.org/10.3390/jdb10030029.

Pataky, Mark W., Carrie J. Heppelmann, Kyle Sevits, Aneesh K. Asokan, Katherine Klaus, and K. Sreekumaran Nair. 2024. “28-OR: Posttranslational Modifications in Skeletal Muscle Direct Divergent Metabolic Responses to Different Exercise Training Modes.” *Diabetes* 73 (Supplement_1). https://doi.org/10.2337/db24-28-or.

Paushkin, Sergey, Amélie K. Gubitz, Séverine Massenet, and Gideon Dreyfuss. 2002. “The SMN Complex, an Assemblyosome of Ribonucleoproteins.” *Current Opinion in Cell Biology* 14 (3): 305–12.

Pecori, Riccardo, Salvatore Di Giorgio, J. Paulo Lorenzo, and F. Nina Papavasiliou. 2022. “Functions and Consequences of AID/APOBEC-Mediated DNA and RNA Deamination.” *Nature Reviews. Genetics* 23 (8): 505–18.

Pedrotti, Simona, Roberta Busà, Claudia Compagnucci, and Claudio Sette. 2012. “The RNA Recognition Motif Protein RBM11 Is a Novel Tissue-Specific Splicing Regulator.” *Nucleic Acids Research* 40 (3): 1021–32.

Perry, George H., Nathaniel J. Dominy, Katrina G. Claw, Arthur S. Lee, Heike Fiegler, Richard Redon, John Werner, et al. 2007. “Diet and the Evolution of Human Amylase Gene Copy Number Variation.” *Nature Genetics* 39 (10): 1256–60.

Pham, Hoang Quoc Hai, Xiaoqun Tao, and Yanzhong Yang. 2023. “Protein Arginine Methylation in Transcription and Epigenetic Regulation.” *Frontiers in Epigenetics and Epigenomics* 1 (August). https://doi.org/10.3389/freae.2023.1245832.

Phipson, Belinda, Stanley Lee, Ian J. Majewski, Warren S. Alexander, and Gordon K. Smyth. 2016. “Robust Hyperparameter Estimation Protects against Hypervariable Genes and Improves Power to Detect Differential Expression.” *The Annals of Applied Statistics* 10 (2): 946–63.

Pineda, Jose Mario Bello, and Robert K. Bradley. 2018. “Most Human Introns Are Recognized via Multiple and Tissue-Specific Branchpoints.” *Genes & Development* 32 (7–8): 577–91.

Porensky, Paul N., and Arthur H. M. Burghes. 2013. “Antisense Oligonucleotides for the Treatment of Spinal Muscular Atrophy.” *Human Gene Therapy* 24 (5): 489–98.

Powell-Rodgers, Geralle, Mujeeb Ur Rehman Pirzada, Jahmiera Richee, Courtney F. Jungers, Sarah Colijn, Amber N. Stratman, and Sergej Djuranovic. 2024. “Role of U11/U12 Minor Spliceosome Gene ZCRB1 in Ciliogenesis and WNT Signaling.” *BioRxivorg*. https://doi.org/10.1101/2024.08.09.607392.

Pozzi, Berta, Laureano Bragado, Cindy L. Will, Pablo Mammi, Guillermo Risso, Henning Urlaub, Reinhard Lührmann, and Anabella Srebrow. 2017. “SUMO Conjugation to Spliceosomal Proteins Is Required for Efficient Pre-MRNA Splicing.” *Nucleic Acids Research* 45 (11): 6729–45.

Pu, William T., Grigory B. Krapivinsky, Luba Krapivinsky, and David E. Clapham. 1999. “PICln Inhibits SnRNP Biogenesis by Binding Core Spliceosomal Proteins.” *Molecular and Cellular Biology* 19 (6): 4113–20.

Qualmann, Britta, and Michael M. Kessels. 2021. “The Role of Protein Arginine Methylation as Post-Translational Modification on Actin Cytoskeletal Components in Neuronal Structure and Function.” *Cells (Basel, Switzerland)* 10 (5): 1079.

Rae, Caroline D., Joseph A. Baur, Karin Borges, Gerald Dienel, Carlos Manlio Díaz-García, Starlette R. Douglass, Kelly Drew, et al. 2024. “Brain Energy Metabolism: A Roadmap for Future Research.” *Journal of Neurochemistry* 168 (5): 910–54.

Ramazi, Shahin, and Javad Zahiri. 2021. “Posttranslational Modifications in Proteins: Resources, Tools and Prediction Methods.” *Database: The Journal of Biological Databases and Curation* 2021 (April). https://doi.org/10.1093/database/baab012.

Rapkins, Robert W., Tim Hore, Megan Smithwick, Eleanor Ager, Andrew J. Pask, Marilyn B. Renfree, Matthias Kohn, et al. 2006. “Recent Assembly of an Imprinted Domain from Non-Imprinted Components.” *PLoS Genetics* 2 (10): e182.

Rappsilber, Juri, Yasushi Ishihama, and Matthias Mann. 2003. “Stop and Go Extraction Tips for Matrix-Assisted Laser Desorption/Ionization, Nanoelectrospray, and LC/MS Sample Pretreatment in Proteomics.” *Analytical Chemistry* 75 (3): 663–70.

Ratnadiwakara, Madara, and Minna-Liisa Änkö. 2018. “MRNA Stability Assay Using Transcription Inhibition by Actinomycin D in Mouse Pluripotent Stem Cells.” *Bio-Protocol* 8 (21): e3072.

Rebak, Alexandra S., Ivo A. Hendriks, Jonas D. Elsborg, Sara C. Buch-Larsen, Claus H. Nielsen, Lene Terslev, Rebecca Kirsch, et al. 2024. “A Quantitative and Site-Specific Atlas of the Citrullinome Reveals Widespread Existence of Citrullination and Insights into PADI4 Substrates.” *Nature Structural & Molecular Biology* 31 (6): 977–95.

Renny-Byfield, Simon, and Jonathan F. Wendel. 2014. “Doubling down on Genomes: Polyploidy and Crop Plants.” *American Journal of Botany* 101 (10): 1711–25.

Rice, Alan M., and Aoife McLysaght. 2017. “Dosage-Sensitive Genes in Evolution and Disease.” *BMC Biology* 15 (1): 78.

Rietschel, Benjamin, Tabiwang N. Arrey, Bjoern Meyer, Sandra Bornemann, Malte Schuerken, Michael Karas, and Ansgar Poetsch. 2009. “Elastase Digests: New Ammunition for Shotgun Membrane Proteomics.” *Molecular & Cellular Proteomics: MCP* 8 (5): 1029–43.

“Roche.” n.d. Accessed March 5, 2025. https://www.roche.com/solutions/pharma/productid-423934d3-782a-4102-884a-1db9fafc8ae8.

Rogers, Scott O., and Arnold J. Bendich. 2023. “Introns Are Derived from Transposons.” *BioRxiv*. https://doi.org/10.1101/2023.02.21.529479.

Rohm, Dahlia, Joshua B. Black, Sean R. McCutcheon, Alejandro Barrera, Shanté S. Berry, Daniel J. Morone, Xander Nuttle, et al. 2025. “Activation of the Imprinted Prader-Willi Syndrome Locus by CRISPR-Based Epigenome Editing.” *Cell Genomics* 5 (2): 100770.

Rovelet-Lecrux, Anne, Didier Hannequin, Gregory Raux, Nathalie Le Meur, Annie Laquerrière, Anne Vital, Cécile Dumanchin, et al. 2006. “APP Locus Duplication Causes Autosomal Dominant Early-Onset Alzheimer Disease with Cerebral Amyloid Angiopathy.” *Nature Genetics* 38 (1): 24–26.

Saltzman, Arneet L., Qun Pan, and Benjamin J. Blencowe. 2011. “Regulation of Alternative Splicing by the Core Spliceosomal Machinery.” *Genes & Development* 25 (4): 373–84.

Sammeth, Michael, Sylvain Foissac, and Roderic Guigó. 2008. “A General Definition and Nomenclature for Alternative Splicing Events.” *PLoS Computational Biology* 4 (8): e1000147.

Samuel, Sabrina F., Antonia Barry, John Greenman, and Pedro Beltran-Alvarez. 2021. “Arginine Methylation: The Promise of a ‘silver Bullet’ for Brain Tumours?” *Amino Acids* 53 (4): 489–506.

Sato, Hanae, and Robert H. Singer. 2021. “Cellular Variability of Nonsense-Mediated MRNA Decay.” *Nature Communications* 12 (1): 7203.

Schindelin, Johannes, Ignacio Arganda-Carreras, Erwin Frise, Verena Kaynig, Mark Longair, Tobias Pietzsch, Stephan Preibisch, et al. 2012. “Fiji: An Open-Source Platform for Biological-Image Analysis.” *Nature Methods* 9 (7): 676–82.

Schneider-Poetsch, Tilman, Jianhua Ju, Daniel E. Eyler, Yongjun Dang, Shridhar Bhat, William C. Merrick, Rachel Green, Ben Shen, and Jun O. Liu. 2010. “Inhibition of Eukaryotic Translation Elongation by Cycloheximide and Lactimidomycin.” *Nature Chemical Biology* 6 (3): 209–17.

Scotti, Marina M., and Maurice S. Swanson. 2016. “RNA Mis-Splicing in Disease.” *Nature Reviews. Genetics* 17 (1): 19–32.

Segert, Julian A., Stephen S. Gisselbrecht, and Martha L. Bulyk. 2021. “Transcriptional Silencers: Driving Gene Expression with the Brakes On.” *Trends in Genetics: TIG* 37 (6): 514–27.

Serefidou, Magdalini, Anuroop Venkateswaran Venkatasubramani, and Axel Imhof. 2019. “The Impact of One Carbon Metabolism on Histone Methylation.” *Frontiers in Genetics* 10 (August): 764.

Sharpe, N. G., D. G. Williams, and D. S. Latchman. 1990. “Regulated Expression of the Small Nuclear Ribonucleoprotein Particle Protein SmN in Embryonic Stem Cell Differentiation.” *Molecular and Cellular Biology* 10 (12): 6817–20.

Shen, Shihao, Juw Won Park, Zhi-Xiang Lu, Lan Lin, Michael D. Henry, Ying Nian Wu, Qing Zhou, and Yi Xing. 2014. “RMATS: Robust and Flexible Detection of Differential Alternative Splicing from Replicate RNA-Seq Data.” *Proceedings of the National Academy of Sciences of the United States of America* 111 (51): E5593-601.

Shen, Shiquan, Honglong Zhou, Zongyu Xiao, Shaofen Zhan, Yonghua Tuo, Danmin Chen, Xiao Pang, Yezhong Wang, and Ji Wang. 2024. “PRMT1 in Human Neoplasm: Cancer Biology and Potential Therapeutic Target.” *Cell Communication and Signaling: CCS* 22 (1): 102.

Siam, Ahmad, Mai Baker, Leah Amit, Gal Regev, Alona Rabner, Rauf Ahmad Najar, Mercedes Bentata, et al. 2019. “Regulation of Alternative Splicing by P300-Mediated Acetylation of Splicing Factors.” *RNA (New York, N.Y.)* 25 (7): 813–24.

Singh, Natalia N., Collin A. O’Leary, Taylor Eich, Walter N. Moss, and Ravindra N. Singh. 2022. “Structural Context of a Critical Exon of Spinal Muscular Atrophy Gene.” *Frontiers in Molecular Biosciences* 9 (July): 928581.

Sylvestersen, Kathrine B., Heiko Horn, Stephanie Jungmichel, Lars J. Jensen, and Michael L. Nielsen. 2014. “Proteomic Analysis of Arginine Methylation Sites in Human Cells Reveals Dynamic Regulation during Transcriptional Arrest.” *Molecular & Cellular Proteomics: MCP* 13 (8): 2072–88.

Szelest, Monika, and Krzysztof Giannopoulos. 2024. “Targeting Splicing for Hematological Malignancies Therapy.” *BMC Genomics* 25 (1): 1067.

Taylor, Alison M., Juliann Shih, Gavin Ha, Galen F. Gao, Xiaoyang Zhang, Ashton C. Berger, Steven E. Schumacher, et al. 2018. “Genomic and Functional Approaches to Understanding Cancer Aneuploidy.” *Cancer Cell* 33 (4): 676-689.e3.

Tewary, Sunil Kumar, Y. George Zheng, and Meng-Chiao Ho. 2019. “Protein Arginine Methyltransferases: Insights into the Enzyme Structure and Mechanism at the Atomic Level.” *Cellular and Molecular Life Sciences: CMLS* 76 (15): 2917–32.

Thompson, Luke W., Kim D. Morrison, Sally L. Shirran, Ewout J. N. Groen, Thomas H. Gillingwater, Catherine H. Botting, and Judith E. Sleeman. 2018. “Neurochondrin Interacts with the SMN Protein Suggesting a Novel Mechanism for Spinal Muscular Atrophy Pathology.” *Journal of Cell Science* 131 (8). https://doi.org/10.1242/jcs.211482.

Tinevez, Jean-Yves, Nick Perry, Johannes Schindelin, Genevieve M. Hoopes, Gregory D. Reynolds, Emmanuel Laplantine, Sebastian Y. Bednarek, Spencer L. Shorte, and Kevin W. Eliceiri. 2017. “TrackMate: An Open and Extensible Platform for Single-Particle Tracking.” *Methods (San Diego, Calif.)* 115 (February): 80–90.

Tognacca, Rocío S., Florencia S. Rodríguez, Federico E. Aballay, Carla M. Cartagena, Lucas Servi, and Ezequiel Petrillo. 2023. “Alternative Splicing in Plants: Current Knowledge and Future Directions for Assessing the Biological Relevance of Splice Variants.” *Journal of Experimental Botany* 74 (7): 2251–72.

Tomuro, Kotaro, Mari Mito, Hirotaka Toh, Naohiro Kawamoto, Takahito Miyake, Siu Yu A. Chow, Masao Doi, Yoshiho Ikeuchi, Yuichi Shichino, and Shintaro Iwasaki. 2024. “Calibrated Ribosome Profiling Assesses the Dynamics of Ribosomal Flux on Transcripts.” *Nature Communications* 15 (1): 7061.

Trewick, Sarah C., Paul J. McLaughlin, and Robin C. Allshire. 2005. “Methylation: Lost in Hydroxylation?” *EMBO Reports* 6 (4): 315–20.

Tsai, Ting-Fen, Ken-Shiung Chen, John S. Weber, Monica J. Justice, and Arthur L. Beaudet. 2002. “Evidence for Translational Regulation of the Imprinted Snurf-Snrpn Locus in Mice.” *Human Molecular Genetics* 11 (14): 1659–68.

Turner, Benedict R. H., Charlotte Mellor, Clara McElroy, Natalie Bowen, Wenjia Gu, Chris Knill, and Nobue Itasaki. 2023. “Non-Ubiquitous Expression of Core Spliceosomal Protein SmB/B’ in Chick and Mouse Embryos.” *Developmental Dynamics: An Official Publication of the American Association of Anatomists* 252 (2): 276–93.

Ustianenko, Dmytro, Sebastien M. Weyn-Vanhentenryck, and Chaolin Zhang. 2017. “Microexons: Discovery, Regulation, and Function.” *Wiley Interdisciplinary Reviews. RNA* 8 (4). https://doi.org/10.1002/wrna.1418.

Wang, Yalong, and Mark T. Bedford. 2023. “Effectors and Effects of Arginine Methylation.” *Biochemical Society Transactions* 51 (2): 725–34.

Wang, Yan, Jing Liu, B. O. Huang, Yan-Mei Xu, Jing Li, Lin-Feng Huang, Jin Lin, et al. 2015. “Mechanism of Alternative Splicing and Its Regulation.” *Biomedical Reports* 3 (2): 152–58.

Warren, Ian A., Kate L. Ciborowski, Elisa Casadei, David G. Hazlerigg, Sam Martin, William C. Jordan, and Seirian Sumner. 2014. “Extensive Local Gene Duplication and Functional Divergence among Paralogs in Atlantic Salmon.” *Genome Biology and Evolution* 6 (7): 1790–1805.

Wijngaarden, Marjolein A., Leontine E. H. Bakker, Gerard C. van der Zon, Peter A. C. ’t Hoen, Ko Willems van Dijk, Ingrid M. Jazet, Hanno Pijl, and Bruno Guigas. 2014. “Regulation of Skeletal Muscle Energy/Nutrient-Sensing Pathways during Metabolic Adaptation to Fasting in Healthy Humans.” *American Journal of Physiology. Endocrinology and Metabolism* 307 (10): E885-95.

Will, Cindy L., and Reinhard Lührmann. 2011. “Spliceosome Structure and Function.” *Cold Spring Harbor Perspectives in Biology* 3 (7): a003707–a003707.

Wong, Justin J-L, Amy Y. M. Au, William Ritchie, and John E. J. Rasko. 2016. “Intron Retention in MRNA: No Longer Nonsense: Known and Putative Roles of Intron Retention in Normal and Disease Biology.” *BioEssays: News and Reviews in Molecular, Cellular and Developmental Biology* 38 (1): 41–49.

Wu, Jianchun, Crystal Chun, Angelica M. Lagunas, and David L. Crowe. 2024. “Lysine Methyltransferase 2D Regulates Immune Response and Metastasis in Head and Neck Cancer.” *Anticancer Research* 44 (8): 3231–42.

Wu, Qin, Matthieu Schapira, Cheryl H. Arrowsmith, and Dalia Barsyte-Lovejoy. 2021. “Protein Arginine Methylation: From Enigmatic Functions to Therapeutic Targeting.” *Nature Reviews. Drug Discovery* 20 (7): 509–30.

Xie, Zizhuo, Yuan Tian, Xiaohan Guo, and Na Xie. 2024. “The Emerging Role of CARM1 in Cancer.” *Cellular Oncology* , April. https://doi.org/10.1007/s13402-024-00943-9.

Xu, Jian, and Stéphane Richard. 2021. “Cellular Pathways Influenced by Protein Arginine Methylation: Implications for Cancer.” *Molecular Cell* 81 (21): 4357–68.

Yang, Yu-Hang, Ri Wen, Ni Yang, Tie-Ning Zhang, and Chun-Feng Liu. 2023. “Roles of Protein Post-Translational Modifications in Glucose and Lipid Metabolism: Mechanisms and Perspectives.” *Molecular Medicine (Cambridge, Mass.)* 29 (1): 93.

Yeo, Crystal J. J., Eduardo F. Tizzano, and Basil T. Darras. 2024. “Challenges and Opportunities in Spinal Muscular Atrophy Therapeutics.” *Lancet Neurology* 23 (2): 205–18.

Yildirim, Adem, Sina Mozaffari-Jovin, Ann-Kathrin Wallisch, Jessica Schäfer, Sebastian E. J. Ludwig, Henning Urlaub, Reinhard Lührmann, and Uwe Wolfrum. 2021. “SANS (USH1G) Regulates Pre-MRNA Splicing by Mediating the Intra-Nuclear Transfer of Tri-SnRNP Complexes.” *Nucleic Acids Research* 49 (10): 5845–66.

Yokoi, Akira, Yoshihiko Kotake, Kentaro Takahashi, Tadashi Kadowaki, Yoshiko Matsumoto, Yukinori Minoshima, Naoko H. Sugi, et al. 2011. “Biological Validation That SF3b Is a Target of the Antitumor Macrolide Pladienolide.” *The FEBS Journal* 278 (24): 4870–80.

Yong, Jeongsik, Tracey J. Golembe, Daniel J. Battle, Livio Pellizzoni, and Gideon Dreyfuss. 2004. “SnRNAs Contain Specific SMN-Binding Domains That Are Essential for SnRNP Assembly.” *Molecular and Cellular Biology* 24 (7): 2747–56.

Zack, G. W., W. E. Rogers, and S. A. Latt. 1977. “Automatic Measurement of Sister Chromatid Exchange Frequency.” *The Journal of Histochemistry and Cytochemistry: Official Journal of the Histochemistry Society* 25 (7): 741–53.

Zakrzewicz, Dariusz, Anna Zakrzewicz, Klaus T. Preissner, Philipp Markart, and Malgorzata Wygrecka. 2012. “Protein Arginine Methyltransferases (PRMTs): Promising Targets for the Treatment of Pulmonary Disorders.” *International Journal of Molecular Sciences* 13 (10): 12383–400.

Zhan, Yujuan, Jingru Guo, Penghui Hu, Ruiyan Huang, Jiangyue Ning, Xingyan Bao, Haotian Chen, Zelong Yan, Li Ding, and Chang Shu. 2024. “A Sensitive Analytical Strategy of Oligonucleotide Functionalized Fluorescent Probes for Detection of Nusinersen Sodium in Human Serum.” *Talanta* 275 (126153): 126153.

Zhang, Hong, Wu Chen, De Zhu, Bintao Zhang, Qiang Xu, Chuanlin Shi, Huiying He, et al. 2024. “Population-Level Exploration of Alternative Splicing and Its Unique Role in Controlling Agronomic Traits of Rice.” *The Plant Cell* 36 (10): 4372–87.

Zhang, Huiyuan, Jun Dou, Yang Yu, Yanling Zhao, Yihui Fan, Jin Cheng, Xin Xu, et al. 2015. “MTOR ATP-Competitive Inhibitor INK128 Inhibits Neuroblastoma Growth via Blocking MTORC Signaling.” *Apoptosis: An International Journal on Programmed Cell Death* 20 (1): 50–62.

Zhang, Zhenxi, Francesco Lotti, Kimberly Dittmar, Ihab Younis, Lili Wan, Mumtaz Kasim, and Gideon Dreyfuss. 2008. “SMN Deficiency Causes Tissue-Specific Perturbations in the Repertoire of SnRNAs and Widespread Defects in Splicing.” *Cell* 133 (4): 585–600.

Zhong, Qian, Xina Xiao, Yijie Qiu, Zhiqiang Xu, Chunyu Chen, Baochen Chong, Xinjun Zhao, et al. 2023. “Protein Posttranslational Modifications in Health and Diseases: Functions, Regulatory Mechanisms, and Therapeutic Implications.” *MedComm* 4 (3): e261.

Zhu, Di, Yu Lu, Yanming Wang, and Yuji Wang. 2022. “PAD4 and Its Inhibitors in Cancer Progression and Prognosis.” *Pharmaceutics* 14 (11): 2414.

8. Supplementary tables

Supplementary Table 8. 1. Significant differential intron retention events between SRNPB versus SNRPN identified by IRFinder. The analysis identified 14 significant intron retention events affecting 12 genes.

Gene	Base Mean	log_2 Fold Change	Standard error of log_2 Fold Change	Statistics	p-value	p_{adj}
ENSG00000273748/ENSG00000273748.1/clean/GL000219.1:54293-78841:-	6.063	-0.372	1.297	-0.287	0.774	0.000
ENSG00000273748/ENSG00000273748.1/clean/GL000219.1:78952-79936:-	11.813	-0.310	1.272	-0.243	0.808	0.000
ENSG00000273748/ENSG00000273748.1/clean/GL000219.1:80028-83212:-	21.375	0.000	1.480	0.000	1.000	0.000
ENSG00000275063/ENSG00000275063.1/clean/KI270726.1:41489-41571:+	0.000	NA	NA	NA	NA	0.000
ENSG00000273554/ENSG00000273554.4/clean/KI270728.1:1142905-1142992:-	0.000	NA	NA	NA	NA	0.000
SAMD11/ENSG00000187634.13/clean/chr1:924948-925921:+	80.438	0.447	0.421	1.060	0.289	0.003
SAMD11/ENSG00000187634.13/clean/chr1:925189-925921:+	79.313	0.602	0.492	1.224	0.221	0.017
SAMD11/ENSG00000187634.13/clean/chr1:925800-925921:+	80.625	0.699	0.415	1.685	0.092	0.017
SAMD11/ENSG00000187634.13/clean/chr1:926013-930154:+	108.188	0.426	0.251	1.698	0.089	0.033
SAMD11/ENSG00000187634.13/clean/chr1:930336-931038:+	129.938	-0.174	0.376	-0.462	0.644	0.033
SAMD11/ENSG00000187634.13/clean/chr1:930336-935771:+	135.063	0.122	0.367	0.332	0.740	0.034
SAMD11/ENSG00000187634.13/clean/chr1:931089-935771:+	130.375	0.308	0.358	0.859	0.390	0.034
SAMD11/ENSG00000187634.13/clean/chr1:935896-939039:+	116.000	0.663	0.480	1.380	0.168	0.034
SAMD11/ENSG00000187634.13/clean/chr1:939129-939274:+	108.813	-0.505	1.034	-0.489	0.625	0.034

9. Supplementary figures

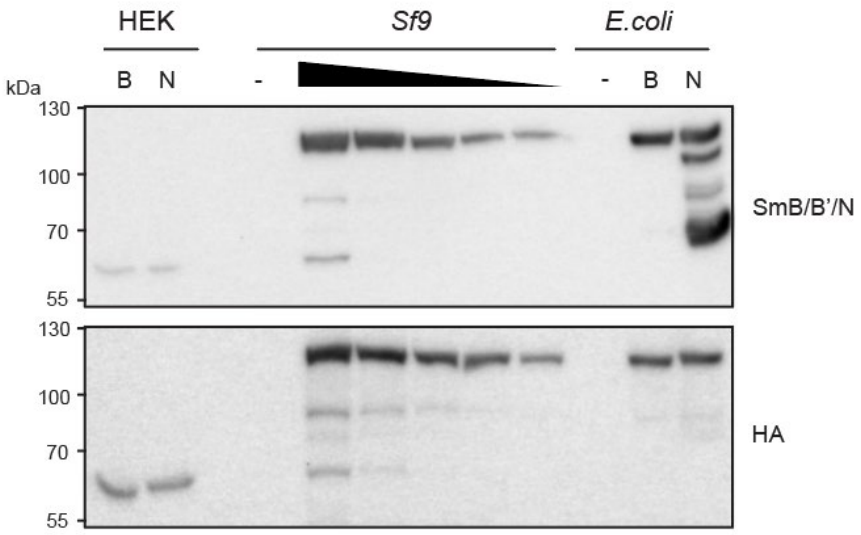

Supplementary Figure 9. 1. Unmethylated Arginine residues are sufficient for 12F5 (SmB/B'/N) binding. Western blot of SNRPB (B) and SNRPN (N) expressed in HEK293T cells, *Sf9* insect cells and *E.coli* cells using 12F5 and HA antibodies. "-" indicates empty vector control.

CURRICULUM VITAE